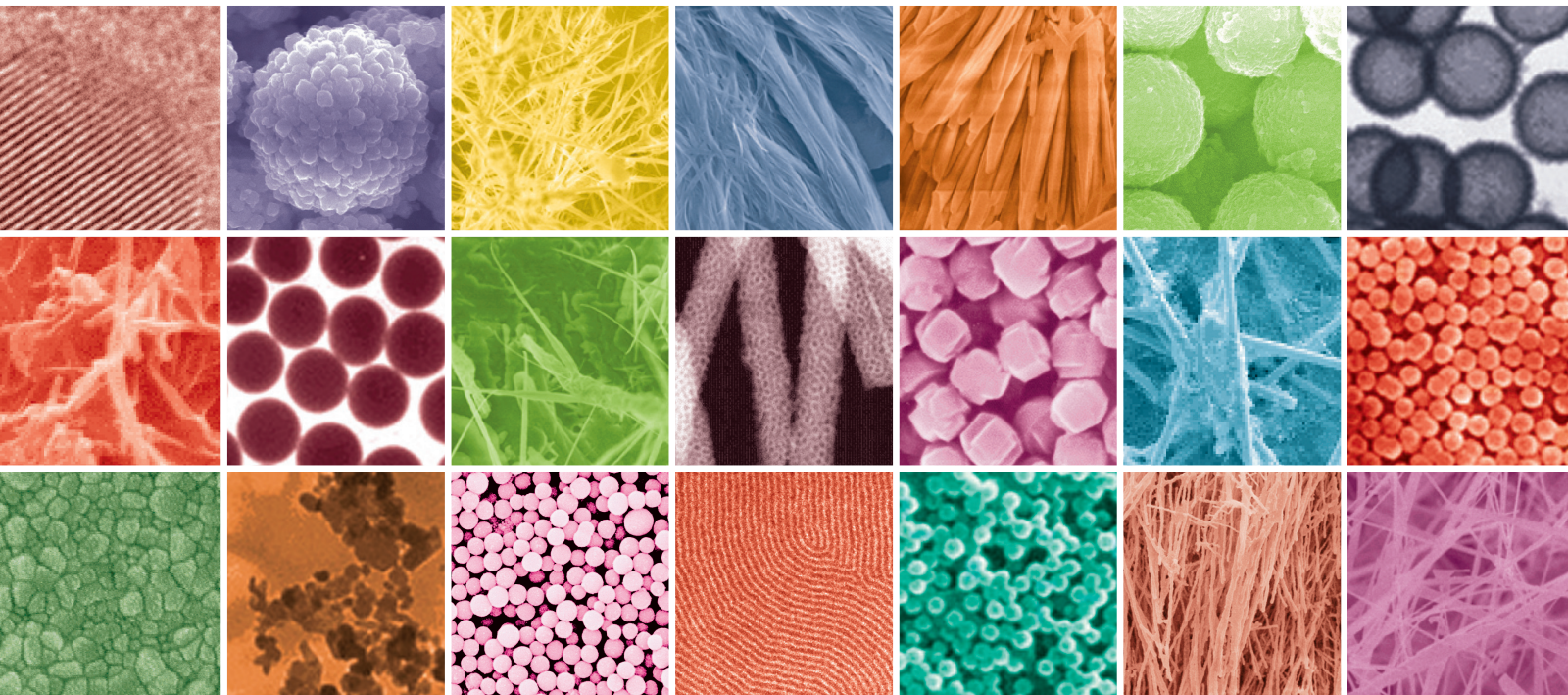


Biocompatible Functional Nanomaterials: Synthesis, Properties, and Applications

Guest Editors: Jiu-Ju Feng, Yan-Yan Song, Xiao-Miao Feng, Nabeen Kumar Shrestha, and Nattawadee Wisitruangsakul





Biocompatible Functional Nanomaterials: Synthesis, Properties, and Applications

Biocompatible Functional Nanomaterials: Synthesis, Properties, and Applications

Guest Editors: Jiu-Ju Feng, Yan-Yan Song, Xiao-Miao Feng,
Nabeen Kumar Shrestha, and Nattawadee Wisitruangsakul



Copyright © 2013 Hindawi Publishing Corporation. All rights reserved.

This is a special issue published in "Journal of Nanomaterials." All articles are open access articles distributed under the Creative Commons Attribution License, which permits unrestricted use, distribution, and reproduction in any medium, provided the original work is properly cited.

Editorial Board

Katerina E. Aifantis, Greece
Nageh K. Allam, USA
Margarida Amaral, Portugal
Xuedong Bai, China
Lavinia Balan, France
Enrico Bergamaschi, Italy
Theodorian Borca-Tasciuc, USA
C. Jeffrey Brinker, USA
Christian Brosseau, France
Xuebo Cao, China
Shafiq Chowdhury, USA
Kwang-Leong Choy, UK
Cui Chunxiang, China
Miguel A. Correa-Duarte, Spain
Shadi A. Dayeh, USA
Claude Estourns, France
Alan Fuchs, USA
Lian Gao, China
Russell E. Gorga, USA
Hongchen Chen Gu, China
Mustafa O. Guler, Turkey
John Zhanhu Guo, USA
Smrati Gupta, Germany
Michael Harris, USA
Zhongkui Hong, China
Michael Z. Hu, USA
David Hui, USA
Y.-K. Jeong, Republic of Korea
Sheng-Rui Jian, Taiwan
Wanqin Jin, China
Rakesh K. Joshi, UK
Zhenhui Kang, China
Fathallah Karimzadeh, Iran
Alireza Khataee, Iran

Do Kyung Kim, Korea
Alan K. T. Lau, Hong Kong
Burtrand Lee, USA
Jun Li, Singapore
Benxia Li, China
Xing-Jie Liang, China
Shijun Liao, China
Gong Ru Lin, Taiwan
J. -Y. Liu, USA
Tianxi Liu, China
Jue Lu, USA
Songwei Lu, USA
Daniel Lu, China
Ed Ma, USA
Gaurav Mago, USA
Santanu K. Maiti, India
Sanjay R. Mathur, Germany
Vikas Mittal, UAE
Weihai Ni, Germany
Sherine Obare, USA
Atsuto Okamoto, Japan
Abdelwahab Omri, Canada
Edward Andrew Payzant, USA
Kui-Qing Peng, China
Anukorn Phuruangrat, Thailand
Suprakas S. Ray, South Africa
Ugur Serincan, Turkey
Huaiyu Shao, Japan
Donglu Shi, USA
Vladimir Sivakov, Germany
Marinella Striccoli, Italy
Bohua Sun, South Africa
Saikat Talapatra, USA
Nairong Tao, China

Titipun Thongtem, Thailand
Somchai Thongtem, Thailand
Alexander Tolmachev, Ukraine
Valeri P. Tolstoy, Russia
Tsung-Yen Tsai, Taiwan
Takuya Tsuzuki, Australia
Raquel Verdejo, Spain
Mat U. Wahit, Malaysia
Zhenbo Wang, China
Ruiping Wang, Canada
Shiren Wang, USA
Cheng Wang, China
Yong Wang, USA
Jinquan Wei, China
Ching-Ping Wong, Hong Kong
Xingcai Wu, China
Guodong Xia, Hong Kong
Zhi Li Xiao, USA
Ping Xiao, UK
Yangchuan Xing, USA
Shuangxi Xing, China
N. Xu, China
Doron Yadlovker, Israel
Yingkui Yang, China
Khaled Youssef, USA
Kui Yu, Canada
William W. Yu, USA
Haibo Zeng, China
Tianyou Zhai, Japan
Renyun Zhang, Sweden
Bin Zhang, China
Yanbao Zhao, China
Lianxi Zheng, Singapore
Chunyi Zhi, Hong Kong

Contents

Biocompatible Functional Nanomaterials: Synthesis, Properties, and Applications, Jiu-Ju Feng, Yan-Yan Song, Xiao-Miao Feng, Nabeen Kumar Shrestha, and Nattawadee Wisitruangsakul
Volume 2013, Article ID 385939, 1 page

Effects of Surface Morphology of ZnAl₂O₄ Ceramic Materials on Osteoblastic Cells Responses, José Luis Suárez-Franco, Manuel García-Hipólito, Miguel Ángel Surárez-Rosales, José Arturo Fernández-Pedrero, Octavio Álvarez-Fregoso, Julio Alberto Juárez-Islas, and Marco Antonio Álvarez-Pérez
Volume 2013, Article ID 361249, 7 pages

Obtaining of Sol-Gel Ketorolac-Silica Nanoparticles: Characterization and Drug Release Kinetics, T. M. López Goerne, M. G. López García, G. Rodríguez Grada, I. Ortiz Pérez, E. Gómez López, and M. A. Alvarez Lemus
Volume 2013, Article ID 450483, 9 pages

Factorial Study of Compressive Mechanical Properties and Primary *In Vitro* Osteoblast Response of PHBV/PLLA Scaffolds, Naznin Sultana and Tareef Hayat Khan
Volume 2012, Article ID 656914, 8 pages

Hydroxyapatite Nanopowder Synthesis with a Programmed Resorption Rate, Dariusz Smoleń, Tadeusz Chudoba, Stanisław Gierlotka, Aleksandra Kedzierska, Witold Łojkowski, Kamil Sobczak, Wojciech Świążkowski, and Krzysztof Jan Kurzydłowski
Volume 2012, Article ID 841971, 9 pages

Understanding the Biocompatibility of Sintered Calcium Phosphate with Ratio of [Ca]/[P] = 1.50, Feng-Lin Yen, Wei-Jen Shih, Min-Hsiung Hon, Hui-Ting Chen, I-Ming Hung, Homg-Huey Ko, and Moo-Chin Wang
Volume 2012, Article ID 325605, 8 pages

Property Evaluation of *Bletilla striata*/Polyvinyl Alcohol Nano Fibers and Composite Dressings, Jia-Horng Lin, Chao-Tsang Lu, Jin-Jia Hu, Yueh-Sheng Chen, Chen-Hung Huang, and Ching-Wen Lou
Volume 2012, Article ID 519516, 7 pages

Sonochemical Synthesis of Er³⁺-Doped ZnO Nanospheres with Enhanced Upconversion Photoluminescence, Jun Geng, Guang-Hui Song, and Jun-Jie Zhu
Volume 2012, Article ID 317857, 5 pages

Facile Synthesis of Calcium Carbonate Nanoparticles from Cockle Shells, Kh. Nurul Islam, A. B. Z. Zuki, M. E. Ali, Mohd Zobir Bin Hussein, M. M. Noordin, M. Y. Loqman, H. Wahid, M. A. Hakim, and Sharifa Bee Abd Hamid
Volume 2012, Article ID 534010, 5 pages

High-Sensitive Sensor of Dopamine Based on Photoluminescence Quenching of Hierarchical CdS Spherical Aggregates, Binjie Sun and Changzheng Wang
Volume 2012, Article ID 502481, 6 pages

Editorial

Biocompatible Functional Nanomaterials: Synthesis, Properties, and Applications

Jiu-Ju Feng,¹ Yan-Yan Song,² Xiao-Miao Feng,³
Nabeen Kumar Shrestha,⁴ and Nattawadee Wisitruangsakul⁵

¹ College of Chemistry and Life Science, Zhejiang Normal University, Jinhua 321004, China

² College of Sciences, Northeastern University, Shenyang 110004, China

³ Key Laboratory for Organic Electronics & Information Displays (KLOEID), Institute of Advanced Materials (IAM), Nanjing University of Posts & Telecommunications (NUPT), Nanjing 210046, China

⁴ Nepal Academy of Science & Technology, P.O. Box 3323, Khumaltar, Lalitpur 44700, Nepal

⁵ Bureau of Industrial Sectors Development Building, 1st-2nd Floor, Soi Trimitr, Rama IV Road, Prakanong, Klong-Toey, Bangkok 10110, Thailand

Correspondence should be addressed to Jiu-Ju Feng; jjfeng@zjnu.cn

Received 23 May 2013; Accepted 23 May 2013

Copyright © 2013 Jiu-Ju Feng et al. This is an open access article distributed under the Creative Commons Attribution License, which permits unrestricted use, distribution, and reproduction in any medium, provided the original work is properly cited.

Biocompatible nanomaterials are revolutionizing many aspects of preventive and therapeutic healthcare, which are already playing important roles in developing new medical devices, prostheses, bioassay technologies, tissue repair and replacement technologies, drug delivery systems, and diagnostic techniques. In recent years, much attention has been focused on the synthesis and applications of biocompatible functional nanomaterials, owing to their promising potential and practical applications in biomedical science, biosensors, biochip design, drug delivery, cancer diagnosis and therapy, implantable devices, gene vectors, bionanotechnology, and tissue engineering.

This special issue is one of the important and keep growing fields on nanoscience, nanoengineering, and nanotechnology. Its to create new functional nanomaterials with a variety of sizes and morphologies such as ZnAl_2O_4 films, hydroxyapatite nanopowder, and calcium carbonate nanoparticles. These nanomaterials have widespread applications in drug delivery, tissue engineering, dental implant, bone substitute, sensors, photoluminescence, and mechanical properties. This themed issue includes some research articles covering important applications of biocompatible functional nanomaterials. M. A. Alvarez-Pérez et al. fabricated the thin nanostructure films of ZnAl_2O_4 prepared by spray pyrolysis, which improved the in vitro cell adhesion on the surface of the as-prepared ceramic film, viability, and cell-material

interactions of osteoblastic cells. Zhu's group synthesized rare earth-ions- (Er^{3+} -) doped ZnO nanospheres through a sonochemical conversion process that displayed enhanced photoluminescence and upconversion photoluminescence properties, in comparison with pure ZnO counterparts. In particular, biocompatible functional nanomaterials have promising potential applications in biomedical field because of their excellent biocompatibility. For example, Goerne and his coworkers have prepared SiO_2 -based nanoparticles in the mixed solvents (water and alcoxide) by the sol-gel technology at acidic conditions and applied for the control delivery of nonsteroidal anti-inflammatory drugs.

Altogether, this issue suggests that the biocompatible functional nanomaterials have a great potential to be used in drug delivery, tissue engineering, bone substitutes, bone-filling materials, sensors, and photoluminescence. It provides new research and developments of the biocompatible functional nanomaterials performed by the researchers in this field.

Jiu-Ju Feng
Yan-Yan Song
Xiao-Miao Feng
Nabeen Kumar Shrestha
Nattawadee Wisitruangsakul

Research Article

Effects of Surface Morphology of ZnAl_2O_4 Ceramic Materials on Osteoblastic Cells Responses

José Luis Suárez-Franco,¹ Manuel García-Hipólito,² Miguel Ángel Surárez-Rosales,²
José Arturo Fernández-Pedrero,¹ Octavio Álvarez-Fregoso,²
Julio Alberto Juárez-Islas,² and Marco Antonio Álvarez-Pérez^{1,3}

¹Laboratorio de Bioingeniería de Tejidos, Facultad de Odontología, Universidad Nacional Autónoma de México, Coyoacán, 04510 Ciudad de México, DF, Mexico

²Instituto de Investigaciones en Materiales, Universidad Nacional Autónoma de México, Coyoacán, 04510 Ciudad de México, DF, Mexico

³Tissue Bioengineering Laboratory, Division of Research and Postgraduate Studies, Faculty of Dentistry, National Autonomous University of Mexico (UNAM), Circuito Exterior s/n, Coyoacan, 04510 Mexico City, DF, Mexico

Correspondence should be addressed to Marco Antonio Álvarez-Pérez; marcoalv@unam.mx

Received 5 September 2012; Revised 16 January 2013; Accepted 17 January 2013

Academic Editor: Nabeen Kumar Shrestha

Copyright © 2013 José Luis Suárez-Franco et al. This is an open access article distributed under the Creative Commons Attribution License, which permits unrestricted use, distribution, and reproduction in any medium, provided the original work is properly cited.

Ceramic scaffolds are widely studied in the tissue engineering field due to their potential in medical applications as bone substitutes or as bone-filling materials. The purpose of this study was to investigate the effect of surface morphology of nanostructure thin films of ZnAl_2O_4 prepared by spray pyrolysis and bulk pellets of polycrystalline ZnAl_2O_4 prepared by chemical coprecipitation reaction on the *in vitro* cell adhesion, viability, and cell-material interactions of osteoblastic cells. Our result showed that cell attachment was significantly enhanced from 60 to 80% on the ZnAl_2O_4 nanostructured material surface when compared with bulk ceramic surfaces. Moreover, our results showed that the balance of morphological properties of the thin film nanostructure ceramic improves cell-material interaction with enhanced spreading and filopodia with multiple cellular extensions on the surface of the ceramic and enhancing cell viability/proliferation in comparison with bulk ceramic surfaces used as control. Altogether, these results suggest that zinc aluminate nanostructured materials have a great potential to be used in dental implant and bone substitute applications.

1. Introduction

Oxide spinel material is a very large group of structurally related compounds [1], many of which are of considerable technological or geological importance [2]. Spinel exhibits a wide range of electronic and magnetic properties. The normal spinel is a typical example of a material with the general formula $(X)[Y]_2O_4$, where X and Y are divalent and trivalent ions, respectively, and the symbols () and [] refer to the 8 tetrahedral coordinated A sites and 16 octahedral coordinated B sites, respectively, within the cubic cell. ZnAl_2O_4 is an oxide spinel with a close-packed face centered cubic structure and $Fd\bar{3}m$ space group symmetry [3]. Moreover, its band gap of 3.8 eV makes it transparent for light possessing wavelengths

>320 nm; these characteristics allow to use it as a host lattice for applications in thin film electroluminescent displays, mechano-optical stress sensors, and stress imaging devices. On the other hand, this material has good catalytic properties such as cracking, dehydration, and dehydrogenation [4]. The spinel zinc aluminates have been widely used as ceramic and as catalytic material in chemical and petrochemical industries [5] and more recently as transparent conductor. Regarding the biological application potentials of this ZnAl_2O_4 ceramic material in thin films and in bulk are very scarce. The search for bone substitute is still a challenge to researchers. The composition, as well as the topography, of such materials is of importance for determining the biological response to such materials [6]. The roughness of materials

is considered to be important to predict interfacial behavior at the material-tissue interface and its interaction with the biological environment. Surface roughness influences cell bioactivity, being important in several bone formation stages, including adhesion, proliferation, differentiation, synthesis of bone matrix, maturation, and calcification of the tissue on the materials surface [7–10]. Besides, bioactivity or bioinertness could result in materials with different physical characteristic that could influence biological behavior [11, 12]. Recently, a number of studies have been carried out to investigate the Zn-doped ceramics as biomaterials in bone tissue engineering [13, 14]. Similar to calcium, zinc has long been recognized as an essential trace element for the proper maintenance of bone growth, with over 85% of the total body zinc residing in bone [15, 16]. Zn has a stimulatory effect on bone formation, and its deficiency has been associated with retardation and failure of bone growth in animals [17, 18]. Zn-substituted ceramics were found that modulate the attachment, proliferation, and differentiation of osteoblasts and modulate the activity of bone formation by the cells [19–21]. In this context, the aim of this study was to investigate the effect of surface morphology of nanostructured thin films of ZnAl_2O_4 prepared by spray pyrolysis and bulk pellets of polycrystalline ZnAl_2O_4 prepared by chemical coprecipitation reaction on the biological response of osteoblastic cells in order to evaluate the surface cell adhesion, spreading, cell viability process at *in vitro* cell culture and compare these results with respect to the different surface morphologies between a nanostructured thin film and a traditional polycrystalline ceramic surface.

2. Experimental Details

2.1. Synthesis and Characterization of ZnAl_2O_4 Material. The ultrasonic spray pyrolysis technique is a well-established process for depositing films. Some advantages of this process are as follow: a high deposition rate, the possibility to coat large areas, its low cost, its ease of operation, and the quality of the coatings obtained. Films of zinc aluminate were deposited by an ultrasonic spray pyrolysis technique described earlier [22]. Basically, this technique consists of an ultrasonic generator used to produce a mist from the spraying solution. This mist is carried to a hot substrate placed on a tin bath through a tubing setup using humid air as a carrier gas (10 liters/minute). When the mist of the solution gets in touch with the hot substrate, the solvents in the solution are vaporized producing a solid coating on the substrate. The nozzle in this system is localized approximately 1 cm above the substrate. The spraying solution consisted of 0.05 M zinc acetate and aluminum chloride in deionized water as solvent. The solution flow rate was 3 mL/minute for all cases. The substrate temperature (T_s) during deposition was in the range from 300°C to 550°C; the substrates used were Corning 7059 glass slides. The deposition time was adjusted (4 to 6 minutes) to deposit films with approximately the same thickness. The thickness of the films studied was about 5 μm as measured by a Sloan Dektak IIA profilometer. The chemical composition of the films was measured with a Leica-Cambridge electron microscope Mo. Stereoscan 440, equipped with a Beryllium window X-ray

detector, using Energy Dispersive Spectroscopy (EDS). The standard used for the EDS measurements was the Multi-element X-ray Reference Standard (Microspec), Serial 0034, part no. 8160-53. The surface morphology was analyzed by means of the scanning electron microscopy (SEM) cited above. The crystalline structure features of the deposited films were analyzed by X-ray diffraction (XRD), using a Siemens D-5000 diffractometer with a wavelength radiation of 1.5406 Å (CuK_α).

A very simple chemical precipitation process was used for the synthesis of zinc aluminate spinel powder. The start materials were $\text{Zn}(\text{NO}_3)_2 \cdot 6\text{H}_2\text{O}$ Sigma-Aldrich (98%) and $\text{Al}(\text{NO}_3)_3 \cdot 9\text{H}_2\text{O}$ Riedel-de Haën at 0.05 M blended in methanol. This simple process consists of three steps: (1) precursor material dissolution in a compatible solvent to form the precursor mixture, (2) solvent evaporation and solute precipitation, and (3) powder annealing. The initial mixture was heat treated at 250°C for 30 minutes to evaporate the solvent. The chemical agglomerates were grounded in an agate mortar to obtain fine powder, which was compressed to form a small disk with a dimension of 1.2 cm in diameter and a thickness of 0.13 cm. The applied pressure for pellets preparation was 150 Kg/cm². These pellets were annealed at $T_a = 600^\circ\text{C}$, during 14 hours in air atmosphere.

The crystalline structure of these pellets was analyzed by X-ray diffraction (XRD) using a Bruker-D8 plus Diffractometer with CuK_α radiation at 1.5405 Å. Their chemical composition was measured using Energy Dispersive Spectroscopy (EDS) with a Cambridge-Leica electron microscope mod. Stereoscan 440 was equipped with a Beryllium window X-ray detector, and their surface topography was obtained by means of the above-mentioned SEM microscope.

2.2. Biological Response

2.2.1. Cell Culture. Biological assays were performed using human osteoblastic cells as reported previously [23]. For cell culture, human osteoblastic cells were cultured in 75 cm² cell culture flasks containing a Dulbecco's Modified Eagle Media (DMEM), supplemented with 10% fetal bovine serum (FBS) and antibiotic solution (streptomycin 100 $\mu\text{g}/\text{mL}$ and penicillin 100 U/mL, Sigma Chem. Co). The cell cultures were incubated in a 100% humidified environment at 37°C in atmosphere of 95% air and 5% CO_2 . Human osteoblastic cells on passage 4–6 were used for all the experimental procedures. In order to perform the *in vitro* cell response assays, all ZnAl_2O_4 bulk and 550°C nanostructured material surfaces were cleaned with distilled water and sterilized by exposure to UV light ($\lambda = 254 \text{ nm}$, 300 uW/cm²).

2.2.2. Cell Attachment. The cell adhesion of human osteoblastic cells onto ZnAl_2O_4 bulk and thin film nanostructure materials was evaluated using the vibrant cell adhesion assay kit (Molecular Probes). Human osteoblastic cells, cultured in a 75 cm² cell culture flask, were washed with phosphate-buffered saline (PBS) and incubated with calcein AM stock solution to a final concentration of 5×10^{-6} M in serum-free medium for 30 min. After incubation, the cells were washed

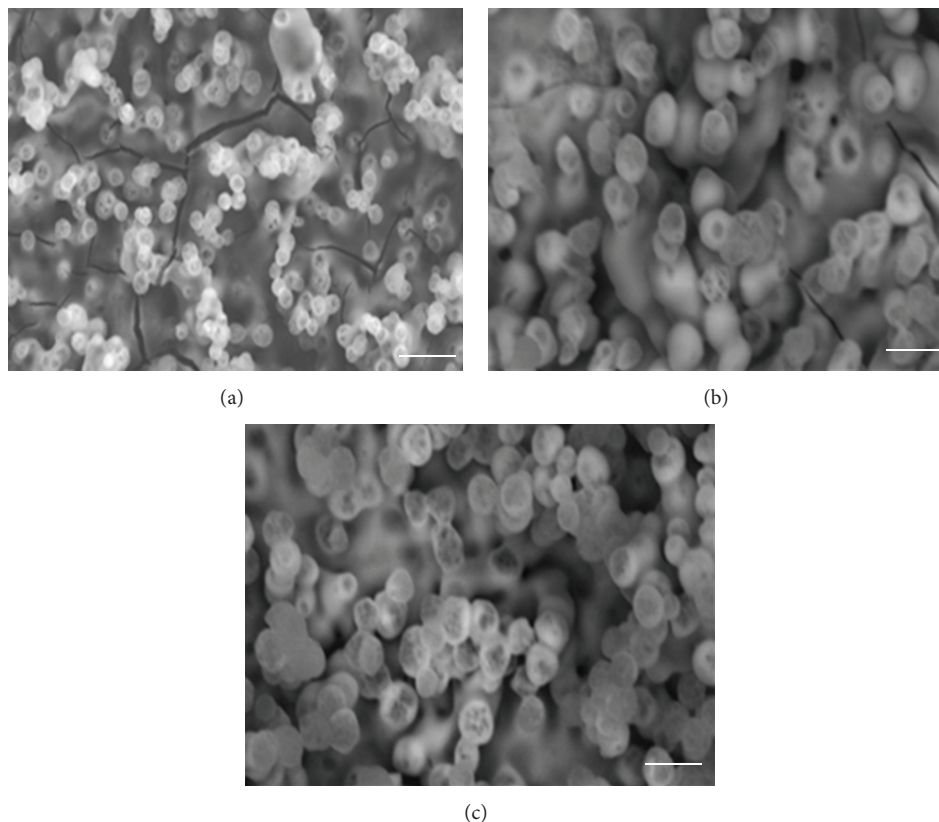


FIGURE 1: SEM micrographs of surface morphology of ZnAl_2O_4 films as a function of the T_s : (a) 300°C, (b) 450°C, and (c) 550°C. Bar = 100 nm.

with PBS, trypsinized, and the cell pellet was collected and diluted with DMEM culture medium to obtain the requisite cell concentration. The human osteoblastic cells at concentration of 1.5×10^3 cells/cm² were seeded onto ZnAl_2O_4 bulk and thin film nanostructured materials and incubated for 4 h and 24 h. The fluorescence was quantified using a fluorescein filter set with a Wallac Victor3 1420 spectrophotometer (Perkin-Elmer, Boston, MA, USA). The percentage cell adhesion was obtained by dividing the corrected (background subtracted) fluorescence of adherent cells by the total corrected fluorescence of control cells and multiplying by 100%. Conventional polystyrene 24-well culture plates were used as a control.

2.2.3. MTT Assay. Cell viability of human osteoblastic cells seeded at concentration of 1×10^4 cells/cm² onto ZnAl_2O_4 bulk and thin film nanostructured materials was checked by the MTT assay for 3, 5, and 7 days of culture. This assay is based on the ability of mitochondrial dehydrogenases of living cells to oxidize a tetrazolium salt (3-[4,5-dimethylthiazolyl-2-yl]-2,5-diphenyltetrazolium bromide), to an insoluble blue formazan product. The concentration of the blue formazan product is directly proportional to the number of metabolically active cells. The human osteoblastic cells seeded onto ZnAl_2O_4 bulk and thin film nanostructure materials at prescribed time were washed with PBS and incubated with fresh cultured medium containing 0.5 mg/mL of MTT for 4 h at 37°C in the dark. Then, the supernatant

was removed and dimethyl sulfoxide (DMSO) was added to each well. After 60 minutes of slow shaking, the absorbance was quantified by spectrophotometry at 570 nm with a plate reader. The culture medium during experimental time was changed every other day with fresh media.

2.2.4. Cell Morphology. For cytoskeletal organization of the human osteoblastic cells cultured onto ZnAl_2O_4 bulk and thin film nanostructured materials, the cells were seeded at concentration of 1×10^3 cells/cm² and incubated for 24 hours in DMEM cultured medium. After 24 hours, the samples were washed with PBS and fixed with 4% paraformaldehyde for 10 minutes at room temperature (RT), permeabilized with 0.2% Triton X-100 for 5 minutes, washed twice with PBS and incubated with α -actin antibody diluted 1:100 in 0.2% of bovine serum albumin (BSA)-PBS for 1 h at RT. The cells were then gently washed twice with 0.2% BSA-PBS and twice with PBS. Then, cells were incubated with FITC secondary antibody diluted 1:1000 in PBS for 1 hour. The cells were gently washed with PBS and visualized by means of indirect immunofluorescence (Axiophot, Carl ZeissR, Germany).

2.2.5. Statistical Analysis. Data are presented as mean standard deviation. Statistical analysis was performed on adhesion and MTT assay results using Student's *t*-test, and *P* value <0.05 was considered significant.

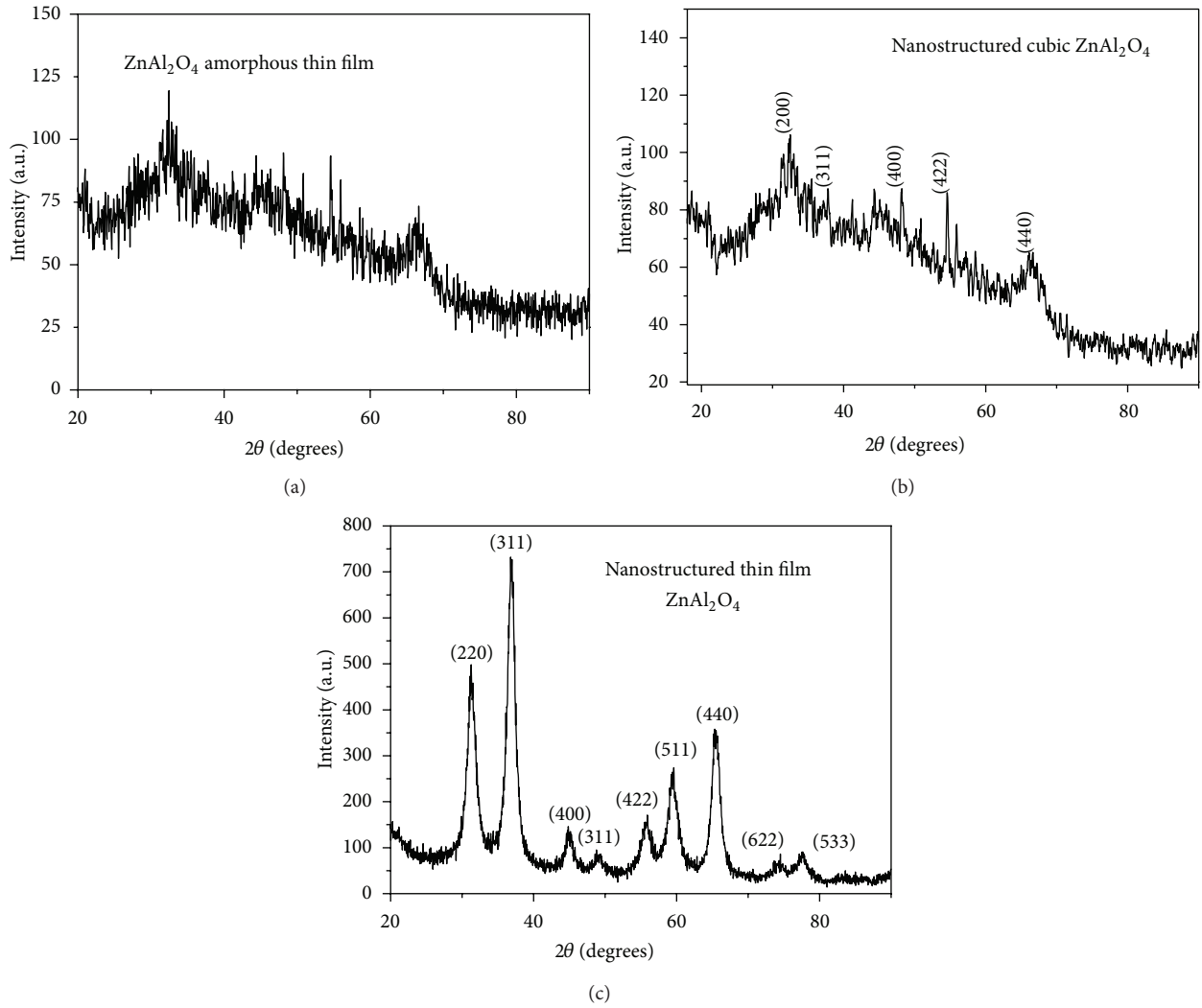


FIGURE 2: X-ray diffraction histograms of ZnAl₂O₄ thin films as a function of the T_s : (a) amorphous = 300°C, (b) nanostructured = 450°C, and (c) nanostructure = 550°C.

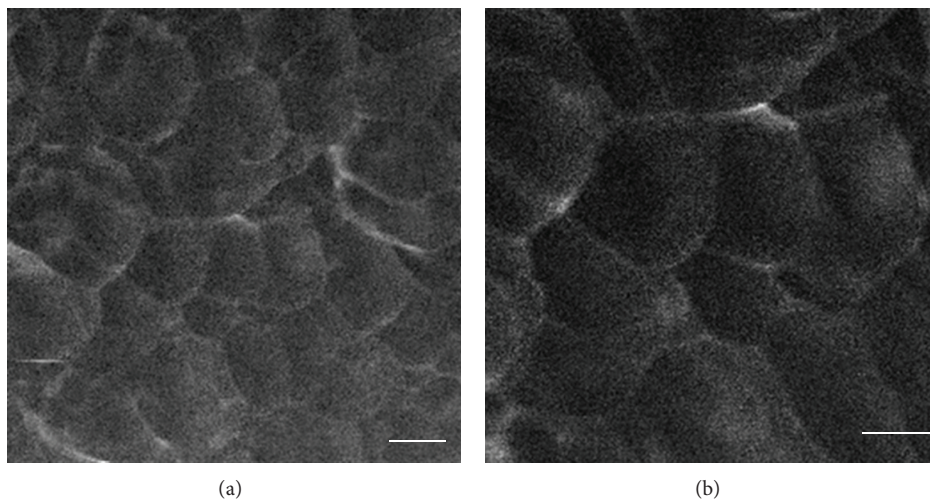


FIGURE 3: Surface morphology of the sintered pellets sample of ZnAl₂O₄. The surface is smooth, homogeneous (a), and without porous regions (b). Bar = 10 microns.

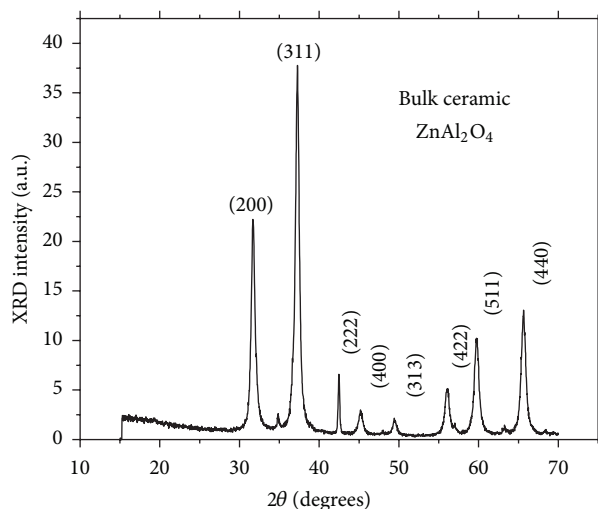


FIGURE 4: XRD of the bulk ceramic sample annealed at 600°C.

3. Results and Discussion

The surface morphology of ZnAl_2O_4 coatings deposited on glass substrates is presented in Figure 1. SEM micrographs show the samples deposited at 300°C Figure 1(a), 450°C Figure 1(b), and 550°C Figure 1(c). It is possible to observe rough but continuous coatings with good adherence to the substrate. This figure shows that the surface morphology of the layers depends on substrate temperature. Coatings deposited at 300°C and 450°C present some cracks. By increasing the substrate temperature to (500–550°C), the cracks disappear and a relatively more dense material is reached. These features could be explained because at higher substrate temperature, the deposited radicals are characterized by higher surface kinetic energy, which permits them better accommodation and consequently produces a better processed and compacted material.

At $T_s = 550^\circ\text{C}$, the thin film shows a nanogranular morphology with a great quantity of porous regions, which mimics the surface morphology of the human bone.

The chemical composition of the films deposited at substrate temperature of 550°C was determined by EDS, with the atomic percentages of Zn = 13.6, Al = 27.8, O = 57.1, and Cl = 1.50, which means that we have ZnAl_2O_4 ceramic compound of stoichiometric composition doped with 1.50 % of chlorine.

XRD measurements carried out on the ZnAl_2O_4 coatings deposited by spray pyrolysis technique are presented in Figures 2(a), 2(b), and 2(c). These XRD patterns are shown for ZnAl_2O_4 at these three different substrate temperatures: 300°C, 450°C, and 550°C. The zinc aluminate coatings remain in the amorphous state when deposited at substrate temperatures up to 400°C (Figure 2(a)); as the substrate temperature is increased to 450°C, some peaks corresponding to hexagonal phase of ZnO (zincite, ICDD Card File no. 36-1451) are observed in Figure 2(b). In case of the sample deposited at 550°C Figure 2(c), only a cubic spinel crystalline phase of ZnAl_2O_4 (gahnite) was found (ICDD Card File no.

05-0669 [24]). The calculated lattice parameters ($a = b = c = 8.0859 \text{ \AA}$) for the cubic spinel phase in the films deposited at 550°C are in agreement with the reported values ($a = b = c = 8.0848 \text{ \AA}$) [24]. Furthermore, it promoted the crystal growth of this material with a preferential (311) orientation normal to the coatings surface. Considerable peaks broadening can be observed due to the nanometric dimension of the grains in the thin film. By using the Debye-Scherrer formula for the broadening fitting curve XRD program, the particle size was evaluated. The average particle diameter was around $20 \pm 5 \text{ nm}$, considering that the grains are spheres.

The surface morphology of the polycrystalline ZnAl_2O_4 pellets sample obtained by chemical coprecipitation process is presented in Figure 3 and its XRD measurements pattern is shown in Figure 4. It is clear that this type of ceramic shows a smooth and homogeneous surface morphology without any observable porous region. Its average grain size is about $8.5 \pm 2.0 \mu\text{m}$.

The biomaterial surface interaction between scaffolds and tissue cells is a significant subject for biomaterials science. Information originating from this interaction is essential to aid the design and fabrication of new biocompatible materials [25]. Our results showed that when we culture osteoblastic cells on ZnAl_2O_4 nanostructured materials, the cell morphology had attached and undergone significant spreading, elongated demonstrating areas, where filopodia had intimately adapted with multiple cellular extensions on the surface of the ceramic (Figure 5(b)). In contrast, osteoblastic cells culture on ZnAl_2O_4 bulk materials showed neither or small elongation or extension (Figure 5(a)). These morphological results could be supported by the results of cell adhesion values after 4 and 24 h, presented as the cellular percentage of attached cells in relation to control tissue cultures plates. The cellular adhesion as the first step to assess the compatibility of the cell-material interaction surface was 60 to 80% greater on the ZnAl_2O_4 nanostructured material surface where it should be noted that the adherent values at all-time points were consistently higher when comparing with bulk ceramic surfaces (Figure 6). Statistical analyses indicated that there were statistically significant differences in the cell response, where osteoblastic cells attachment occurred preferred on the rough ceramic surface followed by the smooth surface ceramic. Moreover, it is important to remark that increased cellular attachment obtained on ZnAl_2O_4 bulk and 550°C thin film nanostructured materials is a good indicator that the surface is not toxic to the cells. We perform the cell viability test assessed by the MTT assay to confirm it. The results of the MTT assay are presented as the optical absorbance at 570 nm as shown in Figure 7. Both ZnAl_2O_4 nanostructure and bulk ceramics exhibited excellent biocompatibility. Among the two ceramics, it can be seen that cell viability is always higher on a nanostructured material than a bulk material, where we found high levels of MTT conversion and continue until day 7. This increment is directly proportional to the increase of metabolic active cells on the surface of ZnAl_2O_4 and inversely proportional to the toxicity effect of the surface topography of the material where significant differences in mean optical density are always presented as confirmed by Student's *t*-test. This increase in

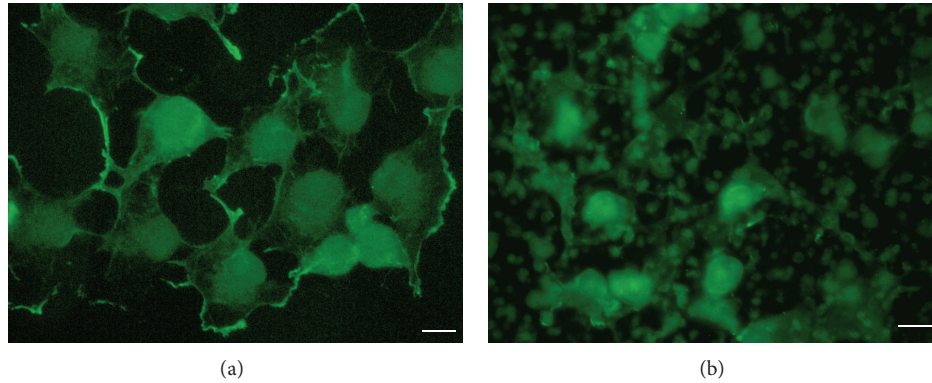


FIGURE 5: Cytoskeletal organization morphology micrographs of the attachment of osteoblastic cells after 24 h on (a) bulk ZnAl₂O₄ ceramic and (b) ZnAl₂O₄ thin film nanostructured ceramic at $T_s = 550^\circ\text{C}$. Bar = 20 μm .

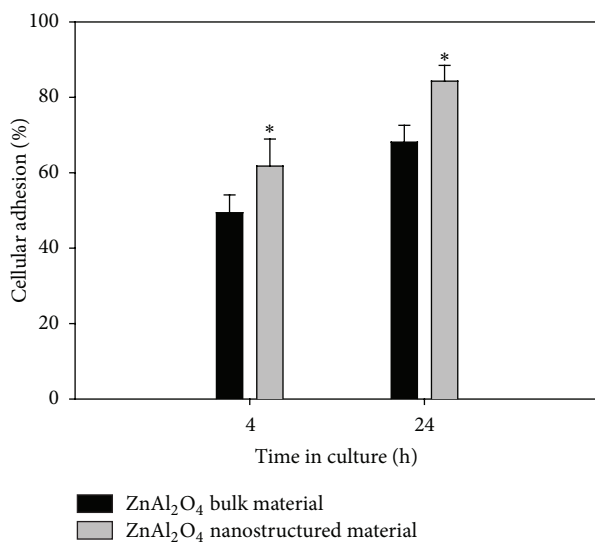


FIGURE 6: Quantitative cell adhesion of osteoblastic cells seeded on ZnAl₂O₄ (■) bulk material and (□) thin films nanostructure at $T_s = 550^\circ\text{C}$, after 4 and 24 h of culture, expressed as percent of cell attachment. Asterisk denotes significant differences ($P < 0.05$) between ceramic materials as determined by Student's t -test.

adhesion and viability by MTT activity of cells could be favored for the presence of ZnAl₂O₄ nanoparticle material. These results are in agreement with the idea that topography of extracellular microenvironment can influence cellular responses from attachment and migration to differentiation and production of new tissue [26–29]. Moreover, it has also been reported that surface energy is a more influential surface characteristic on cellular adhesion and proliferation [30, 31]. So the enhanced cellular adhesion and viability on ZnAl₂O₄ nanostructure ceramic could be due to the positive influence of the component of the surface energy. However, further studies are needed with these materials to fully understand the tissue cell-material interactions.

4. Conclusion

ZnAl₂O₄ nanostructure and bulk spinel ceramic have been evaluated for their *in vitro* biocompatibility to explore their

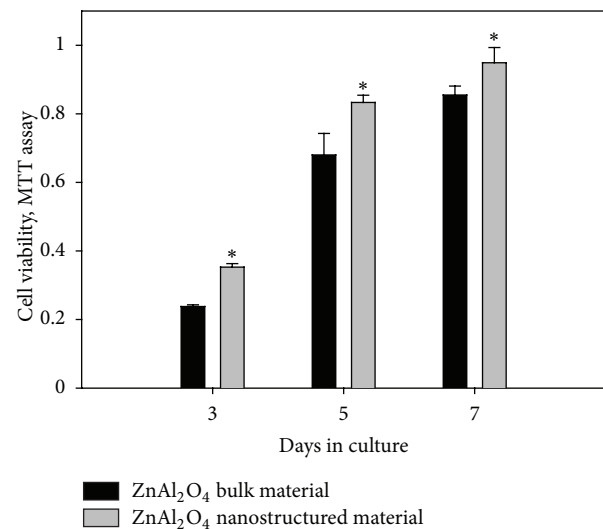


FIGURE 7: Cell viability determined by MTT assay after 3, 5, and 7 days of cell culture on ZnAl₂O₄ (■) bulk material and (□) thin films nanostructured at $T_s = 550^\circ\text{C}$. Error bars represent mean \pm SE, $n = 3$ cultures under each conditions. Asterisk denotes significant differences ($P < 0.05$) between ceramic materials as determined by Student's t -test.

potential to be used in dental implant and bone substitute applications. The *in vitro* attachment and morphological and viability responses of osteoblastic cells suggest that nanostructured ceramic appears to be the most conducive to cells compared to the bulk ceramic surface. The results of these studies could lead to a relatively new generation of bioceramics with surface characteristics specific to the needs of individual tissue types as bone or oral cavity.

Acknowledgments

The authors wish to thank Omar Novelo-Peralta, Raul Reyes, and Adriana Tejeda-Cruz from IIM-UNAM for their technical assistance during the course of this study. This study was supported by UNAM-DGAPA: (PAPIIT Grant no. 213912) and CONACYT (Grant no. 129780).

References

- [1] R. J. Hill, J. R. Craig, and G. V. Gibbs, "Systematics of the spinel structure type," *Physics and Chemistry of Minerals*, vol. 4, no. 4, pp. 317–339, 1979.
- [2] D. L. Anderson, "The earth as a planet: paradigms and paradoxes," *Science*, vol. 223, no. 4634, pp. 347–355, 1984.
- [3] S. K. Sampath, D. G. Kanhere, and R. Pandey, "Electronic structure of spinel oxides: zinc aluminate and zinc gallate," *Journal of Physics Condensed Matter*, vol. 11, no. 18, pp. 3635–3644, 1999.
- [4] S. Mathur, M. Veith, M. Haas et al., "Single-source sol-gel synthesis of nanocrystalline $ZnAl_2O_4$: structural and optical properties," *Journal of the American Ceramic Society*, vol. 84, no. 9, pp. 1921–1928, 2001.
- [5] T. El-Nabarawy, A. A. Attia, and M. N. Alaya, "Effect of thermal treatment on the structural, textural and catalytic properties of the $ZnO-Al_2O_3$ system," *Materials Letters*, vol. 24, no. 5, pp. 319–325, 1995.
- [6] H. Dinopoulos, R. Dimitriou, and P. V. Giannoudis, "Bone graft substitutes: what are the options?" *Surgeon*, vol. 10, no. 4, pp. 230–239, 2012.
- [7] C. Zink, H. Hall, D. M. Brunette, and N. D. Spencer, "Orthogonal nanometer-micrometer roughness gradients probe morphological influences cell behavior," *Biomaterials*, vol. 33, no. 32, pp. 8055–8061, 2012.
- [8] T. P. Kunzler, T. Drobek, M. Schuler, and N. D. Spencer, "Systematic study of osteoblast and fibroblast response to roughness by means of surface-morphology gradients," *Biomaterials*, vol. 28, no. 13, pp. 2175–2182, 2007.
- [9] T. P. Kunzler, C. Huwiler, T. Drobek, J. Vörös, and N. D. Spencer, "Systematic study of osteoblast response to nanotopography by means of nanoparticle-density gradients," *Biomaterials*, vol. 28, no. 33, pp. 5000–5006, 2007.
- [10] D. Khang, J. Choi, Y. M. Im et al., "Role of subnano-, nano- and submicron- surface features on osteoblast differentiation of bone marrow mesenchymal stem cells," *Biomaterials*, vol. 33, no. 26, pp. 5997–6007, 2012.
- [11] P. Ducheyne and Q. Qiu, "Bioactive ceramics: the effect of surface reactivity on bone formation and bone cell function," *Biomaterials*, vol. 20, no. 23-24, pp. 2287–2303, 1999.
- [12] M. Navarro, A. Michiardi, O. Castaño, and J. A. Planell, "Biomaterials in orthopaedics," *Journal of the Royal Society Interface*, vol. 5, no. 27, pp. 1137–1158, 2008.
- [13] C. Wu, J. Chang, and W. Zhai, "A novel hardystonite bioceramic: preparation and characteristics," *Ceramics International*, vol. 31, no. 1, pp. 27–31, 2005.
- [14] Y. Ramaswamy, C. Wu, H. Zhou, and H. Zreiqat, "Biological response of human bone cells to zinc-modified Ca-Si-based ceramics," *Acta Biomaterialia*, vol. 4, no. 5, pp. 1487–1497, 2008.
- [15] H. Tapiero and K. D. Tew, "Trace elements in human physiology and pathology: zinc and metallothioneins," *Biomedicine and Pharmacotherapy*, vol. 57, no. 9, pp. 399–411, 2003.
- [16] C. J. Boehlert and K. Knittel, "The microstructure, tensile properties, and creep behavior of Mg-Zn alloys containing 0–4.4 wt.% Zn," *Materials Science and Engineering A*, vol. 417, no. 1-2, pp. 315–321, 2006.
- [17] M. Yamaguchi, H. Oishi, and Y. Suketa, "Stimulatory effect of zinc on bone formation in tissue culture," *Biochemical Pharmacology*, vol. 36, no. 22, pp. 4007–4012, 1987.
- [18] Y. Tokudome and M. Otsuka, "Possibility of alveolar bone promotion enhancement by using lipophilic and/or hydrophilic zinc related copound in zinc deficient osteoporosis rats," *Biological & Pharmaceutical Bulletin*, vol. 35, no. 9, pp. 1496–1501, 2012.
- [19] A. Ito, H. Kawamura, M. Otsuka et al., "Zinc-releasing calcium phosphate for stimulating bone formation," *Materials Science and Engineering C*, vol. 22, no. 1, pp. 21–25, 2002.
- [20] Y. Tokudome, A. Ito, and M. Otsuka, "Effect of Zinc-containing b-tricalcium phosphate nanoparticles injection on jawbone mineral density and mechanical strength of osteoporosis model rats," *Biological & Pharmaceutical Bulletin*, vol. 34, no. 8, pp. 1215–1218, 2011.
- [21] N. Saha, A. K. Dubey, and B. Basu, "Cellular proliferation, cellular viability, and biocompatibility of HA-ZnO composites," *Journal of Biomedical Materials Research B*, vol. 100, no. 1, pp. 256–264, 2012.
- [22] J. C. Vigiúe and J. Spitz, "Chemical vapor deposition at low temperaturas," *Journal of the Electrochemical Society*, vol. 122, no. 4, pp. 585–588, 1975.
- [23] H. Arzate, M. A. Alvarez-Pérez, M. E. Aguilar-Mendoza, and O. Alvarez-Fregoso, "Human cementum tumor cells have different features from human osteoblastic cells in vitro," *Journal of Periodontal Research*, vol. 33, no. 5, pp. 249–258, 1998.
- [24] Power diffraction file card No. 05-0669, "International center for Diffraction Data," 1990.
- [25] S. Chung and M. W. King, "Design concepts and strategies for tissue engineering scaffolds," *Biotechnology and Applied Biochemistry*, vol. 58, no. 6, pp. 423–438, 2011.
- [26] O. Adamopoulos and T. Papadopoulos, "Nanostructured bioceramics for maxillofacial applications," *Journal of Materials Science*, vol. 18, no. 8, pp. 1587–1597, 2007.
- [27] M. J. Dalby, D. McCloy, M. Robertson et al., "Osteoprogenitor response to semi-ordered and random nanotopographies," *Biomaterials*, vol. 27, no. 15, pp. 2980–2987, 2006.
- [28] L. L. Hench and I. Thompson, "Twenty-first century challenges for biomaterials," *Journal of the Royal Society Interface*, vol. 7, no. 4, pp. S379–S391, 2010.
- [29] D. F. Williams, "On the mechanisms of biocompatibility," *Biomaterials*, vol. 29, no. 20, pp. 2941–2953, 2008.
- [30] B. Feng, J. Weng, B. C. Yang, S. X. Qu, and X. D. Zhang, "Characterization of surface oxide films on titanium and adhesion of osteoblast," *Biomaterials*, vol. 24, no. 25, pp. 4663–4670, 2003.
- [31] P. Thevenot, W. Hu, and L. Tang, "Surface chemistry influences implant biocompatibility," *Current Topics in Medicinal Chemistry*, vol. 8, no. 4, pp. 270–280, 2008.

Research Article

Obtaining of Sol-Gel Ketorolac-Silica Nanoparticles: Characterization and Drug Release Kinetics

T. M. López Goerne,^{1,2,3} M. G. López García,^{1,2} G. Rodríguez Grada,^{1,2} I. Ortiz Pérez,^{1,2} E. Gómez López,⁴ and M. A. Alvarez Lemus²

¹ *Laboratorio de Nanotecnología y Nanomedicina, Departamento de Atención a la Salud, Universidad Autónoma Metropolitana Xochimilco, Calzada del Hueso 1100, Col. Villa Quietud, Delegación Coyoacán, 04960 México, DF, Mexico*

² *Laboratorio de Nanotecnología, Instituto Nacional de Neurología y Neurocirugía "Manuel Velasco Suárez", Avenida Insurgentes sur 3877, Col. La Fama, 14269 Tlalpan, DF, Mexico*

³ *Department of Chemical and Biomolecular Engineering, Tulane University, New Orleans, LA 70118, USA*

⁴ *Facultad de Ciencias, Universidad Nacional Autónoma de México, Avenida Universidad 3000, Circuito Exterior S/N Delegación Coyoacán, Ciudad Universitaria, 04510 México, DF, Mexico*

Correspondence should be addressed to M. A. Alvarez Lemus; maalvarez@innn.edu.mx

Received 24 August 2012; Accepted 1 November 2012

Academic Editor: Yan-Yan Song

Copyright © 2013 T. M. López Goerne et al. This is an open access article distributed under the Creative Commons Attribution License, which permits unrestricted use, distribution, and reproduction in any medium, provided the original work is properly cited.

Nonsteroidal anti-inflammatory drugs (NSAIDs) are among most commonly prescribed medications worldwide. NSAIDs play an important role due to their pronounced analgesic potency, anti-inflammatory effects, and lesser side effects compared to opioids. However, adverse effects including gastrointestinal and cardiovascular effects seriously complicate their prolonged use. In the present work we prepare SiO₂-based nanoparticles with ketorolac, for controlled release proposes. The nanomaterials were prepared by the sol-gel technology at acidic conditions and two different water/alcoxide ratios were used. FTIR spectroscopy was performed in order to characterize the solids and drug-SiO₂ interactions. Thermal analysis and nitrogen adsorption isotherms showed thermal stability of the drug and confirmed the presence of particles with high surface area. Transmission electron micrographies of the samples showed the nanosize particles (20 nm) forming aggregates. Drug release profiles were collected by means of UV-Vis spectroscopy and kinetic analysis was developed. Release data were fitted and 1:8 sample showed a sustained release over ten hours; 90% of the drug was delivered at the end of the time.

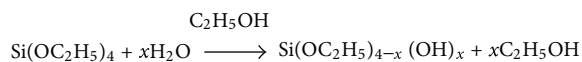
1. Introduction

Nanotechnology drug delivery, diagnosis, and drug development represent the change in medicine in 21st century. This field is an area that will produce significant results, in this way the drug is controlled during days or even weeks, depending on the disease to treat [1]. Nanoparticulate drug delivery vehicles can be organic or inorganic solids but biocompatible and nontoxic. These novel systems allow drug absorption in a controlled way and with less adverse side effects [2].

Nonsteroidal anti-inflammatory drugs (NSAIDs) are among most commonly prescribed medications worldwide [3]. Approximately 20% of people older than 65 years have been prescribed NSAIDs [4]. In acute pain as headache,

stomach ache, or flu, NSAIDs play an important role due to their pronounced analgesic potency, anti-inflammatory effects, and lesser side effects compared to opioids [5, 6]. However, adverse effects including gastrointestinal (GI) and cardiovascular (CV) seriously complicate their prolonged use [7].

Ketorolac tromethamine (KT), Figure 1, is a pyrrolizine carboxylic acid derivative of NSAIDs with potent analgesic and moderate anti-inflammatory activity, a relatively favorable therapeutic agent for the management of moderate to severe pain [8, 9]. The beneficial effects of KT are probably due to its ability to block prostaglandin synthesis by preventing the conversion of arachidonic acid to the endoperoxides [10].



SCHEME 1: Hydrolysis of TEOS.

For instance, weight by weight KT proved to be 50 times more potent than naproxen in analgesia models but only 3 times more potent in inflammation models [11]. This remarkable dissociation between analgesic and anti-inflammatory effects provided the basis for the development of the drug as excellent anti-inflammatory and analgesic. In clinical settings however ketorolac has been involved as a contributing cause of increased postoperative bleeding, renal failure, and gastritis; the severity of these side effects is probably dose related [12].

For these reasons, many attempts to develop novel formulation strategies to deliver KT had been made. Sinha and Trehan [13] prepared drug-loaded polycaprolactone and poly lactic-co-glycolic acid microspheres, Rokhade et al. [14] developed semi-interpenetrating polymer network microspheres of gelatin and sodium carboxymethyl cellulose, and recently, Genc and Jalvand [15] produced controlled release hydrophilic matrix tablets.

The use of mesoporous silica nanoparticles offers a suitable method to deliver drugs toward specific tissues or cells depending on drug properties [16]. Sol-gel inorganic nanoparticles exhibit significantly higher surface area and porosity [17] which means more available surface to place molecules of interest. One of the main advantages of sol-gel process is that materials exhibit special features like highly hydroxylated surface which has demonstrated to be one facile method to achieve functionalized surfaces. Additionally, sol-gel process provides the opportunity to release a great variety of biomolecules, medicines, or compounds from the oxide structure, while functionalization or surface modification is relatively easy.

Sol-gel chemistry uses neutral, acidic, or basic conditions to achieve hydrolysis and condensation of numerous silane monomers $\equiv\text{Si}-\text{O}$ and $\text{O}-\text{Si}-\text{OH}$ (Scheme 1) [17–20].

At present, a great deal of emphasis is being placed on the development of controlled or sustained release forms for the drug as this would help in achieving the required therapeutic efficacy and better tolerance. The main goal of this study was to develop ketorolac silica reservoir (ketorolac- SiO_2) delivery system using sol-gel method.

2. Experimental

2.1. Materials. Tetraethoxysilane (TEOS) 98%, was purchased from Sigma-Aldrich. Ketorolac tromethamine ($\text{C}_{15}\text{H}_{13}\text{NO}_3$, MW 255.27 g/mol) by Lyomont laboratories was also purchased, all organic solvents were purchased from Sigma-Aldrich.

2.2. Preparation of Reservoir. Silica reservoir was made by sol-gel process at room temperature using two water alkoxide molar ratios 1:8 and 1:4; the same ethanol:alkoxide

ratios were used. Preparation was as follows: appropriated amounts of water and ethanol were placed and mixed in a three neck round-bottom flask. Then 18.5 mL of TEOS was dropwise simultaneously but in a different neck with the drug (6 mg/g SiO_2). The mixture was left under stirring for 14–21 days. Other SiO_2 nanoparticles were prepared under the same conditions but without analgesic. Then, dried material was crushed in an agata mortar.

2.3. Characterization. Infrared absorption spectra, of the nanomaterials were obtained on IRAffinity-1 FTIR system. A tablet with the different samples (5%wt) was pressed together with 95% wt of KBr (2000 ton/in²).

Thermograms were carried out using a Simultaneous Thermal Analyzer STA i-1000. Samples were placed in a platinum pan and heated at a rate of 10°C/min, in N_2 atmosphere from room temperature to 800°C.

2.4. Morphology Study. High-resolution transmission electron microscopy (TEM) images were obtained using a TEM microscope, JEOL JEM-2100F, operated at 200 kV and equipped with an energy dispersive spectroscopic (EDS) microanalysis system (Oxford). The images were obtained using a Gatan Orius camera.

2.5. Nitrogen Adsorption Measurements. Nitrogen adsorption-desorption isotherms were obtained using a Micromeritics Belsorp II, Bell Japan Inc The Brunauer-Emmett-Teller (BET) method was used to calculate specific surface areas (S_{BET}). Pore volumes and pore size distributions were obtained using BJH method.

2.6. Controlled Drug Release. A tablet made of each Ketorolac- SiO_2 nanomaterial (1:4 and 1:8 ratios) was placed into a glass with deionized water (50–75 mL). Sampling was performed at different periods of time over a total of 200 hours. Analysis was performed using ultraviolet spectroscopy (Cary-1 UV-visible, Varian) by following the increase in main absorption bands reported for ketorolac. After measurements, samples were returned to the glass to maintain constant volume. A calibration curve was performed and absorbance spectra were collected. In order to calculate drug concentration Lambert-Beer law was used. Drug release curves were obtained by plotting cumulative drug concentration versus time. Determinations were made by duplicate.

2.7. Applied Methods to Compare Drug Release Profiles. Ketorolac release kinetics from each nanomaterial was analyzed by several mathematical models. Depending on these estimations, suitable mathematical models to describe dissolution profiles were determined. The following plots were made: dissolution % drug release versus time (zero-order kinetic model); Ln dissolution % drug remaining versus time (first-order kinetic model); dissolution % drug release versus square root of time (Higuchi model); cube root of drug % remaining in matrix versus time (Hixson-Crowell cube root law); and dissolution % drug release versus time (hyperbola).

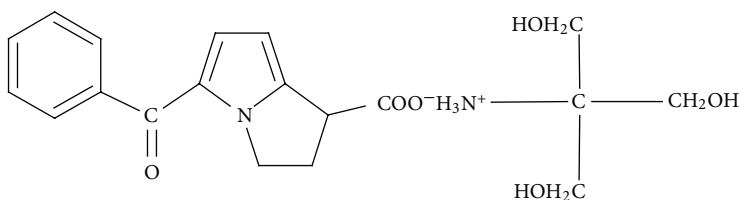
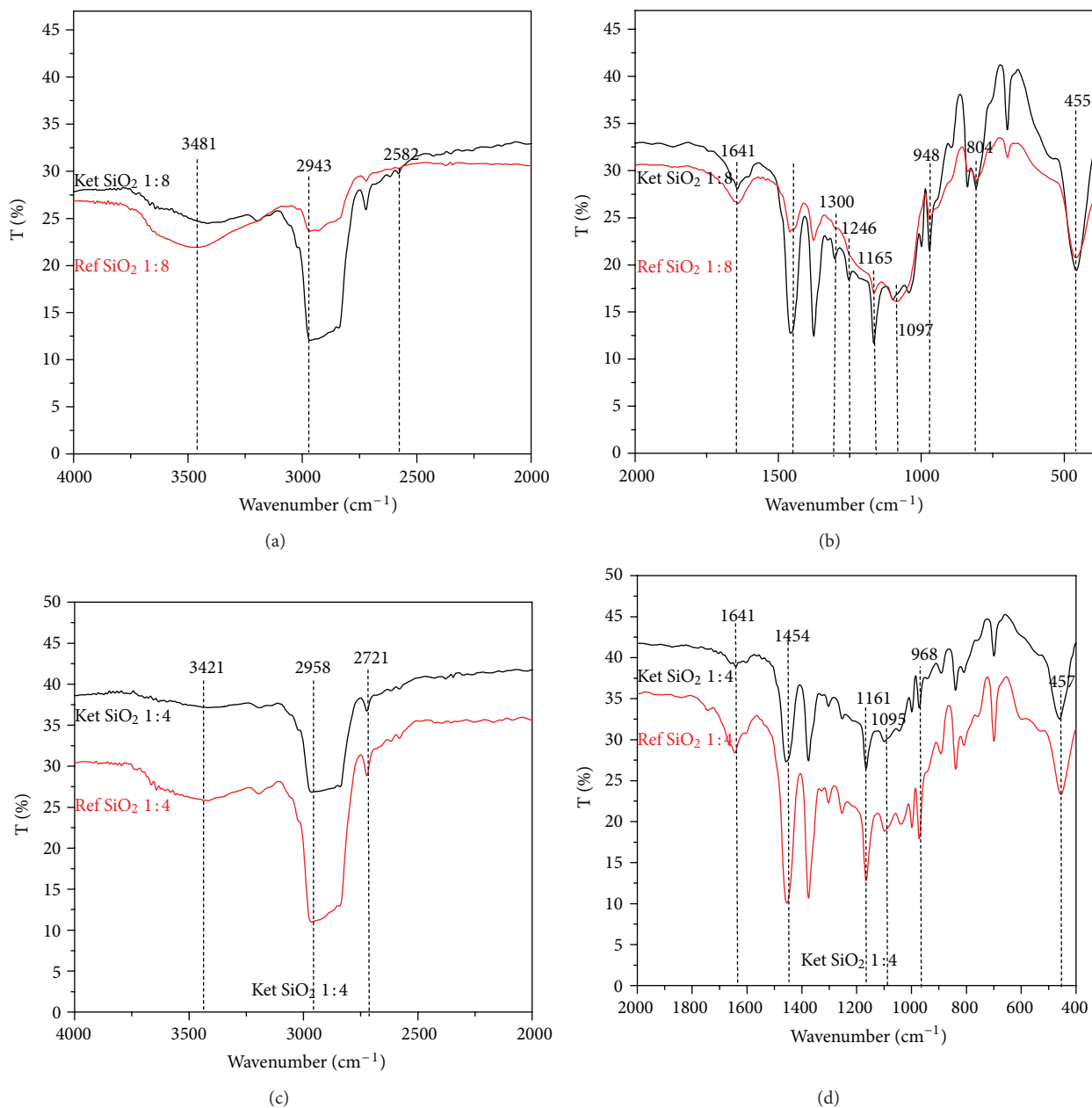


FIGURE 1: Structure of Ketorolac tromethamine.

FIGURE 2: IR spectra of (a) and (b) 1:8 ratio; (c) and (d) 1:4 ratio SiO₂ based materials.

3. Results and Discussion

3.1. Characterization. Figure 2 shows the most distinctive infrared absorption bands of silica for both ratios. In the 3500–3200 cm⁻¹ region, the O–H stretching band due to

residual water and Si–OH vibration was observed, this is typical in sol-gel materials, and the presence of O–H from methanol groups of the drug contributes to this band. Presence of adsorbed water is confirmed by the appearance of a band around 1641 cm⁻¹ in all the samples. The signals

centered at 455 and 457 cm^{-1} are related with the Si–O–Si bond deformation. The band around 1100 cm^{-1} is split into two bands at 1165 and 1097 cm^{-1} for the 1:8 material and at 1161 and 1095 cm^{-1} for 1:4 ratio; these correspond to stretching vibrations of Si–O–Si bonds. At 804 and 810 cm^{-1} we observed of Si–O⁻ flexion vibrations for 1:8 and 1:4 ratios, respectively. Si–OH stretching bands were observed at 948 and 968 cm^{-1} , these results are similar to those reported by Gonz ales et al. [18] and Kalampounias [21], no absorption bands of Ketorolac can be clearly assigned, since most of the signals due to the bonds of the drug are overlapped white silica bands. However some features are slightly distinguished; a more intense band was observed at 1450 cm^{-1} for Ketorolac-SiO₂ 1:8 and at 1454 cm^{-1} for Ketorolac-SiO₂ 1:4. In this region C=C ring antisymmetric elongation can be detected, this band is less intense in both silica references due to in those samples there still remains residual ethanol from the synthesis, so the band we observed corresponds to O–H deformation.

TGA curves are shown in Figure 3. Weight loss was very similar for all samples. For 1:8 ratio, the first loss was about 5% for Ketorolac-SiO₂ and ca. 8% for the reference around from room temperature to 150°C. This first gradual loss is associated with residual ethanol of the synthesis, and dehydration from both silica and the drug [22]. A second loss was recorded around 168°C (ca. 3%) in Ketorolac-SiO₂, this can be due to decomposition of tromethamine salt [23], the final gradual loss from 200 to 500°C is attributable to the lost of structural OH groups from silica.

When we compared TGA in both water ratios, the main difference is that silica references initially loss more weight than those nanomaterials with ketorolac; this can be explained due to the time of aging in both samples, since drug-loaded silica required higher time than silica alone. Regarding to the water ratios, the difference due to the amount of water is barely noticeable.

3.2. TEM and EDS of Reservoirs. The surface morphology of the Ketorolac-SiO₂ reservoirs was studied by transmission electron microscopy. The samples were placed on a cooper grid with a holey carbon support film. Several areas of the sample were photographed using the bright field technique (Figure 4), where the crystalline parts in Bragg orientation appear dark and the amorphous or not Bragg oriented parts appear bright [24], with a 200 kV electron beam.

The micrographs showed aggregates formations of SiO₂ in the drug-silica nanomaterial, with particle size of 20–100 nm approximately; due to electrostatic forces between these particles, agglomeration occurs, giving rise to nanoparticles collection, similar to previously reported by Uddin et al. [25]. The images suggest no Ketorolac presence in the crystalline Silica formations surface, in comparison with the reference sample.

The EDS was obtained from different large groups of particles; several hundred nanometers wide showing and confirming the nanomaterial are silica pure not only in the surface, but also in the whole structure. The dispersive energy bands shown are purely from silicon and oxygen without any

TABLE I: N₂ adsorption parameters.

Sample	S _{BET} (m ² /g)	V _P (cm ³ /g)	R _p (nm)
SiO ₂ 1:4	485	0.40	1.64
Ketorolac-SiO ₂ 1:4	26	0.20	6.95
SiO ₂ 1:8	532	0.26	1.64
Ketorolac-SiO ₂ 1:8	95	0.60	1.64

peak overlapping (Figure 6) with some peaks, in the case of the reference, due to the dispersive energy of the Cu grid (around 1, 8, and 9 keV) where the sample is sustained, and for that must be ignored.

3.3. Surface Analysis Using Nitrogen Adsorption-Desorption.

N₂ adsorption-desorption isotherms of the reservoirs measured at 77 K are shown in Figure 7; it can be clearly noticed that introducing Ketorolac modifies obtained isotherm. In both cases (1:8 and 1:4) ketorolac-SiO₂ materials showed lower adsorption, because drug molecules fill the pores, blocking available space to nitrogen molecules to measure real surface area; this is confirmed by S_{BET} values (Table 1). Isotherm of the sample ketorolac-SiO₂ 1:8 showed a type III according to IUPAC classification. In this case, ketorolac molecules showed weak interaction with nitrogen; thus adsorption of high amount of N₂ is not achieved and no significant hysteresis was observed. The 1:4 ketorolac sample showed similar behavior although with a slight hysteresis, however as in reference sample, adsorbed volume is lower than 1:8 material, which means that when a larger ratio of water is used, higher porosity is obtained. In the references samples, isotherms are type IV. Microporosity of the samples can be confirmed by TEM images (Figures 4(g) and 5(d)).

Pore size distributions showed a wide distribution for references; nevertheless we must consider the influence of adsorbed drug in pore occlusion, while in references we clearly observe a sharp peak around 2 nm. These results are comparable with those reported by Guo et al. [26].

The BET surface area values observed in both references were between 620–800 and both ketorolac-SiO₂ samples exhibited less area values, confirming the presence of drug inside and over the surface of the material. Pore size distribution (PSD) was estimated from desorption branch using BJH method (Figure 8). In pure silica, when we used 1:8 ratio, a narrow distribution centered around 1.6 nm is observed, while in 1:4 ratio material, bimodal behavior with a second peak at 2.7 nm occurs. Incorporation of drug causes pore occlusion limiting adsorptive access and reducing N₂ adsorption. In ketorolac SiO₂ 1:8, a wide but small distribution from 14 to 22 nm (inset) can be observed, in the other sample (1:4) a minimal volume was adsorbed. These results are in agreement with observations made from corresponding isotherms.

3.4. In Vitro Drug Release. Several mathematical models are used to evaluate the kinetics of drug release from pharmaceutical formulations. The model that best fits the obtained data is selected based on the correlation coefficient (*r*) value.

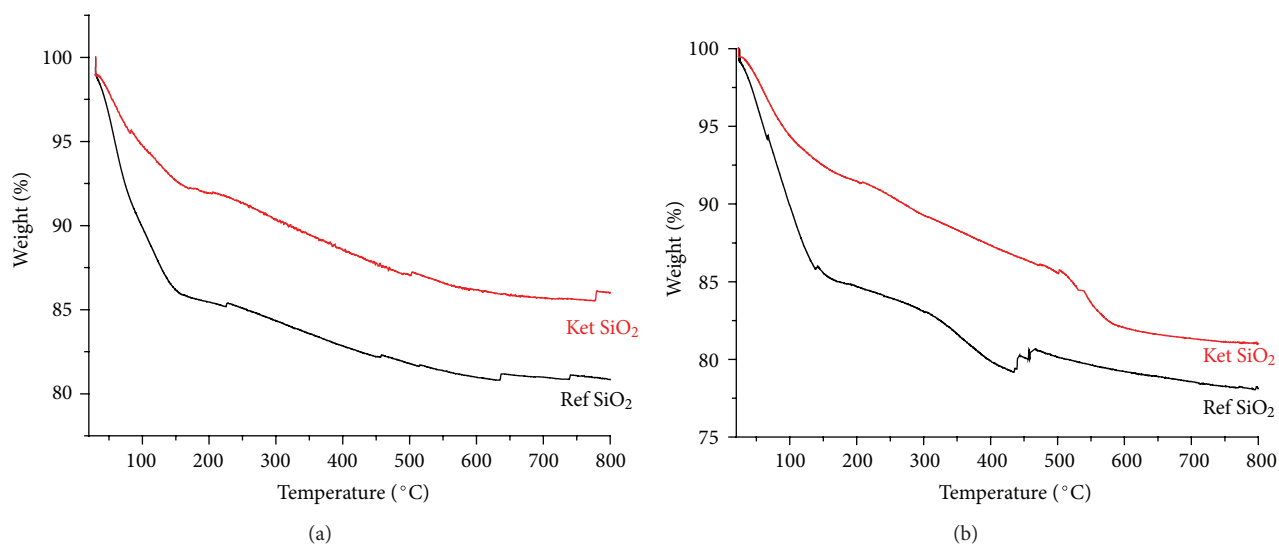


FIGURE 3: TGA curves of (a) 1:8 and (b) 1:4 samples.

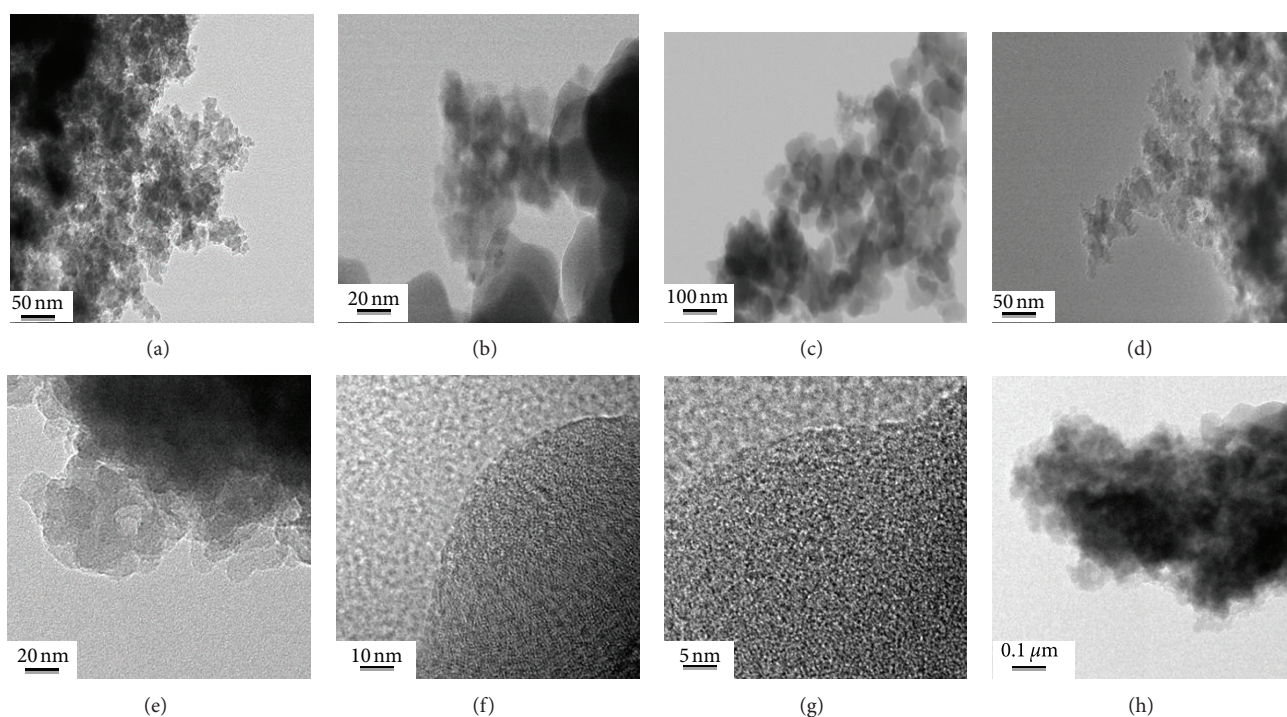


FIGURE 4: TEM images of ketorolac-SiO₂ 1:8 in the first four images and of reference-SiO₂ 1:8 in the next four images.

Several attempts have been made in order to avoid adverse side effects from oral administration of ketorolac, as the work of Genc and Jalvand [15] where they used hydrophilic matrix and achieved a slow release during 7 hours, another example is the use of microcapsules most of them made of Eudragit [27], and release the drug for no longer than 10 hours. Release profile of both Ketorolac-SiO₂ samples is different from each other (Figure 9). The cumulative % drug release from 1:4 was two times faster than 1:8 sample (Figure 10). This is probably due to more drug molecules being surface adsorbed

in ketorolac SiO₂ 1:4, and these are weakly bonded to the silica surface, releasing them more easily, and hence release time is shorter. For ketorolac SiO₂ 1:8 we observed that 90% of the drug was released after 200 hr. (Figure 9(a)).

In order to fit data to mathematical models, we applied five dissolution-diffusion kinetic models (zero-order, first-order, Higuchi, Hixon-Crowell and hyperbola) and calculated the corresponding kinetic parameters and linear correlation coefficients (R_2), these values are showed in Tables 2 and 3.

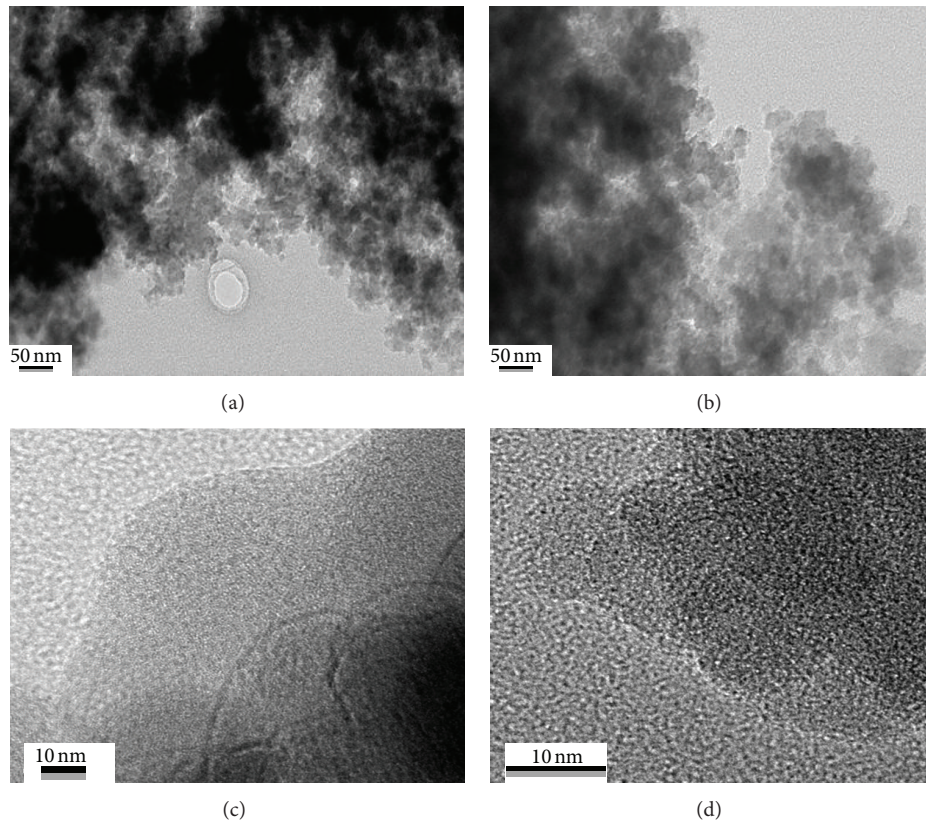


FIGURE 5: TEM images of 1: 4 (a), (b) Ketorolac-SiO₂ and (c), (d) reference-SiO₂.

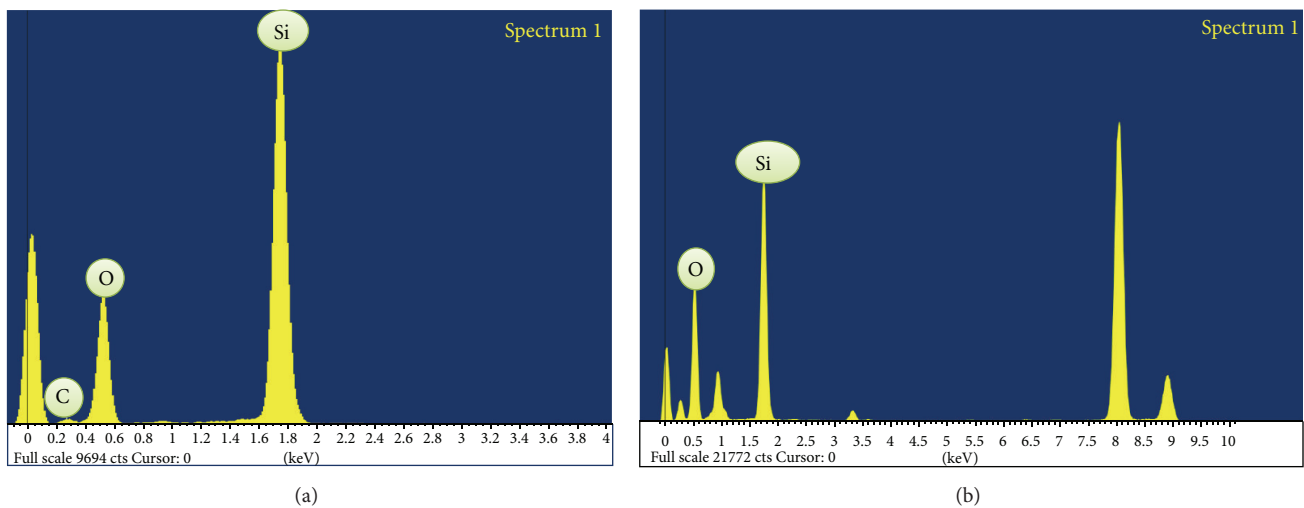


FIGURE 6: EDS spectra of Ketorolac SiO₂ 1: 8 (a) and Reference SiO₂ 1: 8 (b).

In general, the zero-order-first-order, Higuchi, and Hixson-Crowel models are not suitable to explain the controlled drug release data obtained in this study. The plots do not fit linear relationships and also have low correlation coefficients ($R_2 < 0.8$). The hyperbola model fits the release data much better, with linear correlation coefficients of $R_2 > 0.9$ for both reservoirs; the rate of drug release shows a hyperbole not dependent on the concentration.

The difference in drug release is not only attributed to the presence of nanosized pores. The presence of a small amount of mesopores in the 1:4 material (in pure SiO₂) implies that drug molecules can be occluded more easily in wider pores and release occurs faster than in micropores contributing to higher release rate. Also, during synthesis, considerable amount of adsorbed drug on particle surface might contribute to drug release in the initial phase.

TABLE 2: Linearization coefficients obtained from in vitro release of Ketorolac from SiO₂.

Reservoir	Zero-order $Q_t = Q_0 + K_0t$	First-order $Q_t = \ln Q_0 - K_1t$	Higuchi $Q_t = k_Ht^{1/2}$	Hixon-crowel $W_0^{1/3} - W_t^{1/3} = K_s t$	Hyperbola $a * x/(b + x)$
Ketorolac SiO ₂ 1: 8	0.4183	0.6809	0.5980	0.5712	0.9651
Ketorolac SiO ₂ 1: 4	0.7496	0.9664	0.8644	0.8919	0.9516

Q_t : amount of drug released in time t .
 Q_0 : initial amount of drug in the tablet.
 K_0, K_1, k_H, K_s : release rate constants.
 b : shape parameter.
 a : scale parameter.

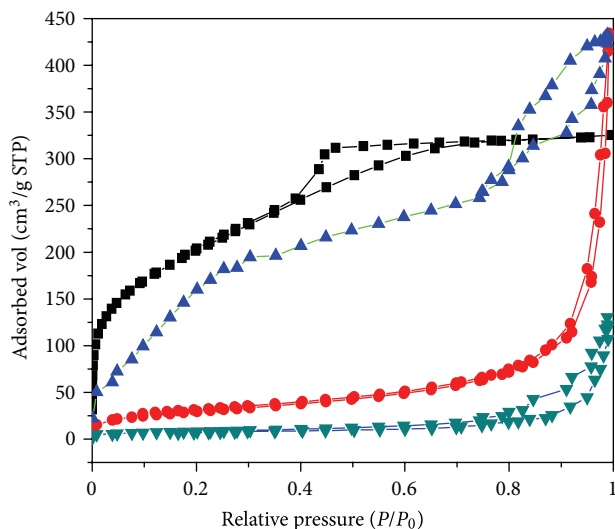


FIGURE 7: Nitrogen adsorption-desorption isotherms for the reservoirs at different stoichiometric relation as follows: (—■—) reference-SiO₂ 1: 8, (—●—) ketorolac-SiO₂ 1: 8, (—▲—) Reference SiO₂ 1: 4, and (—▼—) Ketorolac SiO₂ 1: 4.

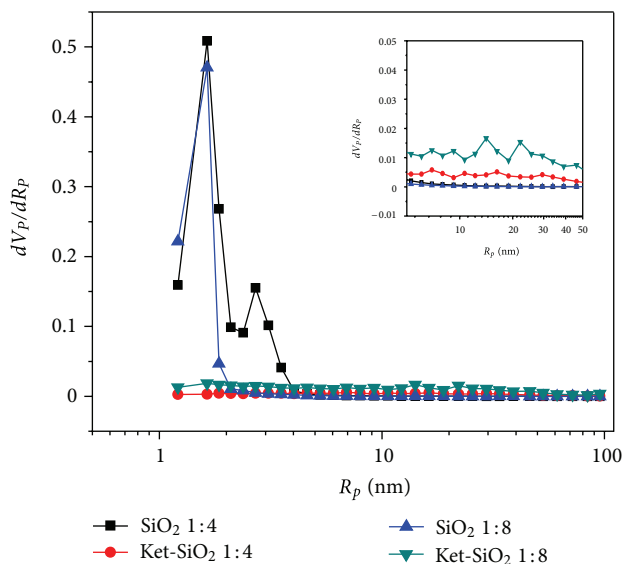
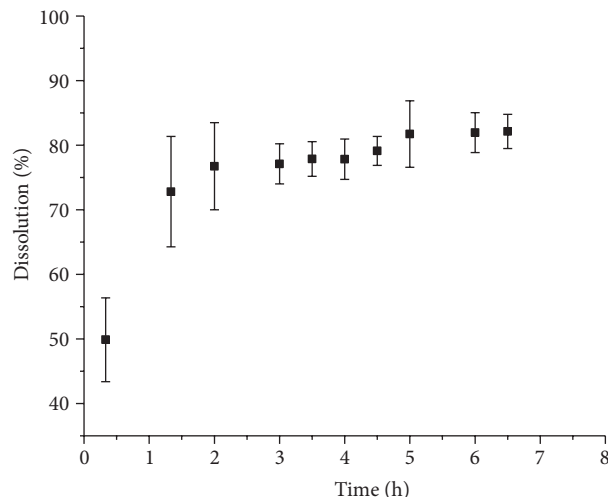
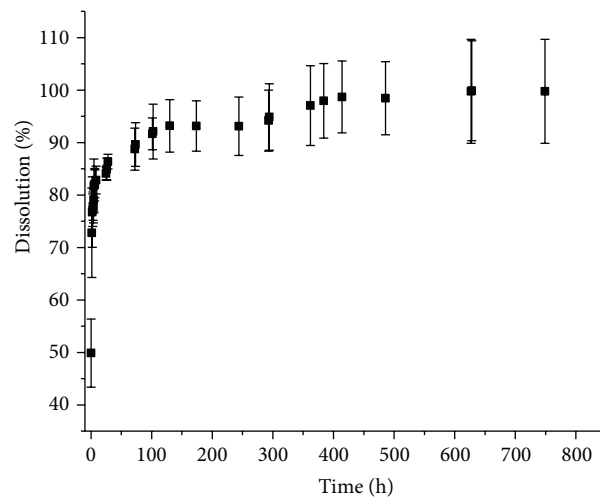


FIGURE 8: Pore size distribution of the SiO₂ materials.



(a)



(b)

FIGURE 9: *In vitro* release profile of ketorolac from SiO₂ 1: 8 reservoir (a) first 8 hours and (b) full time.

4. Conclusion

The development of new pharmaceutical formulations to enhance the therapeutic effect of conventional drugs is a rising area. Most micro- and nanomaterial used for this purposes are organic polymers; however since most of them

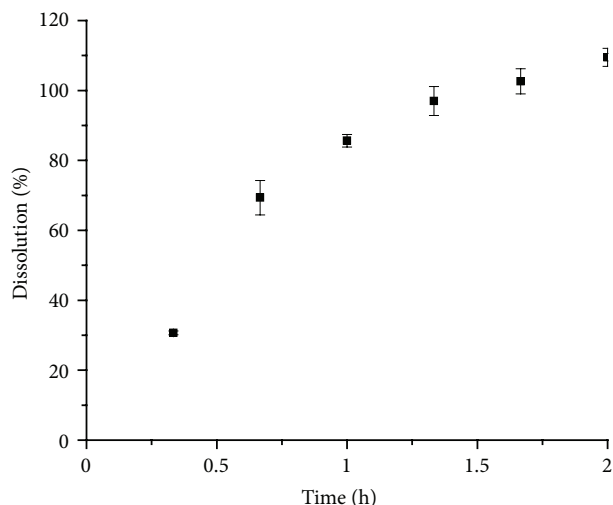


FIGURE 10: Release profile from SiO₂ 1:4.

TABLE 3: Drug release rates calculated for the different mathematical models.

Mathematical model	Ketorolac SiO ₂ 1:4	Ketorolac SiO ₂ 1:8
Zero-order [%/h]	30.51	0.09563
First-order [h]	3.057	0.00677
Higuchi [%]	72.97	1.69
Hixon-Crowell [h ⁻¹]	0.5364	0.0081
Hyperbola [%/h]	176.62	88.01

are commercially available, less control over their physical and chemical properties can be achieved. In order to bypass their limitations, alternative nanostructured materials like silica can be used. We synthesized silica nanoparticles with ketorolac for drug release. The best molar ratio was 1:8, since 80% of the drug is released at the 10 hours with a slower rate in the following hours reaching the 90% at the end of the time. Although 1:4 material released much faster, the behavior of 1:8 material was more homogeneous. Both systems represent an alternative to deliver ketorolac in a more controlled way. Sol-gel process is a potential method to obtain designed materials with suitable characteristics to host a great variety of molecules.

Acknowledgments

The authors would like thank to Universidad Autónoma Metropolitana and National Institute of Neurology an Neurosurgery for facilities; special thanks to P. Castillo for TEM studies also Project FONCICYT-CONACYT 96095 for financial support.

References

[1] R. Bawa, "Patents and nanomedicine," *Nanomedicine*, vol. 2, no. 3, pp. 351–374, 2007.

- [2] R. Bawa, S. R. Bawa, S. B. Maebius, T. Flynn, and C. Wei, "Protecting new ideas and inventions in nanomedicine with patents," *Nanomedicine*, vol. 1, no. 2, pp. 150–158, 2005.
- [3] A. Abdulwahed, "Gastrointestinal and cardiovascular risk of nonsteroidal anti-inflammatory drugs," *Oman Medical Journal*, vol. 26, no. 6, pp. 385–391, 2011.
- [4] L. Filaretova, T. Bagaeva, O. Morozova, and D. Zelena, "The healing of nsaid-induced gastric lesion may be followed by small intestinal and cardiovascular side effects," *Journal of Physiology and Pharmacology*, vol. 62, no. 6, pp. 619–625, 2011.
- [5] I. Pountos, T. Georgouli, G. Calori, and P. Giannoudis, "Do nonsteroidal anti-inflammatory drugs affect bone healing?" *The Scientific World Journal*, vol. 2012, Article ID 606404, 14 pages, 2012.
- [6] N. M. Gajraj, "The effect of cyclooxygenase-2 inhibitors on bone healing," *Regional Anesthesia and Pain Medicine*, vol. 28, no. 5, pp. 456–465, 2003.
- [7] L. E. Targownik, C. J. Metge, S. Leung, and D. G. Chateau, "The relative efficacies of gastroprotective strategies in chronic users of nonsteroidal anti-inflammatory drugs," *Gastroenterology*, vol. 134, no. 4, pp. 937–e1, 2008.
- [8] J. Varshosaz, V. Hajhashemi, and S. Soltanzadeh, "Lipid nanocapsule-based gels for enhancement of transdermal delivery of ketorolac tromethamine," *Journal Drug Delivery*, vol. 2011, Article ID 571272, 7 pages, 2011.
- [9] P. Santhosh, N. Senthil Kumar, M. Renukadevi, A. I. Gopalan, T. Vasudevan, and K. P. Lee, "Enhanced electrochemical detection of ketorolac tromethamine at polypyrrole modified glassy carbon electrode," *Analytical Sciences*, vol. 23, no. 4, pp. 475–478, 2007.
- [10] S. Hungund and R. Thakkar, "Effect of pretreatment with Ketorolac Tromethamine on operative pain during periodontal surgery: a case-control study," *Journal of Indian Society of Periodontology*, vol. 15, no. 1, pp. 55–58, 2011.
- [11] S. K. Paliwal, R. Chauhan, V. Sharma, D. K. Majumdar, and S. Paliwal, "Entrapment of ketorolac tromethamine in polymeric vehicle for controlled drug delivery," *Indian Journal of Pharmaceutical Sciences*, vol. 71, no. 6, pp. 687–691, 2009.
- [12] M. A. Radwan, B. T. AlQuadeib, N. M. Aloudah, and H. Y. Aboul Enein, "Pharmacokinetics of ketorolac loaded to polyethylcyanoacrylate nanoparticles using UPLC MS/MS for its determination in rats," *International Journal of Pharmaceutics*, vol. 397, no. 1-2, pp. 173–178, 2010.
- [13] V. R. Sinha and A. Trehan, "Formulation, characterization, and evaluation of ketorolac tromethamine-loaded biodegradable microspheres," *Drug Delivery*, vol. 12, no. 3, pp. 133–139, 2005.
- [14] A. P. Rokhade, S. A. Agnihotri, S. A. Patil, N. N. Mallikarjuna, P. V. Kulkarni, and T. M. Aminabhavi, "Semi-interpenetrating polymer network microspheres of gelatin and sodium carboxymethyl cellulose for controlled release of ketorolac tromethamine," *Carbohydrate Polymers*, vol. 65, no. 3, pp. 243–252, 2006.
- [15] L. Genc and E. Jalvand, "Preparation and in vitro evaluation of controlled release hydrophilic matrix tablets of ketorolac tromethamine using factorial design," *Drug Development and Industrial Pharmacy*, vol. 34, no. 8, pp. 903–910, 2008.
- [16] T. López, S. Recillas, P. Guevara, J. Sotelo, M. Alvarez, and J. A. Odriozola, "Pt/TiO₂ brain biocompatible nanoparticles: GBM treatment using the C6 model in Wistar rats," *Acta Biomaterialia*, vol. 4, no. 6, pp. 2037–2044, 2008.

- [17] K. Farrington and F. Regan, "Molecularly imprinted sol gel for ibuprofen: an analytical study of the factors influencing selectivity," *Talanta*, vol. 78, no. 3, pp. 653–659, 2009.
- [18] J. González, J. Pérez, F. Ruiz, and J. y Martínez, "Vidrios SiO₂ nanocompuestos preparados por sol-gel: revisión," *Superficies y Vacío*, vol. 11, pp. 1–16, 2000.
- [19] J. Livage, C. Sanchez, M. Henry, and S. Doeuff, "The chemistry of the sol-gel process," *Solid State Ionics*, vol. 32-33, no. 2, pp. 633–638, 1989.
- [20] J. Livage, "Sol-gel processes," *Current Opinion in Solid State and Materials Science*, vol. 2, no. 2, pp. 132–138, 1997.
- [21] A. Kalampounias, "IR and Raman spectroscopic studies of sol-gel derived alkaline-earth silicate glasses," *Bulletin of Materials Science*, vol. 34, no. 2, pp. 299–303, 2011.
- [22] C. M. Whang, C. S. Yeo, and Y. H. Kim, "Preparation and characterization of sol-gel derived SiO₂-TiO₂-PDMS composite films," *Bulletin of the Korean Chemical Society*, vol. 22, no. 12, pp. 1366–1370, 2001.
- [23] Y. T. Sohn and O. S. Hyun, "Crystal forms of ketorolac," *Archives of Pharmacal Research*, vol. 27, no. 3, pp. 357–360, 2004.
- [24] W. Lin and Zhong, *Characterization of Nanophase Materials, Transmission Electron Microscopy and Spectroscopy of Nanoparticles*, Qilwy-VCH Verlag GmbH, Berlin, Germany, 2000.
- [25] M. J. Uddin, D. Mondal, C. A. Morris, T. Lopez, U. Diebold, and R. D. Gonzalez, "An in vitro controlled release study of valproic acid encapsulated in a titania ceramic matrix," *Applied Surface Science*, vol. 257, no. 18, pp. 7920–7927, 2011.
- [26] H. Guo, H. Qian, S. Sun et al., "Hollow mesoporous silica nanoparticles for intracellular delivery of fluorescent dye," *Chemistry Central Journal*, vol. 5, no. 1, p. 1, 2011.
- [27] K. Ruckmani, M. S. Muneera, and R. Vijaya, "Eudragit matrices for sustained release of ketorolac tromethamine: formulation and kinetics of release," *Bollettino Chimico Farmaceutico*, vol. 139, no. 5, pp. 205–208, 2000.

Research Article

Factorial Study of Compressive Mechanical Properties and Primary *In Vitro* Osteoblast Response of PHBV/PLLA Scaffolds

Naznin Sultana^{1,2} and Tareef Hayat Khan³

¹Department of Mechanical Engineering, The University of Hong Kong, Pokfulam Road, Hong Kong

²Department of Clinical Sciences, Faculty of Biosciences and Medical Engineering, Universiti Teknologi Malaysia, Johor, 81310 Johor Bahru, Malaysia

³Department of Architecture, Faculty of Built Environment, Universiti Teknologi Malaysia, Johor, 81310 Johor Bahru, Malaysia

Correspondence should be addressed to Naznin Sultana, naznin@biomedical.utm.my

Received 11 September 2012; Accepted 30 October 2012

Academic Editor: Xiao-Miao Feng

Copyright © 2012 N. Sultana and T. H. Khan. This is an open access article distributed under the Creative Commons Attribution License, which permits unrestricted use, distribution, and reproduction in any medium, provided the original work is properly cited.

For bone tissue regeneration, composite scaffolds containing biodegradable polymers and nanosized osteoconductive bioceramics have been regarded as promising biomimetic systems. Polymer blends of poly(hydroxybutyrate-co-hydroxyvalerate) (PHBV) and poly(L-lactic acid) (PLLA) can be used as the polymer matrix to control the degradation rate. In order to render the scaffolds osteoconductive, nano-sized hydroxyapatite (nHA) particles can be incorporated into the polymer matrix. In the first part of this study, a factorial design approach to investigate the influence of materials on the initial compressive mechanical properties of the scaffolds was studied. In the second part, the protein adsorption behavior and the attachment and morphology of osteoblast-like cells (Saos-2) of the scaffolds *in vitro* were also studied. It was observed that nHA incorporated PHBV/PLLA composite scaffolds adsorbed more bovine serum albumin (BSA) protein than PHBV or PHBV/PLLA scaffolds. *In vitro* studies also revealed that the attachment of human osteoblastic cells (SaOS-2) was significantly higher in nHA incorporated PHBV/PLLA composite scaffolds. From the SEM micrographs of nHA incorporated PHBV/PLLA composite scaffolds seeded with SaOS-2 cells after a 7-day cell culture period, it was observed that the cells were well expanded and spread in all directions on the scaffolds.

1. Introduction

In scaffold-based tissue engineering (TE), scaffolds play several important roles. Scaffold material and scaffold fabrication techniques should be selected carefully as the scaffold properties are crucial to determine the success of a TE approach [1, 2]. One of the basic requirements for polymer-based scaffolds is that the scaffolds should have controllable porous architecture that can allow cell migration, attachment, and growth, leading to tissue regeneration. The degradation product(s) of scaffolds should be non-toxic and easily taken up or excreted via metabolic pathways. Scaffolds should have sufficient mechanical strength to maintain structural integrity during culture. Some of the commonly used biodegradable polymers that are used as scaffold materials include poly(glycolic acid) (PGA),

poly(L-lactic acid) (PLLA), and their copolymer poly(lactic acid-co-glycolic acid) (PLGA) [2]. Poly(hydroxybutyrate-co-hydroxyvalerate) (PHBV), which is a natural, biodegradable polymer, possesses good biocompatibility, also being used to make into TE scaffolds. The *in vivo* degradation product of PHBV is a normal constituent of human blood [2]. PHBV has been investigated for tissue engineering application [3–5]. Due to the slow degradation rate, PHBV can be blended with PLLA in order to control degradation rate and time [6, 7]. Hydroxyapatite (HA) being the mineral component of living bones has gained much recognition as a scaffolding material [8, 9]. Nanosized HA (nHA) and biodegradable polymer blends containing biocomposite scaffolds can offer a promising strategy for bone tissue regeneration.

The freeze-drying technique has been used for constructing TE scaffolds due to its usefulness to create highly porous

scaffolds and controlled pore sizes [10, 11] although there are many techniques available to fabricate tissue engineering scaffolds. If freeze-drying technique is used, a number of factors are concerned for the ultimate morphology and properties of the scaffolds. It is possible to achieve highly organized three-dimensional structures if the parameters are selected and employed properly. In the first part of the study, the factorial design was used to investigate the material parameters to fabricate TE scaffolds based on PHBV and PLLA polymers and nHA.

Protein adsorption on the substrate is of importance in evaluating a TE scaffold as cell adhesion and survival could be modulated by adsorption capacity on the substrate [12]. Within seconds of implantation, protein adsorption onto the foreign surface occurs when biomaterials are implanted into animals or humans. By rapid protein adsorption, it is meant that the arriving cells at the biomaterial surface interact with the adsorbed protein layer instead of the material itself. The response between implanted biomaterial and the body depends on the initial protein adsorption onto a biomaterial surface. Thus adsorption of protein plays a key role. The three primary plasma proteins are albumin, immunoglobulin, and fibrinogen. Among these three proteins, albumin is the predominant plasma protein which makes up 60–70% of plasma. It was reported that albumin could “passivate” the surface of biomaterial and reduced the acute inflammatory response to the biomaterial. It was reported that osteoblast adhesion was significantly greater on nanophase alumina, titania and HA which was due to enhanced adsorption of protein vitronectin by the bioceramics [12]. Protein adsorption of cerium oxide nanoparticles as a function of zeta potential was studied and it was reported that electrostatic interactions played an important role in protein adsorption of nanoparticles [13]. The adhesion of protein on low density polyethylene (LDPE) was studied and it was described that the surface wettability and contact time had significant effects on protein adhesion to the surface of biomaterials. In the second part of this study, the protein adsorption behavior by the scaffolds and the response of osteoblast attachment and morphology was also investigated for the composite scaffolds.

In the present study, a two-level fractional factorial design was formulated to determine the compressive properties of the scaffolds *in vitro* and then the scaffolds were used for protein (bovine serum albumin, BSA) adsorption study. The attachment and morphology of osteoblast-like cells (Saos-2) when cultured on the scaffolds were also studied.

2. Materials and Methods

2.1. Materials. PHBV (6% of 3-hydroxyvalerate) was purchased from Sigma-Aldrich and PLLA with an inherent viscosity 1.6 dL g^{-1} and 1.9 dL g^{-1} (Medisorb 100L 1A) was purchased from Lakeshore Biomaterials (Birmingham, AL). The nHA nanoparticles used for composite scaffolds were produced in-house through a nanoemulsion process [14]. All chemicals used in this investigation were analytical grade.

2.2. Methods

2.2.1. Factorial Design. To overcome the limitations of one-factor-at-a-time method, a factorial design study was performed to investigate the effects of material parameters to produce tissue engineering scaffolds. Five processing parameters as variables were tested in a two-level fractional factorial design [15] and compressive properties were determined from compressive stress-strain curves. The variables in the experimental design were (1) the polymer concentration, (2) water phase fraction, (3) blend composition of PLLA in PHBV, (4) the amount of HA as filler, and (5) molecular weight of PLLA.

2.2.2. Scaffold Fabrication. For scaffold fabrication, polymer was weighed accurately and poured into a centrifuge tube. Then an accurately measured amount of chloroform was added to the tube to make a solution with a desired polymer concentration. After obtaining the homogeneous polymer solution, the water phase (aqueous acetic acid solution or ultra pure water) was added to make an emulsion. The emulsion was homogenized by using a homogenizer (Ultra-Turrax, T-25; IKA-WERKE). Polymer or HA/polymer composite scaffolds were made via freeze-drying technique [5, 16].

In order to solidify the emulsion, the beaker containing the emulsion was rapidly transferred into a deep freezer at a preset temperature for overnight. The frozen emulsion was then placed into a freeze-drying vessel (LABCONCO-Freeze dry system, USA). To remove the solvent and the water phase completely, the samples were freeze-dried for at least 46 hrs. The polymer and composite scaffolds were subsequently obtained. The scaffolds were stored in a vacuum desiccator at room temperature for storage.

2.2.3. Characterization and In Vitro Mechanical Properties of the Scaffolds. The porous structures of PHBV scaffolds were studied through scanning electron microscopy (SEM; Stereoscan 440, Cambridge, UK). The pore diameters were calculated using SEM micrographs. Using an Instron mechanical tester (Instron 5848, USA) with a 100 N load cell and at a crosshead speed of 0.5 mm/min , the compressive mechanical properties of PHBV and PHBV-based composite scaffolds were obtained for dry cylindrical samples with height of 5 mm and diameter of 10 mm at room temperature. The compressive yield strength and compressive modulus was calculated from the initial linear region of stress-strain curves.

2.2.4. Protein Adsorption Study. Experiments of protein adsorption on scaffolds (100/0 PHBV/PLLA, 50/50 PHBV/PLLA, and 10% HA in 50/50 PHBV/PLLA) were performed by incubating scaffold samples at 37°C in PBS containing bovine serum albumin (BSA) for predetermined periods of time. The samples were pretreated by ethanol and washed by PBS before incubation. A commercial protein assay kit, Micro BCA (Thermo Scientific, Pierce, Rockford, IL, USA) using BSA standards, was used to quantify the

concentration of protein in BSA/PBS solutions containing scaffold samples and the control (without scaffold samples), respectively, under the same incubation conditions. The amount of adsorbed proteins was determined by subtracting the amount of protein which was left in the BSA/PBS solution from the amount of protein in the control.

2.2.5. Cell Culture and Cell Seeding. Human osteoblast cells (Saos-2) were cultured with Dulbecco's modified Eagle medium (DMEM, Gibco, UK). The medium was supplemented with L-glutamine, 1% streptomycin, 0.04% fungi zone, and 10% fetal calf serum (FCS) at 37°C in a 5% (v/v) CO₂ incubator. The cells were detached using 0.25% (w/v) trypsin-ethylenediaminetetraacetic acid (EDTA) (Invitrogen, USA) when the cells reached about 80% confluence and subcultured for subsequent use. Scaffold samples were cut to the correct height (1.5 mm) and diameter (10 mm) and were prewetted in ethanol for 24 h and then washed with PBS. Then they were sterilized by ⁶⁰Co γ -irradiation. 2.2×10^5 cells/well in the wells of a 24-well plate were then seeded separately onto scaffold samples as well as onto a tissue culture polystyrene (TCPS) as control. Then the culture wells were filled with 1 mL of culture medium. The cell-scaffold constructs were maintained until 1, 7, or 14 days postseeding.

2.2.6. Cell Attachment and Morphology. The cells were cultured for 3 h and 24 h in order to examine the cell attachment to the scaffolds and TCPS; Triplicate samples were used for each time. The culture medium was removed after each time point and then the wells were gently washed with PBS to remove unattached cells. The adherent cells were enzymatically released from the specimens with the aid of 0.25% trypsin-EDTA. In order to count the cells, a haemocytometer (Tiefe Depth Profounder, Marienfeld, Germany) was used.

The viability and the morphology of cells around the scaffold specimen on the bottom of the cell culture plate was observed through an optical microscope (Leica MZFLIII, Germany) equipped with a digital camera. For scanning electron microscopy (SEM), cells were grown and prepared for SEM by fixing with 2.5% glutaraldehyde in cacodylate buffer and dehydrated with ethanol. Then the samples were dried in a critical point dryer using liquid carbon dioxide as the transition fluid. The samples were sliced, sputter coated, and analyzed with a SEM (Hitachi S3400N).

2.2.7. Statistical Analysis. All quantitative data of this study were obtained from triplicate samples and were presented as mean \pm standard deviation (SD). To test the significance, an unpaired Student's *t* test (two tail) was applied. A value of $P < 0.05$ was considered to be statistically significant.

3. Results and Discussion

3.1. Factorial Design Study. Tables 1 and 2 show the low and high levels of the variables which are represented by "+" and "-" and the combinations of the variables in total of

TABLE 1: Low levels (-) and high levels (+) of variables in the fractional factorial design.

Factors	Levels	
	-	+
(A) Polymer concentration (%)	7.5	10
(B) Water phase fraction	0.5	0.66
(C) Composition of PLLA in PHBV	50/50	75/25
(D) Amount of HA (%)	5	10
(E) Molecular weight of PLLA (dL g ⁻¹)	1.6	1.9

eight runs. The results of factorial design on compressive properties are given in Table 3. For the composite scaffolds, the effects of the five variables in the fractional factorial design on the compressive strength and modulus with their standard errors are given in Table 4. Figure 1 is the typical compressive stress-strain curves of a scaffold specimens cut from one scaffolds. The compressive stress-strain curve had three distinct regions: linear elasticity, long plateau, and densification region. The compressive modulus and compressive yield strengths were calculated from initial linear region. It can be demonstrated that the positive number indicates that the particular variable has an effect to increase the modulus as it goes from its low level to high level and a negative number indicates that the variables causes the modulus to decrease as the variable goes from its low level to its high level. As it is important to have some methods for interpreting the effects whether they are certainly real and whether they might be explained readily by chance variation, a rough rule is that effects greater than 2 or 3 times their standard error cannot be explained by chance alone [15].

In Table 4, the main effects which are not due to noise are given in italic form. It can be seen from Table 4 that the polymer concentration, amount of HA, and the molecular weight of PLLA had the effects to increase the compressive modulus and yield strength as they go from low levels to high levels. On the other hand, the ratio of water phase and blend composition have the effects to decrease the compressive modulus and yield strength when they go from low to high levels.

Yaszemski et al. investigated the effects of several composite material formulations and conducted a factorial study to calculate initial mechanical properties *in vitro* and studied the association with histological characteristics of the resulting material *in vivo* [17]. It was also reported that the synthesis of polymer allowed alterations of the composition as well as of the physical properties to effect resulting composites. It was also studied and reported that the polymer molecular weight, presence of a leachable salt, and amount of cross linking monomer had strong effects on the final strength and modulus of the composite, which were on the order of 5 MPA, an appropriate magnitude for a temporary trabecular bone substitute [18]. In this study, the effects of five processing parameters were studied for the determination of the effects of these processing parameters on the compressive properties. It was possible

TABLE 2: Eight-run experimental design for studying the effects of the five factors.

Run number	Polymer concentration (A)	Water phase composition (B)	Blend composition PLLA/PHBV (C)	Amount of HA (D)	PLLA molecular weight (E)
1	+	-	-	-	-
2	+	-	+	+	-
3	+	-	-	+	+
4	-	+	+	+	-
5	-	+	-	-	-
6	+	+	+	-	+
7	-	+	-	+	+
8	-	-	+	-	+

TABLE 3: Compressive yield strength and compressive modulus of scaffolds.

Run number	Compressive yield strength* (MPa)	Modulus* (MPa)
1	0.25 ± 0.07	4.0 ± 1.2
2	0.50 ± 0.04	11.0 ± 3.4
3	0.80 ± 0.06	12.0 ± 4.1
4	0.20 ± 0.01	1.0 ± 0.3
5	0.11 ± 0.01	1.2 ± 0.4
6	0.32 ± 0.08	0.8 ± 0.2
7	0.23 ± 0.04	10.0 ± 3.1
8	0.34 ± 0.05	2.0 ± 0.8

*mean ± standard deviation.

to produce scaffolds by altering the combinations of these parameters. Polymer concentration and amount of HA had the maximum effects on the scaffold compressive properties. It was observed that the scaffolds produced from these processing parameters which had highest effects on the compressive properties would facilitate bone formation *in vitro* [5].

3.2. Scaffold Properties. For the second part of the study, based on the parameters and main effects as given in Table 1 and Table 4, three types of scaffolds fabricated from 10% (w/v) polymer concentration, 0.5 water phase fraction, 100/0 PHBV/PLLA, 50/50 PLLA/PHBV and 10% HA incorporated 50/50 PHBV/PLLA scaffolds were chosen for protein adsorption and *in vitro* cell culture study. SEM micrographs of these three types of scaffolds are given in Figures 2(a), 2(b), and 2(c). It was observed that the scaffolds exhibited a large pore size distribution (from several μm to 300 μm) and had interconnected pores. It was also observed that the HA nano particles were homogeneously distributed in the 10% HA incorporated 50/50 PHBV/PLLA composite scaffolds described elsewhere [5].

3.3. Protein Adsorption. Figure 3(a) shows the physical appearance of the scaffolds. All the scaffolds were three-dimensional in structure and physically manageable. UV-visible spectroscopy measurements were carried out for

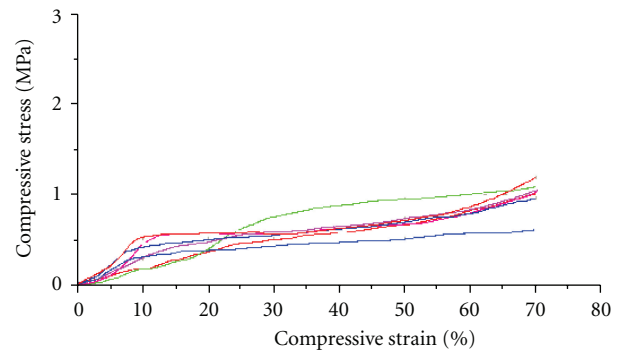


FIGURE 1: Typical compressive curves of the scaffold specimens cut from one scaffolds fabricated from combination of run 3 of Table 3.

known concentrations of BSA at the absorbance of 562 nm. Noncoated polymer and composite scaffolds of different composition were incubated for 3 hrs, 22 hrs and 42 hrs in BSA/PBS solution in order to assess protein adsorption behavior. After 22 hrs, protein adsorption of all the scaffolds reached equilibrium as there was no significant change observed from 22 hrs to 42 hrs (Figure 3(b)). Figure 4 shows the effect of polymer blend composition and incorporated nHA on the protein adsorption capacity of composite scaffolds. The amount of adsorbed protein was calculated from the standard curve. After 22 hr, of immersion in BSA/PBS solution, 50/50 PHBV/PLLA scaffold adsorbed more BSA proteins than 100/0 PHBV/PLLA scaffold and 10% nHA incorporated 50/50 PHBV/PLLA composite scaffolds adsorbed more BSA proteins than plain PHBV scaffold.

Protein adsorption is of importance to evaluate a scaffold for the tissue engineering application. It was observed from this part of the study that composite scaffolds containing nanosized HA could adsorb more protein than pure PHBV or PHBV/PLLA blend scaffolds. Incorporation of HA can alter the pore surface morphology of the scaffolds and may made them more suitable for increased protein adsorption. As HA has better affinity towards protein adsorption, particles exposed on the pore walls in the composite scaffolds had increased capacity of protein adsorption.

Andrade et al. and Sun et al. studied the principles of protein adsorption extensively and summarized that the

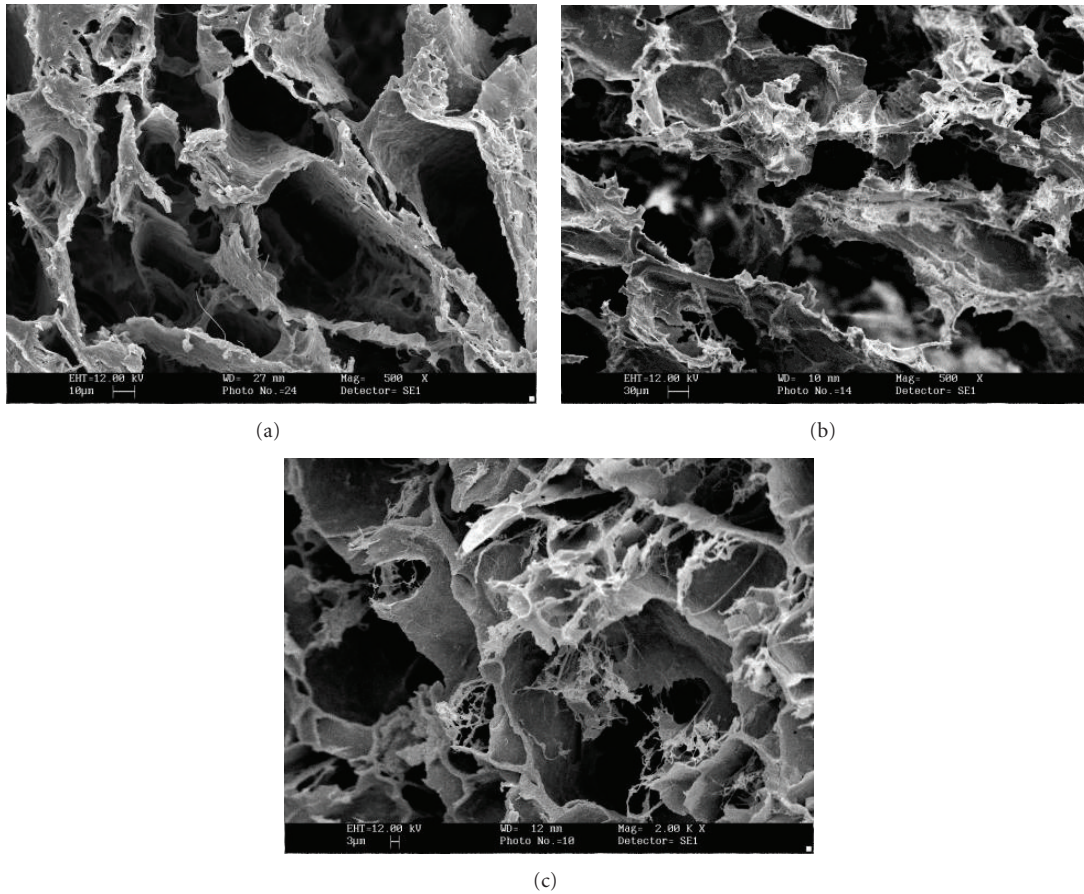


FIGURE 2: Microstructures examined by SEM of three types of scaffolds: (a) 100/0 PHBV scaffold, (b) 50/50 PHBV/PLLA scaffold, and (c) 10% HA in 50/50 PHBV/PLLA scaffold.

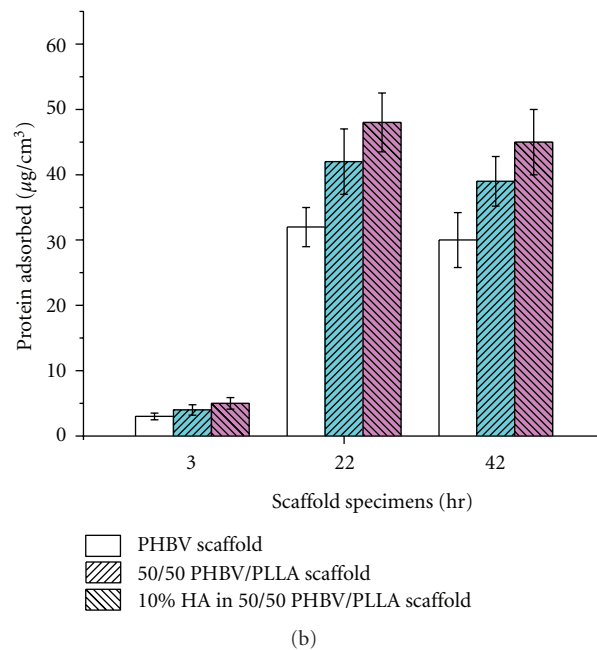


FIGURE 3: (a) General appearance of the scaffolds and (b) protein adsorption of different scaffolds at 3 hrs, 22 hrs and 42 hrs (data are expressed as mean ± SD; n = 3).

TABLE 4: Calculated main effects of the variables on compressive strength and modulus.

Main effects	Effect on compressive yield strength (MPa)*	Effect on modulus (MPa)*
(A) Polymer concentration	+0.25 ± 0.03	+3.4 ± 1.12
(B) Water phase composition	-0.26 ± 0.03	-4.0 ± 1.12
(C) Ratio of PHBV/PLLA	-0.01 ± 0.03	-3.1 ± 1.12
(D) The amount of HA	+0.18 ± 0.03	+6.5 ± 1.12
(E) Molecular weight of PLLA	+0.16 ± 0.03	+1.9 ± 1.12

*mean ± standard error.

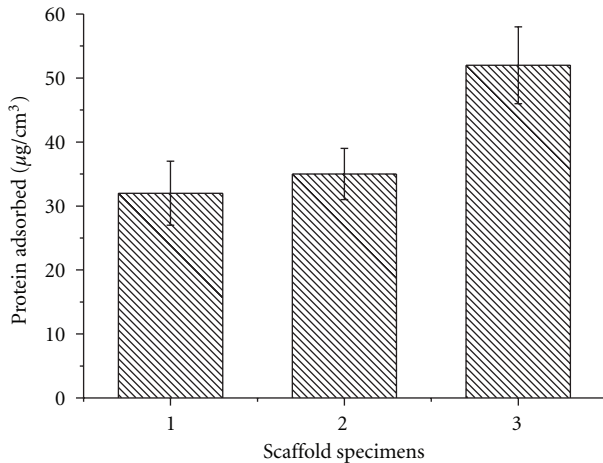


FIGURE 4: Protein adsorption of different scaffolds: (1) PHBV scaffolds, (2) 50/50 blend scaffolds, and (3) 10% HA in 50/50 blend scaffolds; (Data are expressed as mean ± SD; $n = 3$).

arrival of protein at the interface is driven solely by diffusion process which is dependent on bulk concentration and diffusion coefficient [18, 19]. It was also demonstrated that the particular surface chemistry of the protein also controls the adsorption. When protein adsorption takes place on neutral hydrophilic surfaces, it will be relatively weak; on the other hand, adsorption of proteins on hydrophobic surfaces tends to be very strong and irreversible. When adsorption takes place on charged surfaces, it tends to be a strong function of the charge character of the protein, the pH of the medium, and ionic strength. In this study, protein adsorption onto the scaffolds was reported. In order to study the mechanisms whether the protein is adsorbed on the scaffolds strongly or moderately, protein release study is needed.

3.4. Cell Morphology and Attachment. Both optical microscopy (Figure 5) and SEM (Figure 6) were used to examine the state and morphology of Saos-2 cells. Figure 5 shows the state and morphology of Saos-2 cells after biocompatibility test for 3 days. It was observed that the cell population and cell morphology of all specimens of PHBV scaffolds, 50/50 PHBV/PLLA scaffolds, and 10% HA in 50/50 PHBV/PLLA scaffolds were comparable to the control. This can indicate that the cell viability remained high after being in contact with all three types of scaffolds.

Using SEM analysis, the morphology of Saos-2 cells on the surface of the scaffolds specimens was also studied. Cells were appeared with clear substrate attachments and cellular processes. After culturing for 1 day, flat cells were observed by SEM to be well attached on all three types of scaffolds. At day 7 of Saos-2 cultures on all types of scaffolds, SEM analysis verified that the Saos-2 cells were well proliferated. The cells were more elongated as well as very well attached and spread on the surface of the scaffolds. The difference in morphology observed among the cells grown on three types of scaffolds was not obvious. The cells were found anchored to the surface by discrete filopodia on the composite scaffolds (Figure 6).

In this study, all three types of scaffolds were evaluated for cell attachment (Figure 7). It was observed that after 24 hours, the number of cells attached to HA incorporated composite scaffolds was significantly different ($P < 0.05$) than that of 100/0 PHBV/PLLA scaffolds or 50/50 PHBV/PLLA blend scaffolds. On the other hand, the number of Saos-2 cells attached on the PHBV/PLLA scaffold was apparently higher than PHBV scaffolds. The difference was not statistically significant.

In our previous studies [5–7], we reported the fabrication, *in vitro* degradation and biological evaluation of PHBV-based scaffolds using emulsion freezing/freeze-drying process. In the present paper, a factorial design approach was used to systematically investigate the influence of different material parameters on the compressive mechanical properties of the PHBV-based scaffolds. Besides the other requirements, the scaffolds should possess appropriate mechanical properties. In order to control the compressive stress and compressive modulus of the polymer and composite scaffolds, careful analysis was possible using factorial design approach. The protein adsorption and osteoblast (Saos-2) cell response were also studied in order to evaluate the scaffolds for bone tissue engineering application. Successful control of compressive properties is important for constructing composite scaffolds for bone tissue engineering applications.

4. Conclusions

A factorial design study was performed to assess the main effects of different material parameters on the compressive properties of the scaffolds. Polymer concentration and the amount of HA had the strongest effect to increase the compressive modulus and yield strength. 100/0

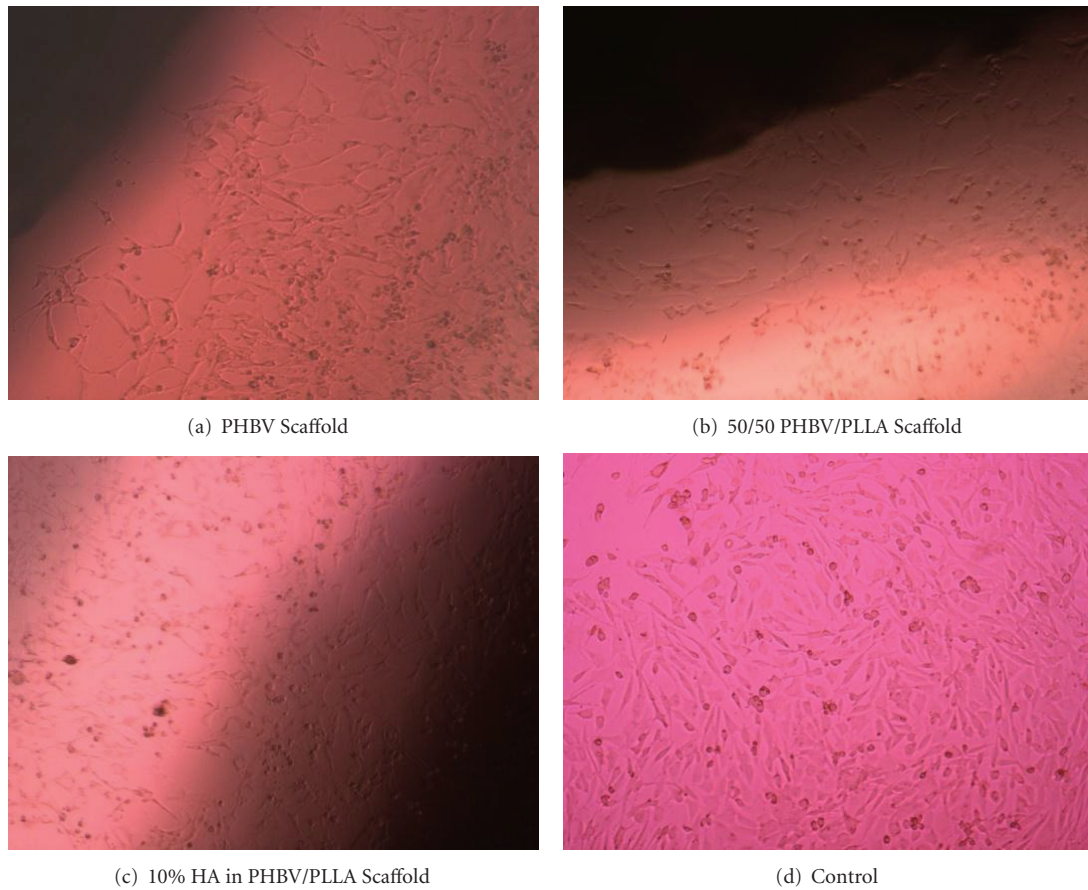


FIGURE 5: Optical microscopic image of state and morphology of Saos-2 cells in contact with scaffold specimens, (the dark area in (a), (b), (c) is the test specimen (d) control). (Magnification $\times 10$).

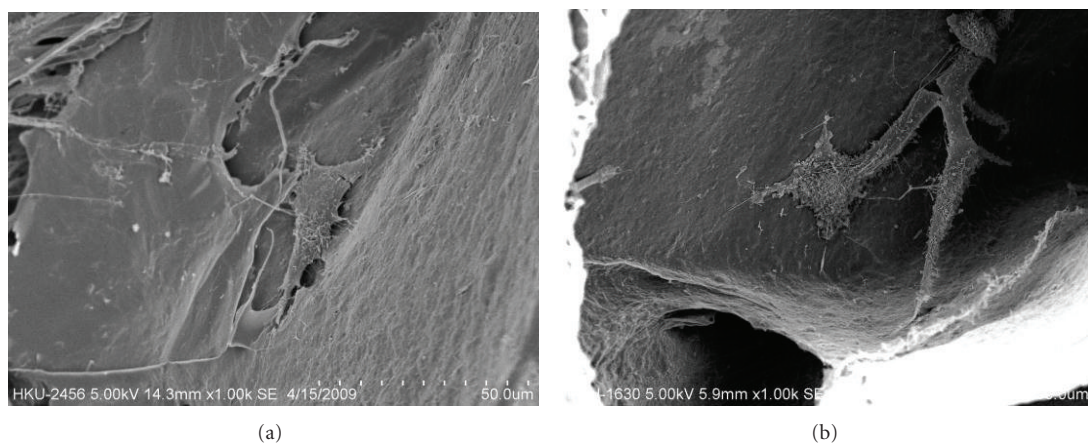


FIGURE 6: SEM micrographs of 10% HA in 50/50 PHBV/PLLA composite scaffold after 7-day culture with Saos-2 cells (a, b).

PHBV/PLLA scaffolds, 50/50 PHBV/PLLA scaffolds, and 10% HA incorporated 50/50 composite scaffolds showed satisfactory adsorption of BSA protein. Adsorption of protein of all the scaffolds reached equilibrium after 22 hrs. The HA incorporated composite scaffolds exhibited more affinity towards protein adsorption than pure other two types of scaffolds. The attachment of Saos-2 cells was

also significantly higher in 10% HA incorporated 50/50 composite scaffolds.

Conflict of Interests

The authors declare that they do not have any conflict of interests.

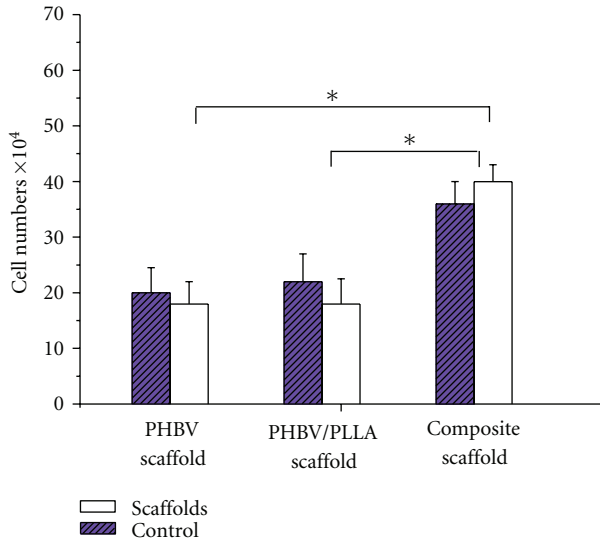


FIGURE 7: The attachment of Saos-2 cells on PHBV and PHBV-based composite scaffolds (data are expressed as mean \pm SD; 2 = 3. * $P < 0.05$).

Acknowledgment

N. Sultana acknowledges The University of Hong Kong (HKU), GRF Grant (HKU 7182/05E) from the Research Grants Council of Hong Kong. Assistance provided by technical staff in the Department of Mechanical Engineering, Faculty of Engineering and Department of Orthopedics and Traumatology, Li Ka Shing Faculty of Medicine, HKU, is acknowledged. N. Sultana and T. H. Khan also acknowledge the financial support provided by UTM research Grants GUP Tier 1 (Vote: 03H13), GUP Tier 2 (vote: 06J34), FRGS (vote: 4F126), and ERGS (Vote: 4L063), Ministry of Higher Education (MOHE), and RMC for financial support.

References

- [1] P. X. Ma, "Scaffolds for tissue fabrication," *Materials Today*, vol. 7, no. 5, pp. 30–40, 2004.
- [2] P. A. Holmes, *Developments in Crystalline Polymers*, Edited by D. C. Bassett, Elsevier Applied Science, London, UK, 1982.
- [3] B. Duan, M. Wang, W. Y. Zhou, W. L. Cheung, Z. Y. Li, and W. W. Lu, "Three-dimensional nanocomposite scaffolds fabricated via selective laser sintering for bone tissue engineering," *Acta Biomaterialia*, vol. 6, no. 12, pp. 4495–4505, 2010.
- [4] H. W. Tong, M. Wang, Z. Y. Li, and W. W. Lu, "Electrospinning, characterization and in vitro biological evaluation of nanocomposite fibers containing carbonated hydroxyapatite nanoparticles," *Biomedical Materials*, vol. 5, no. 5, Article ID 054111, 2010.
- [5] N. Sultana and M. Wang, "PHBV/PLLA-based composite scaffolds fabricated using an emulsion freezing/freeze-drying technique for bone tissue engineering: surface modification and in vitro biological evaluation," *Biofabrication*, vol. 4, Article ID 015003, 2012.
- [6] N. Sultana and T. H. Khan, "In Vitro degradation of PHBV scaffolds and nHA/PHBV composite scaffolds containing hydroxyapatite nanoparticles for bone tissue engineering," *Journal of Nanomaterials*, vol. 2012, Article ID 190950, 12 pages, 2012.
- [7] N. Sultana and M. Wang, "PHBV/PLLA-based composite scaffolds containing nano-sized hydroxyapatite particles for bone tissue engineering," *Journal of Experimental Nanoscience*, vol. 3, no. 2, pp. 121–132, 2008.
- [8] P. X. Ma, R. Zhang, G. Xiao, and R. Franceschi, "Engineering new bone tissue in vitro on highly porous poly(alpha-hydroxyl acids)/hydroxyapatite composite scaffolds," *Journal of Biomedical Materials Research*, vol. 54, pp. 284–293, 2001.
- [9] H. Wang, Y. Li, Y. Zuo, J. Li, S. Ma, and L. Cheng, "Biocompatibility and osteogenesis of biomimetic nano-hydroxyapatite/polyamide composite scaffolds for bone tissue engineering," *Biomaterials*, vol. 28, no. 22, pp. 3338–3348, 2007.
- [10] K. Whang and K. E. Healy, "Processing of polymer scaffolds: freeze-drying," in *Methods of Tissue Engineering*, A. Atala and R. P. Lanza, Eds., p. 1285, Academic Press, San Diego, Calif, USA, 2002.
- [11] N. Sultana and M. Wang, "Fabrication of tissue engineering scaffolds using the emulsion freezing/freeze-drying technique and characteristics of the scaffolds," in *Integrated Biomaterials in Tissue Engineering*, pp. 63–89, John Wiley & Sons, 2012.
- [12] T. J. Webster, C. Ergun, R. H. Doremus, R. W. Siegel, and R. Bizios, "Specific proteins mediate enhanced osteoblast adhesion on nanophase ceramics," *Journal of Biomedical Materials Research*, vol. 51, pp. 475–483, 2000.
- [13] S. Patil, A. Sandberg, E. Heckert, W. Self, and S. Seal, "Protein adsorption and cellular uptake of cerium oxide nanoparticles as a function of zeta potential," *Biomaterials*, vol. 28, no. 31, pp. 4600–4607, 2007.
- [14] W. Y. Zhou, M. Wang, W. L. Cheung, B. C. Guo, and D. M. Jia, "Synthesis of carbonated hydroxyapatite nanospheres through nanoemulsion," *Journal of Materials Science: Materials in Medicine*, vol. 19, no. 1, pp. 103–110, 2008.
- [15] G. E. P. Box, J. S. Hunter, and W. G. Hunter, *Statistics for Experimenters: Design, Innovation, and Discovery*, Wiley-Interscience, Hoboken, NJ, USA, 2nd ed edition, 2005.
- [16] N. Sultana and M. Wang, "Fabrication of HA/PHBV composite scaffolds through the emulsion freezing/freeze-drying process and characterisation of the scaffolds," *Journal of Materials Science: Materials in Medicine*, vol. 19, no. 7, pp. 2555–2561, 2008.
- [17] M. J. Yaszemski, R. G. Payne, W. C. Hayes, R. S. Langer, T. B. Aufdemorte, and A. G. Mikos, "The ingrowth of new bone tissue and initial mechanical properties of a degrading polymeric composite scaffold," *Tissue Engineering*, vol. 1, pp. 41–52, 1995.
- [18] J. D. Andrade, V. Hlady, and A. P. Wei, "Adsorption of complex proteins at interfaces," *Pure and Applied Chemistry*, vol. 64, pp. 1777–1781, 1992.
- [19] T. Sun, M. Wang, and W. C. Lee, "Surface characteristics, properties and in vitro biological assessment of a NiTi shape memory alloy after high temperature heat treatment or surface H₂O₂-oxidation: a comparative study," *Materials Chemistry and Physics*, vol. 130, no. 1-2, pp. 45–58, 2011.

Research Article

Hydroxyapatite Nanopowder Synthesis with a Programmed Resorption Rate

**Dariusz Smoleń,¹ Tadeusz Chudoba,¹ Stanisław Gierlotka,¹
Aleksandra Kedzierska,¹ Witold Łojkowski,¹ Kamil Sobczak,²
Wojciech Świążkowski,³ and Krzysztof Jan Kurzydłowski³**

¹*Institute of high Pressure Physics, Polish Academy of Science, Sokolowska 29/37, 01-142 Warsaw, Poland*

²*Institute of Physics, Polish Academy of Science, Al. Lotnikow 32/46, 02-668 Warsaw, Poland*

³*Faculty of Materials Science and Engineering, Warsaw University of Technology, Woloska 141, 02-507 Warsaw, Poland*

Correspondence should be addressed to Dariusz Smoleń, smolendarek@gmail.com

Received 11 September 2012; Revised 18 October 2012; Accepted 1 November 2012

Academic Editor: Yan-Yan Song

Copyright © 2012 Dariusz Smoleń et al. This is an open access article distributed under the Creative Commons Attribution License, which permits unrestricted use, distribution, and reproduction in any medium, provided the original work is properly cited.

A microwave, solvothermal synthesis of hydroxyapatite (HAp) nanopowder with a programmed material resorption rate was developed. The aqueous reaction solution was heated by a microwave radiation field with high energy density. The measurements included powder X-ray diffraction (PXRD) and the density, specific surface area (SSA), and chemical composition as specified by the inductively coupled plasma optical emission spectrometry technique (ICP-OES). The morphology and structure were investigated using scanning electron microscopy (SEM) and transmission electron microscopy (TEM). A degradation test in accordance with norm ISO 10993-4 was conducted. The developed method enables control of the average grain size and chemical composition of the obtained HAp nanoparticles by regulating the microwave radiation time. As a consequence, it allows programming of the material degradation rate and makes possible an adjustment of the material activity in a human body to meet individual resorption rate needs. The authors synthesized a pure, fully crystalline hexagonal hydroxyapatite nanopowder with a specific surface area from 60 to almost 240 m²/g, a Ca/P molar ratio in the range of 1.57–1.67, and an average grain size from 6 nm to over 30 nm. A 28-day degradation test indicated that the material solubility ranged from 4 to 20 mg/dm³.

1. Introduction

The number of cases of bone defects requiring replacement has increased rapidly in recent years [1, 2]. Nevertheless, there is no solution presently available that overcomes the disadvantages and disabilities of current medical practices. Techniques are needed to repair large bone defects and to return patients to their previous quality of life. A primary difficulty is the lack of a proper material which enables the creation of bone scaffolds with the appropriate mechanical strength and a controllable resorption rate. Currently, autografts are the clinical gold standard for bone replacement therapy. Autografts provide the primary factors for effective bone regeneration, but they also impose a significant cost and risk [3–5].

One potential solution marketed as filler for small bone gaps and defects is a bioactive ceramic made of micro- and sub-microhydroxyapatite. Due to their strong similarity to the mineral phase of native bone, called apatite, bioactive ceramics display appropriate levels of osteoconductivity and biocompatibility [6, 7]. Additionally, the interaction of osteogenic cells with this material leads to good bone bonding and bone regeneration [8]. Although micro- or sub-microhydroxyapatite powder is suitable for recovering small bone gaps, in more complicated cases it has several drawbacks like the lack of possibility to control the material resorption rate [9, 10]. These disadvantages may be reduced or eliminated by replacing the micropowder by a hydroxyapatite nanopowder. The latter has grains much smaller than 100 nm, possibly giving it unexpected

properties that are necessary to achieve a proper bioactivity and biodegradability levels. These nanoparticles have a significantly greater surface-to-volume ratio than powders with larger grains; thus, they have increased surface energy [11, 12]. Consequently, the surface energy-related features such as the solubility may be controlled. According to the Ostwald-Freundlich equation [13], the material solubility increases with increased specific surface area. A decrease in the HAp particle size to a few nanometers should significantly increase the material solubility [13]. The ability to regulate the particle size thus enables the control of the material degradation rate. Additionally, as the literature shows [14], osteoblast adhesion is strongly driven by the material surface area and topography. A decrease in the particle size increases the osteoblast adhesion as it is directly related [14] to the greater surface area.

A second important feature which influences the HAp bioactivity is its stoichiometry. Bone mineral has a Ca/P molar ratio near 1.50, which is close to the tricalcium phosphate (TCP) stoichiometry, but structurally and chemically it is similar to the stoichiometric HAp with a Ca/P molar ratio equal to 1.67 [15]. The ion exchange or degradation rate is strongly dependent on the bioactive ceramic stoichiometry. With calcium deficiency increase, the number of crystalline structure defects caused by calcium ions vacancies increases which is reducing material stability and in consequence increasing its solubility [15, 16].

The literature presents various methods for hydroxyapatite nanoparticle synthesis; these include processes conducted by mills [17, 18], hydrothermal syntheses conducted in a typical vessel with conventional heating [19, 20], sol-gel methods [21, 22], and even synthesis by emulsion [23, 24]. In most cases, the synthesized powder is stoichiometric hydroxyapatite, and in many cases it includes additional phases and substances such as byproducts or unreacted substrates. Usually the powder's degradation rate is too low to adjust to bone scaffolding needs and it is not possible to program its solubility in advance, which is necessary for bone implant development to overcome the previously described barriers. Microwave heating is a potential solution, as it may result in a product that fulfills the previously described requirements. It has been used as a source of energy [25–27], but to our best knowledge, never in a closed system with an energy density equal to or above 5 W/mL. Microwave radiation is able to evenly and rapidly heat an entire volume of a vessel almost without a temperature gradient in the heated materials [28, 29]. Additionally, it enables the necessary control of the reaction parameters, so there is the possibility of obtaining a fully crystalline, nonequilibrium structure with a programmed grain-size distribution [30, 31].

The purpose of this work was to develop a microwave solvothermal synthesis method (MSS) based on high energy density microwave radiation [32] which results in pure, nonstoichiometric hydroxyapatite nanoparticles with a programmed particle size, that is, able to regulate the degradation rate of bone scaffolds. The novelty of the presented method lies in its extremely short synthesis time, ranging from 90 seconds to 10 minutes, which is made possible by the

implementation of a microwave reactor with a high energy density reaching 5 W/mL. This paper presents the chemical, physical, and biological properties of the obtained material, including its chemical composition, structure, morphology, and solubility.

2. Experimental Methods

2.1. Material Preparation. The hydroxyapatite nanocrystals were obtained by the following method, described in detail in [33]. The starting materials used for the HAp synthesis were calcium hydroxide ($\text{Ca}(\text{OH})_2$, CHEMPUR, pure) and phosphoric acid (H_3PO_4 , 85% solution, CHEMPUR, pure for analysis); the reactants were used in a molar ratio Ca/P of 1.67. To form a reaction solution, phosphoric acid was added dropwise to the calcium solution at a rate of 0.01 mL every 3 seconds, and the solution was intensively stirred at room temperature. After 30 minutes of additional stirring, the reaction solution was transferred into a capped Teflon vessel and heated using microwave radiation. The microwave reactor was produced by ERTEC (Wroclaw, Poland) and was operated at 2.45 GHz and at a power density adjusted to approximately 5 W/mL. The time, temperature, pressure, and microwave power were computer-controlled. The synthesis conditions encompassed pressures ranging from 1 to 32 MPa and times ranging from 1.5 min to 10 min. After the synthesis, the obtained powder was washed by anhydrous ethanol and dried in an air flow at a temperature of 30°C for 16 h. Herein, this resulting material is referred to as “GoHAP” with the addition of the reaction time (e.g., GoHAP 1.5 min).

The hydroxyapatite nanopowder NanoXIM201 (FLUIDINOVA, ENGENHARIA DE FLUIDOS, SA TECMAIA-Parque de Ciência e Tecnologia da Maia Rua Eng° Frederico Ulrich, 2650 4470-605 Moreira da Maia, Portugal) was used as a reference material in the degradation test and in the PXRD analysis. To the authors' knowledge, this commercially available hydroxyapatite powder had the lowest available particle size on the market. Its characteristics were a density of 2.93 g/dm³, an SSA of 120 m²/g, an average particle diameter calculated from SSA of 17 nm, and a Ca/P molar ratio declared by the producer and confirmed by the authors of 1.66. Figure 1 presents SEM micrograph of NanoXIM201 nanopowder.

Additionally, an XRD analysis using a plate from a pig's shank bone was used as a reference for natural apatite.

2.2. Material Characterization. The density measurements were performed using a helium pycnometer (Micromeritics AccuPyc, model 1330) using an in-house procedure [34]. The specific surface area (SSA) of the powders was measured by the Brunauer-Emmett-Teller (BET) method (Micromeritics AccuPyc, model Gemini 2360). The average diameter of the particles was calculated based on the specific surface area and density, assuming that all of the particles were spherical and identical [34].

The phase composition of the reaction products was analyzed by powder X-ray diffraction (Panalytical X'Pert

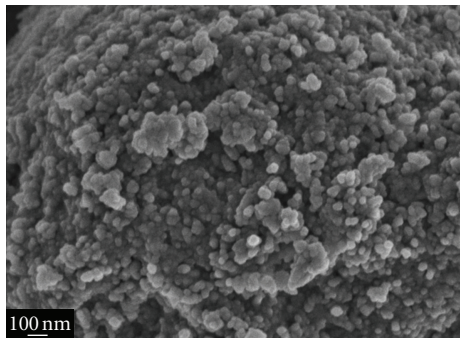


FIGURE 1: SEM micrograph of NanoXIM201 nanopowder produced by the Fluidinova Company.

PRO diffractometer, Cu K α 1 radiation). The patterns were collected at room temperature in the 2 theta range 10–150° and with a step of 0.03°. The pattern analysis was performed by whole pattern fitting (the Rietveld method) using the DDM software suite [35]. The particle size was determined by the Scherrer equation.

The morphology of the nanopowder samples was examined with SEM (ZEISS LEO 1530) and TEM (JEOL JEM2000EX). The TEM investigations, high-resolution TEM (HRTEM), and selected area electron diffraction (SAED) were conducted at 200 kV. The specimens for the TEM observations were prepared by dropping the methanol particle dispersion, created by an ultrasonic technique, on a carbon film supported on a 300 mesh copper grid. Additionally, TEM studies were used to determine the nanoparticle size distribution. The grain size histograms were obtained by considering a region of a sample having about 250 nanocrystals and approximating the shape of each nanocrystal by a sphere. The obtained histograms were fitted to either normal or log-normal distributions (Chi-square test and Person's coefficient).

The chemical composition of the powders was determined by inductively coupled plasma optical emission spectrometry (ICP-OES), with induction in argon plasma (Jobin-Yvon, model 138 Ultrace).

The determination of material solubility was performed according to norm ISO 10993-14: biological evaluation of medical devices—identification and quantification of degradation products from ceramics. The material was tested in the form of a 6 mm disk (each disk was around 35 mg and was created from the nanopowder using a laboratory hydraulic press under 5 MPa pressure) and was placed in 200 mL of buffer solution (TRIS-HCl buffer with pH 7.4 ± 0.1). A simulation solution test, lasting 28 days, was conducted without buffer solution exchange during the entire test. During the degradation test the samples were incubated at 37.0°C. Along with the degradation of the samples, the calcium ion concentration value was measured three times per week with an ion selective electrode (Schott ProLab 2000 GLP equipped with ion electrode type CA60). Additionally, the material solubility was determined by the gravimetric method.

3. Results and Discussion

With the shortest reaction of 1.5 min of microwave radiation, the obtained GoHAP had a density equal to 2.91 g/cm³, which is 4% lesser than the value given in the literature for hydroxyapatite, 3.05 g/cm³ [36]. It was observed that with nanoparticles, there was a reduction in the material density probably caused by the high contribution of surface layers, which are less densely packed than the bulk [37]. The material's specific surface area was 236 ± 5 m²/g, and the average particle diameter calculated based on SSA was 9 nm. Longer microwave radiation slowly increased the material density and significantly decreased the specific surface area (Figure 2); details are presented in Table 1. For the 2.5-minute reaction, the specific surface area of GoHAP was reduced by over 60 m²/g to 174 m²/g, and the density increased to 2.94 g/cm³ comparing to the 1.5 min reaction. The average particle size calculated based on the specific surface area increased to 12 nm. With 5 minutes of microwave radiation, the SSA decreased to under 100 m²/g. The density increased by 0.02 g/cm³ to 2.96 g/cm³; the average particle size exceeded 20 nm. Within extension of the reaction time over 5 minutes, there was a decrease in the specific surface area to 81 m²/g for the 7.5-minute reaction and 63 m²/g for the 10-minute reaction. Consequently, the density became 3.00 g/cm³ and the particle size became 25 nm for the 7.5-minute reaction. For the 10-minute reaction, the resulting particles had an average size of 32 nm and a density of 3.03 g/cm³, which was almost equal to the literature values for hydroxyapatite [36].

The ICP-OES analysis indicated that for 1.5 min reaction, the Ca/P molar ratio was equal to 1.57, which is close to the molar ratios of the natural bone calcium and phosphorus elements [36]. Longer microwave heating increased the Ca/P molar ratio to values close to stoichiometric HAP (Figure 3); with 2.5 minutes of reaction the Ca/P molar ratio changed to 1.65 which is a value frequently indicated in papers presenting HAP synthesis [17–24]. After 5.0 minutes of reaction, the ratio was equal to 1.66, and further radiation led to fully stoichiometric hydroxyapatite. In all cases the obtained powder included 0.20–0.22 wt% magnesium ions.

The XRD analysis was conducted on GoHAP powders obtained from 1.5-, 2.5-, 5.0-, and 10.0-minute reactions and using a plate from a pig's shank bone as a reference for natural apatite (Figure 4). The results confirmed that the GoHAP powders were a pure well-crystalline hexagonal hydroxyapatite with nanosized particles. No indication of the presence of other crystalline phases or any amorphous component was found. The lattice parameters for the GoHAP powders are presented in Table 2, and the pig bone results were $a = 9.42(5)$ Å and $c = 6.87(7)$ Å. Other crystal structure parameters could not be derived with satisfying precision due to the considerable anisotropy size and the very small absolute crystal size. However, it was apparent that the crystals obtained in the reaction with 10 minutes of microwave radiation were approximately 10 times larger than the crystals of GoHAP obtained from the 1.5 minute reaction.

The morphology investigation was conducted with SEM and TEM techniques. Figure 5 shows SEM micrographs

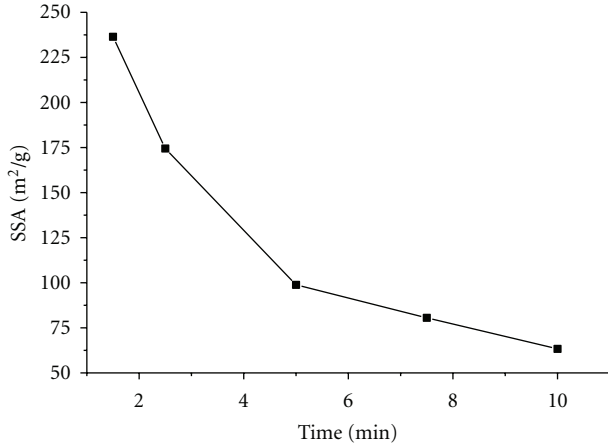


FIGURE 2: Effect of the microwave radiation time on the specific surface area.

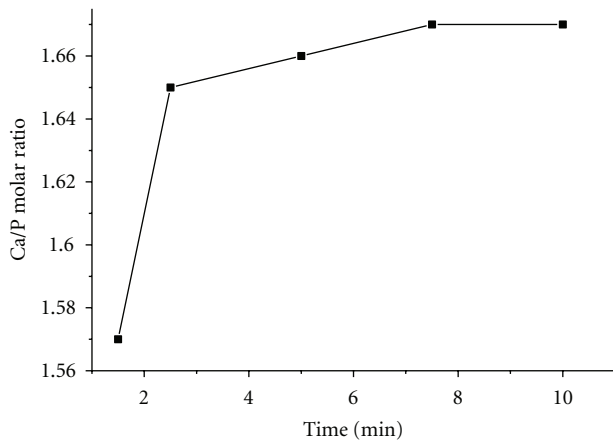


FIGURE 3: Effect of the microwave radiation time on the Ca/P molar ratio.

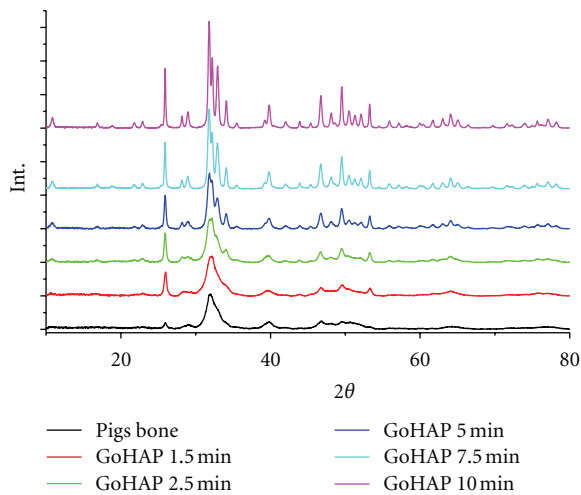


FIGURE 4: XRD patterns of HAp particles in pig bone and GoHAP powders synthesized with microwave radiation times of 1.5, 2.5, 5.0, and 10.0 minutes.

TABLE 1: Effect of the microwave radiation time on the material specific surface area, the density, the grain size calculated on the basis of SSA measurements, and the Ca/P ratio established by the ICP-OES measurements.

Radiation time (min)	SSA (m ² /g)	Density (g/cm ³)	Grain size (nm)	Ca/P
1.5	236	2.91	9	1.57
2.5	174	2.94	12	1.65
5.0	99	2.96	21	1.66
7.5	81	3.00	25	1.67
10.0	63	3.03	32	1.67

TABLE 2: Effect of the microwave radiation time on the lattice parameters determined by the XRD analysis.

Radiation time (min)	Lattice parameter <i>a</i> (±0.001 Å)	Lattice parameter <i>c</i> (±0.0007 Å)
1.5	9.433	6.8745
2.5	9.439	6.8775
5.0	9.429	6.8772
7.5	9.425	6.8767
10.0	9.423	6.8777

of GoHAP nanoparticles for reaction times of 1.5 min, 2.5 min, 5.0 min, and 10.0 min. Figure 5(a) presents the strong homogeneity of GoHAP obtained from the 1.5 min reaction and confirms that the average particle size of the synthesized hydroxyapatite was less than 10 nm. The powder obtained with 1 minute longer reaction (2.5 minutes) had a larger average particle size as observed on a SEM micrograph (Figure 5(b)). Instead of being homogeneous as with the powder from the shortest reaction time, this powder appeared in the form of agglomerates with diverse sizes. Further microwave heating (5.0- and 7.5-minute reactions) increased the size of both the single particles and their agglomerates. The nanopowder presented in Figure 5(c) was obtained from the 5-minute reaction. Compared to GoHAP synthesized in the shortest reaction, its morphology was highly diverse, and several times the larger particles were grouped in agglomerates with sub-micro- and microsizes. Finally, the reaction with 10 minutes of microwave radiation led to a significant increase in the single particle size and decreased the powder agglomeration degree (Figure 5(d)). The GoHAP powder after the longest reaction time was in form of large, slightly agglomerated particles with an average grain size close to 50 nm.

A TEM examination showed that for all microwave radiation times, the obtained hydroxyapatite had the space group P.P63/m of a hexagonal crystal structure with the parameters $a = 9.424(4) \text{ \AA}$ and $c = 6.879(4) \text{ \AA}$ [38]. An increase in the reaction time did not have any visible impact on the phase composition and lattice parameters. In all cases the result was pure hexagonal hydroxyapatite without phase impurities. Figure 6 shows the SAED with identified planes for hydroxyapatite synthesized during the 1.5-minute reaction; in the remaining cases SAED was identical. No

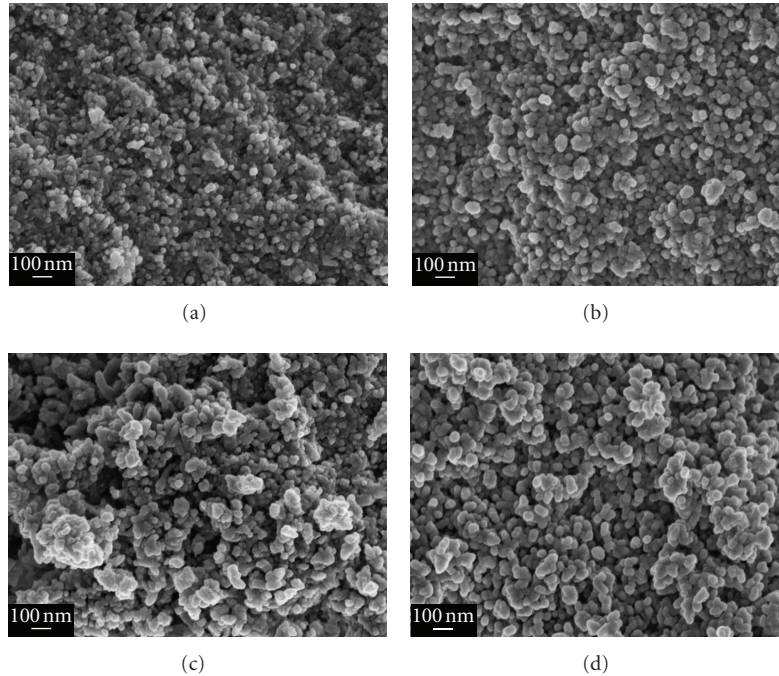


FIGURE 5: SEM micrographs of GoHAP synthesized in (a) 1.5-minute reaction, (b) 2.5-minute reaction, (c) 5.0-minute reaction, and (d) 10.0-minute reaction.

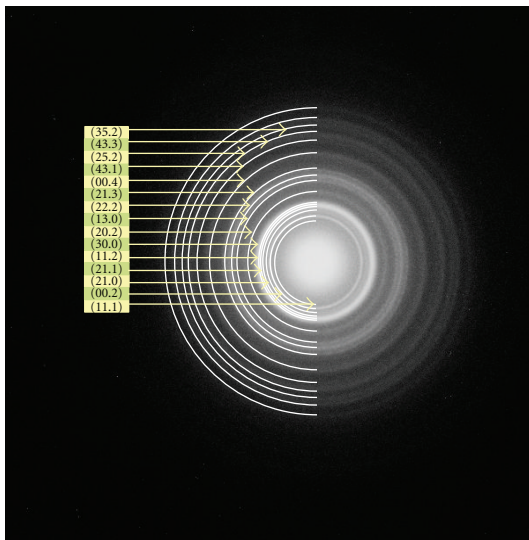


FIGURE 6: SAED with the identified planes.

other phases have been found in tested samples. The average grain size for GoHAP synthesized during the 1.5-minute reaction was 5.6 nm (Figure 7). After increasing the reaction time to 2.5 minutes, the average grain size barely changed; it was 5.8 nm but studies indicated that the particles were in the form of large, stable agglomerates. Further microwave heating caused an increase in the particle size and a decrease in the sample homogeneity. Figure 8 shows an image taken in the dark field of particles obtained from the 7.5-minute reaction, with a morphology ranging from spherical to

almost needle-like shapes. The average grain size after the 7.5-minute reaction was 26.2 nm. Reactions longer than 7.5 minutes increased the grain size to over 30 nm.

A degradation test was conducted for GoHAP obtained during reactions with microwave radiation times of 1.5, 2.5, 5.0, and 10.0 minutes. Commercially available HAP nanopowder, NanoXIM, was used as a reference material. The initial pH of the test solution was 7.47, the conductivity was 6.82 mS/cm, and the calcium ion concentration was $0.479 \mu\text{mol}/\text{dm}^3$. The results of the calcium ion concentration changes are shown in Figure 9. These results showed that in each day the GoHAP obtained from the shortest reaction (1.5 minutes) had the highest rate of degradation. Along with an increase in the microwave radiation time for the GoHAP synthesis there was decrease in the material solubility, until finally, in the case of GoHAP obtained from the longest (10 minutes) reaction, the achieved solubility value was close to the NanoXIM results. After 21 days of tests, the calcium ion concentration in the sample with NanoXIM remained nearly constant and achieved a value of $40.37 \mu\text{mol}/\text{dm}^3$ by the end of test, which can be recalculated based on weight solubility to $4.0 \text{ mg}/\text{dm}^3$. After three weeks of tests, the GoHAP obtained in 1.5 min reaction had twice as much solubility as NanoXIM, and, furthermore, in the fourth week there was an acceleration of solubility which led to a concentration of $199.6 \mu\text{mol}/\text{dm}^3$ calcium ions by the end of the test, equal to $20.0 \text{ mg}/\text{dm}^3$. The GoHAP obtained with microwave radiation times longer than 1.5 minutes achieved solubility values in the range between the NanoXIM and GoHAP 1.5 min solubility, decreasing as a function of microwave radiation time. In the case of GoHAP obtained with the 2.5-minute reaction, the final

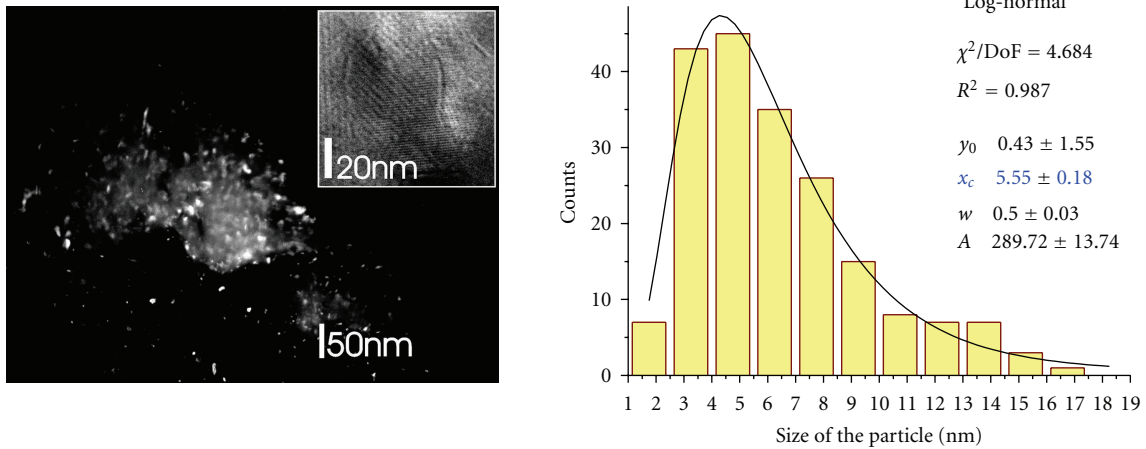


FIGURE 7: The dark field TEM image of GoHAP synthesized with a 1.5-minute reaction, and the histogram of the particle size distribution.

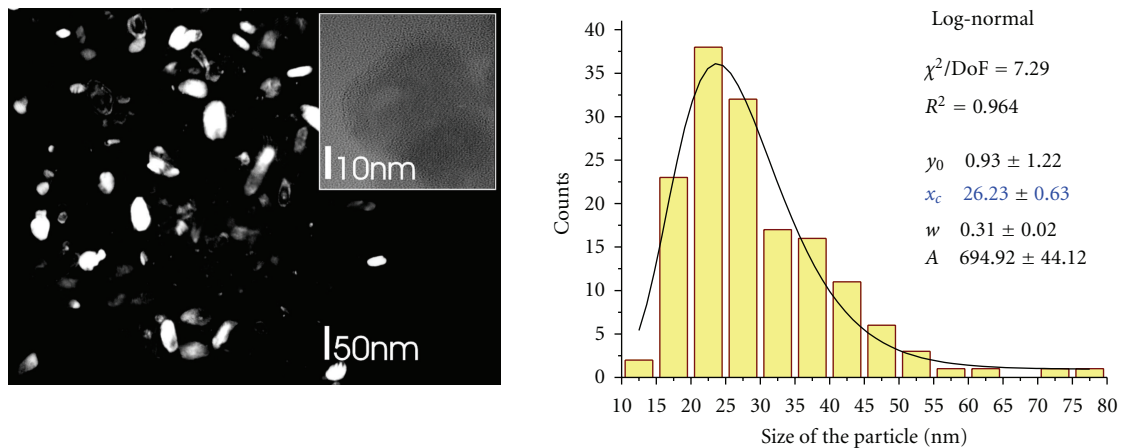


FIGURE 8: The dark field TEM image of GoHAP synthesized with a 7.5-minute reaction, and the histogram of the particle size distribution.

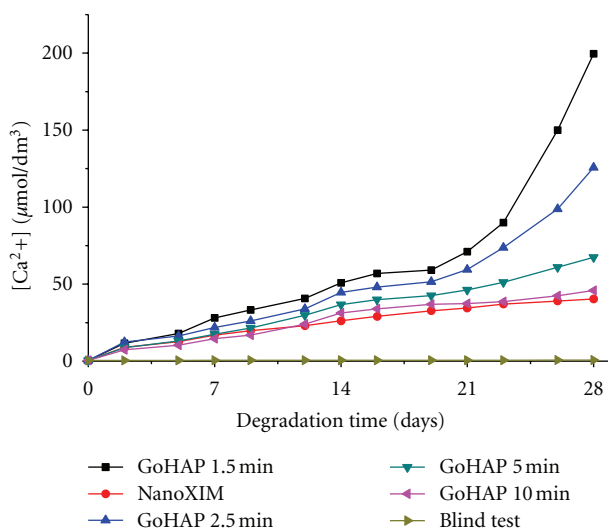


FIGURE 9: Calcium ion concentration changes for GoHAP synthesized with microwave radiation times of 1.5, 2.5, 5.0, and 10.0 minutes, and for the commercial nanopowder, NanoXIM used as a reference material.

calcium ion concentration was $125.7 \mu\text{mol}/\text{dm}^3$ which is equal to $12.6 \text{ mg}/\text{dm}^3$ solubility. The GoHAP obtained with the 5-minute reaction achieved $67.4 \mu\text{mol}/\text{dm}^3$ calcium ion concentration equal to $6.8 \text{ mg}/\text{dm}^3$ solubility, and that from the longest (10 minutes) microwave reaction had $4.6 \text{ mg}/\text{dm}^3$ solubility ($45.8 \mu\text{mol}/\text{dm}^3$ calcium ion concentration).

The degradation test was additionally followed by determining the weight loss after 28 days of tests. During the test, NanoXIM lost 4% of its original weight, resulting in $7.0 \text{ mg}/\text{dm}^3$ of solubility, and GoHAP obtained with 1.5-minute reaction time lost over 22% of its initial weight, equal to $38.5 \text{ mg}/\text{dm}^3$. GoHAP from the 2.5-minute reaction had a solubility of $25.6 \text{ mg}/\text{dm}^3$, from the 5-minute reaction had solubility of $14.1 \text{ mg}/\text{dm}^3$, and from the 10 min reaction had solubility of $8.7 \text{ mg}/\text{dm}^3$, as determined from weight loss measurements. The solubility measured by the gravimetric method was in all cases approximately twice as large as the solubility measured by changes in the calcium ion concentration, probably due to nanopowder dispersion. The samples of GoHAP synthesized in 1.5 min reaction were deeply cracked on whole sample surface, but the test disk still was keeping its original shape, when the NanoXIM sample

was cracked only in few places and was very weak. In case of the rest GoHAP samples, the density and depth of cracks were decreasing with powder reaction time increase—the GoHAP obtained in 10-minute reaction presented similar cracking to the NanoXIM disk, but it was much more stable during the mechanical operations, like disk transport, and so forth.

Such a high solubility rate should ensure a short degradation time of future scaffold. In degradation time longer than 28 days of conducted ISO test, GoHAP samples should keep or even accelerate their degradation rate, but in case of the real bone implants, the scaffolds degradation rate for time perspective longer than 28 days will depend on many other factors like new tissue formation process, and so forth, so that for long-time periods it should be checked by in vivo tests.

The degradation test showed that the developed method has the potential to adjust the material solubility according to the individual case needs in range from 4 to 20 mg/dm³, according to the ISO 10993-14 norm. The synthesis of this material with a programmable degradation rate was possible due to the implementation of a unique microwave heating technology (MSS) with very high energy density, which enables precise control of the material grain size growth. Compared to conventional heating, microwaves transmit energy directly to the entire volume almost without causing temperature gradients in the reaction vessel. The microwave radiation time may be regulated with 1 s precision, which enables precise grain size growth control.

The rapid microwave heating process leads to overheating of the reaction solution. From the overheated solution, a fine dispersion of nano-HAP precipitates starts to crystallise. Most likely, for short crystallisation times, kinetic processes dominate its growth, and nonstoichiometric crystallites grow with an nonequilibrium structure. Our experimental data show that this is the case for extremely short reaction times of 1.5 minutes. With increase of microwave radiation time the precipitates structure approaches the equilibrium one, and a fully stoichiometric structure is achieved for radiation times longer than 5 minutes (Figure 2). In consequence, precise microwave radiation time regulation allows to control hydroxyapatite stoichiometry and grain size growth. Furthermore the solution is rapidly cooled, so no secondary grain growth takes place [29, 39]. As it was described in the introduction section a material solubility depend on material specific surface area—the material solubility increases with material grain size decrease [13] and its nonstoichiometry [15, 16]. The decrease of Ca/P molar ratio was increasing calcium ion concentration in tested solution due to increase of crystalline defects in the hydroxyapatite structure. The higher calcium deficiency is, the more defected crystalline structure will be, which is decreasing material stability and in consequence increases its solubility.

Precise grain size growth control which determines material specific surface area, together with material stoichiometry control both available via microwave radiation time regulation made the programming of hydroxyapatite solubility possible. The microwave solvothermal synthesis (MSS) with the high energy density allowed obtaining GoHAP powder with unique features which is a promising

material for resorbable ceramic bone implants fabrication [40].

4. Conclusions

A fully crystalline hydroxyapatite nanopowder with programmed solubility rate was successfully synthesized by a novel MSS method using high-density microwave radiation as a heating mechanism. The material degradation rate was regulated by the amount of applied microwave radiation, which determined the particle size and stoichiometry of the obtained hydroxyapatite nanopowder and consequently enabled the material solubility to be programmed. The obtained nanopowder has unique properties. It is a pure crystalline, hexagonal hydroxyapatite nanopowder with a specific surface area ranging from 60 to almost 240 m²/g and a Ca/P molar ratio in the range of 1.57–1.67; these values are fully regulated by the applied microwave radiation time. The average particle size estimated by the TEM investigation was regulated between 6 nm to over 30 nm. As the degradation study demonstrated, the developed method was able to control the material solubility in conditions simulating the human body in the range from 4 mg/dm³—which is close to NanoXIM, a commercial HAp nanopowder—to 20 mg/dm³. The presented material has the potential to significantly improve the properties of ceramic bone scaffolds by allowing the implant degradation rate to be adjusted to individual situations.

Acknowledgments

This work was financed by the European Regional Development Fund within the Innovative Economy Operational Programme in the frame of the BIO-IMPLANT project “Bioimplants for the treatment of bone tissue lesions in oncological patients” (POIG.01.01.02-00-022/09) and by the SONOSCA ERANET-MATERA project as well as by the Institute of High Pressure Physics, PAS. The research subject was carried out with the use of equipment funded by the project CePT financed by the European Regional development Fund within the Operational Programme “Innovative Economy” for 2007–2013. The authors would like also to thank J. Mizeracki and A. Presz from the Institute of High Pressure Physics PAS, P. Dłużewski from the Institute of Physics PAS, and A. Karaś from the Institute of Electronic Materials Technology.

References

- [1] J. R. Porter, T. T. Ruckh, and K. C. Papat, “Bone tissue engineering: a review in bone biomimetics and drug delivery strategies,” *Biotechnology Progress*, vol. 25, no. 6, pp. 1539–1560, 2009.
- [2] European Technology Platform Nanomedicine, Roadmap Report, 2009.
- [3] C. F. Lord, M. C. Gebhardt, W. W. Tomford, and H. J. Mankin, “Infection in bone allografts. Incidence, nature, and treatment,” *Journal of Bone and Joint Surgery*, vol. 70, no. 3, pp. 369–376, 1988.

- [4] B. H. Berrey, C. F. Lord, M. C. Gebhardt, and H. J. Mankin, "Fractures of allografts. Frequency, treatment, and end-results," *Journal of Bone and Joint Surgery*, vol. 72, no. 6, pp. 825–833, 1990.
- [5] M. Aebi, "Introduction to update on osteochondral allograft surgery," in *Bone Transplantation*, M. Aebi and B. Regazzoni, Eds., Springer, Berlin, Germany, 1987.
- [6] S. H. Li, J. R. De Wijn, P. Layrolle, and K. De Groot, "Synthesis of macroporous hydroxyapatite scaffolds for bone tissue engineering," *Journal of Biomedical Materials Research*, vol. 61, no. 1, pp. 109–120, 2002.
- [7] B. Flautre, M. Descamps, C. Delecourt, M. C. Blary, and P. Hardouin, "Porous HA ceramic for bone replacement: role of the pores and interconnections—experimental study in the rabbit," *Journal of Materials Science: Materials in Medicine*, vol. 12, no. 8, pp. 679–682, 2001.
- [8] S. S. Kim, M. Sun Park, O. Jeon, C. Yong Choi, and B. S. Kim, "Poly(lactide-co-glycolide)/hydroxyapatite composite scaffolds for bone tissue engineering," *Biomaterials*, vol. 27, no. 8, pp. 1399–1409, 2006.
- [9] F. Barrère, C. A. van Blitterswijk, and K. de Groot, "Bone regeneration: molecular and cellular interactions with calcium phosphate ceramics," *International Journal of Nanomedicine*, vol. 1, no. 3, pp. 317–332, 2006.
- [10] W. Suchanek and M. Yoshimura, "Processing and properties of hydroxyapatite-based biomaterials for use as hard tissue replacement implants," *Journal of Materials Research*, vol. 13, no. 1, pp. 94–117, 1998.
- [11] R. Dingreville, J. Qu, and Mohammed Cherkaoui, "Surface free energy and its effect on the elastic behavior of nano-sized particles, wires and films," *Journal of the Mechanics and Physics of Solids*, vol. 53, no. 8, pp. 1827–1854, 2005.
- [12] F. D. Fischer, T. Waitz, D. Vollath, and N. K. Simha, "On the role of surface energy and surface stress in phase-transforming nanoparticles," *Progress in Materials Science*, vol. 53, no. 3, pp. 481–527, 2008.
- [13] G. Kaptay, "On the size and shape dependence of the solubility of nano-particles in solution," *International Journal of Pharmaceutics*, vol. 430, pp. 253–2257, 2012.
- [14] T. J. Webster, R. W. Siegel, and R. Bizios, "Osteoblast adhesion on nanophase ceramics," *Biomaterials*, vol. 20, no. 13, pp. 1221–1227, 1999.
- [15] M. P. Ginebra, E. Fernández, F. C. M. Driessens, and J. A. Planell, "Modeling of the hydrolysis of α -tricalcium phosphate," *Journal of the American Ceramic Society*, vol. 82, no. 10, pp. 2808–2812, 1999.
- [16] J. L. Meyer and B. O. Fowler, "Lattice defects in nonstoichiometric calcium hydroxylapatites. A chemical approach," *Inorganic Chemistry*, vol. 21, no. 8, pp. 3029–3035, 1982.
- [17] W. L. Suchanek, P. Shuk, K. Byrappa, R. E. Riman, K. S. TenHuisen, and V. F. Janas, "Mechanochemical-hydrothermal synthesis of carbonated apatite powders at room temperature," *Biomaterials*, vol. 23, no. 3, pp. 699–710, 2002.
- [18] D. Choi and P. N. Kumta, "An alternative chemical route for the synthesis and thermal stability of chemically enriched hydroxyapatite," *Journal of the American Ceramic Society*, vol. 89, no. 2, pp. 444–449, 2006.
- [19] S. J. Yan, Z. H. Zhou, F. Zhang, S. P. Yang, L. Z. Yang, and X. B. Yu, "Effect of anionic PAMAM with amido groups starburst dendrimers on the crystallization of $\text{Ca}_{10}(\text{PO}_4)_6(\text{OH})_2$ by hydrothermal method," *Materials Chemistry and Physics*, vol. 99, no. 1, pp. 164–169, 2006.
- [20] A. Banerjee, A. Bandyopadhyay, and S. Bose, "Hydroxyapatite nanopowders: synthesis, densification and cell-materials interaction," *Materials Science and Engineering C*, vol. 27, no. 4, pp. 729–735, 2007.
- [21] T. A. Kuriakosea, S. N. Kalkuraa, M. Palamichanyc et al., "Synthesis of stoichiometric nano crystalline hydroxyapatite by ethanol based sol-gel technique at low temperature," *Journal of Crystal Growth*, vol. 263, pp. 517–523, 2004.
- [22] D. M. Liu, T. Troczynski, and W. J. Tseng, "Water-based sol-gel synthesis of hydroxyapatite: process development," *Biomaterials*, vol. 22, no. 13, pp. 1721–1730, 2001.
- [23] K. Sonoda, T. Furuzono, D. Walsh, K. Sato, and J. Tanaka, "Influence of emulsion on crystal growth of hydroxyapatite," *Solid State Ionics*, vol. 151, no. 1–4, pp. 321–327, 2002.
- [24] B. H. Chen, K. I. Chen, M. L. Ho, H. N. Chen, W. C. Chen, and C. K. Wang, "Synthesis of calcium phosphates and porous hydroxyapatite beads prepared by emulsion method," *Materials Chemistry and Physics*, vol. 113, no. 1, pp. 365–371, 2009.
- [25] S. J. Kalita and S. Verma, "Nanocrystalline hydroxyapatite bioceramic using microwave radiation: synthesis and characterization," *Materials Science and Engineering C*, vol. 30, no. 2, pp. 295–303, 2010.
- [26] D. Veljović, I. Zalite, E. Palcevskis, I. Smiciklas, R. Petrović, and D. Janačković, "Microwave sintering of fine grained HAP and HAP/TCP bioceramics," *Ceramics International*, vol. 36, no. 2, pp. 595–603, 2010.
- [27] S. Vijayan and H. Varma, "Microwave sintering of nanosized hydroxyapatite powder compacts," *Materials Letters*, vol. 56, no. 5, pp. 827–831, 2002.
- [28] D. E. Clark and W. H. Sutton, "Microwave processing of materials," *Annual Review of Materials Research*, vol. 26, pp. 299–331, 1996.
- [29] C. Leonelli and W. Lojkowski, "Main development directions in the application of microwave irradiation to the synthesis of nanopowders," *Chimica Oggi*, vol. 25, no. 3, pp. 34–38, 2007.
- [30] Y. B. Kholam, A. S. Deshpande, A. J. Patil, H. S. Potdar, S. B. Deshpande, and S. K. Date, "Microwave-hydrothermal synthesis of equi-axed and submicron-sized BaTiO_3 powders," *Materials Chemistry and Physics*, vol. 71, no. 3, pp. 304–308, 2001.
- [31] H. Yang, C. Huang, X. Li, R. Shi, and K. Zhang, "Luminescent and photocatalytic properties of cadmium sulfide nanoparticles synthesized via microwave irradiation," *Materials Chemistry and Physics*, vol. 90, no. 1, pp. 155–158, 2005.
- [32] A. Opalinska, C. Leonelli, W. Lojkowski et al., "Effect of pressure on synthesis of Pr-doped Zirconia powders produced by microwave-driven hydrothermal reaction," *Journal of Nanomaterials*, vol. 2006, Article ID 98769, 8 pages, 2006.
- [33] Patent application P-369906, The method of nanoplates obtaining from synthetic hydroxyapatite and method of nanopowder with nanoplates obtaining from synthetic hydroxyapatite.
- [34] T. Wejrzanowski, R. Pielaszek, A. Opalińska, H. Matysiak, W. Łojkowski, and K. J. Kurzydłowski, "Quantitative methods for nanopowders characterization," *Applied Surface Science*, vol. 253, no. 1, pp. 204–208, 2006.
- [35] L. A. Solovyov, "Full-profile refinement by derivative difference minimization," *Journal of Applied Crystallography*, vol. 37, no. 5, pp. 743–749, 2004.
- [36] P. W. Brown and B. Constantz, *Hydroxyapatite and Related Materials*, CRC Press, 1994.

- [37] J. Chang and E. Johnson, "Surface and bulk melting of small metal clusters," *Philosophical Magazine*, vol. 85, no. 30, pp. 3617–3627, 2005.
- [38] K. Sudarsanan and R. A. Young, "Significant precisions in crystal structural details. Holly springs hydroxyapatite," *Acta Crystallographica Section B*, vol. 25, pp. 1534–1543, 1969.
- [39] L. Perreux and A. Loupy, "A tentative rationalization of microwave effects in organic synthesis according to the reaction medium, and mechanistic considerations," *Tetrahedron*, vol. 57, no. 45, pp. 9199–9223, 2001.
- [40] Patent application P-399701, The method of bone implants fabrication and the bone implant.

Research Article

Understanding the Biocompatibility of Sintered Calcium Phosphate with Ratio of $[Ca]/[P] = 1.50$

Feng-Lin Yen,¹ Wei-Jen Shih,² Min-Hsiung Hon,³ Hui-Ting Chen,¹ I-Ming Hung,⁴
Homg-Huey Ko,¹ and Moo-Chin Wang¹

¹Department of Fragrance and Cosmetic Science, Kaohsiung Medical University, 100 Shih-Chuan 1st Road, Kaohsiung 80782, Taiwan

²Medical Devices and Opto-Electronics Equipment Department, Metal Industries Research and Development Center, 1001 Kaonan Highway, Kaohsiung 81160, Taiwan

³Department of Materials Science and Engineering, National Cheng Kung University, 1 Ta-Hsueh Road, Tainan 70101, Taiwan

⁴Department of Chemical Engineering and Materials Science, Yuan Ze University, 135 Yuan-Tung Road, Chungli, Taoyuan 320, Taiwan

Correspondence should be addressed to Moo-Chin Wang, mcwang@kmu.edu.tw

Received 3 September 2012; Revised 13 October 2012; Accepted 15 October 2012

Academic Editor: Yan-Yan Song

Copyright © 2012 Feng-Lin Yen et al. This is an open access article distributed under the Creative Commons Attribution License, which permits unrestricted use, distribution, and reproduction in any medium, provided the original work is properly cited.

Biocompatibility of sintered calcium phosphate pellets with $[Ca]/[P] = 1.50$ was determined in this study. Calcium pyrophosphate (CPP) phase formed on the sintered pellets immersed in a normal saline solution for 14 d at 37°C. The intensities of hydroxyapatite (HA) reflections in the X-ray diffraction (XRD) patterns of the pellets were retrieved to as-sintered state. The pellet surface morphology shows that CPP crystallites were clearly present and make an amorphous calcium phosphate (ACP) to discriminate against become to the area of slice join together. In addition, the intensities of the CPP reflections in the XRD patterns were the highest when the pellets were immersed for 28 d. When the CPP powders were extracted from the pellets after immersion in the solution for 14 d, the viability of 3T3 cells remained above 90% for culture times from 1 to 4 d. The pellet surface morphology observed using optical microscopy showed that the cells did not adhere to the bottom of the sintered pellets when cultured for 4 d; however, some CPP phase precipitates were formed, as confirmed by XRD. In consequence, the results suggest that the sintered HA powders are good materials for use in biomedical applications because of their good biocompatibility.

1. Introduction

Among calcium phosphate-based ceramics, hydroxyapatite (HA, $Ca_{10}(PO_4)_6(OH)_2$) and β -tricalcium phosphate (β -TCP, β - $Ca_3(PO_4)_2$) are the most commonly used as bioresorbable materials and tissue-engineering scaffolds [1–3] because these ceramics are biocompatible, nontoxic, and resorbable, and because they exhibit excellent osteoconductive ability. HA has widely been used as bone cement and implant material for direct bone-to-bone grafts [4–6]. Nevertheless, natural bone is a nanocomposite combination consisting of an organic fraction and a mineral fraction containing a small amount of apatite crystals and nonstoichiometric calcium phosphate, which jointly confer mechanical resistance [7]. Therefore, applications of HA are currently limited to powders, coatings, porous bodies, and non-load-bearing implants owing to process difficulties and

to the poor mechanical properties of conventional HA also reported by Suchanek and Yoshimura [8].

Prepared nanosized HA has received much attention in recent years for simulating natural structures [9–11]. Nanoscale-engineered HA would exhibit amazing functional properties owing to its small crystallite size, large surface area to volume ratio, and ultrafine structure similar to that of biological apatite, which would have a great effect on the interaction of cells implanted in the body. In addition, the nanoscale particle size and morphology of HA can control the sinterability, solubility, mechanical reliability, and osteoconductivity of HA [12, 13]. It is important to investigate methods of fabricating HA powders at low temperature such as sol-gel [14, 15], salt hydrolysis [16–18], electrochemical deposition [19–23], microemulsion [24], microwave irradiation [25], and hydrothermal reaction [26]. Using wet chemical methods to prepare HA powders usually

results in fine-grained microstructures, even submicron- to nanocrystallites, which are better accepted by the host tissue.

Although HA powders have previously been fabricated using calcium hydrogen phosphate dihydrate ($\text{CaHPO}_4 \cdot 2\text{H}_2\text{O}$, DCPD) and calcium carbonate (CaCO_3) as starting materials with hydrolysis [12], calcium-deficient HA (d-HA, $\text{Ca}_{10-x}(\text{HPO}_4)_x(\text{PO}_4)_{6-x}(\text{OH})_2 \cdot n\text{H}_2\text{O}$, for $0 \leq x \leq 1$) was formed, and there was significant lattice disparity between $\text{Ca}_{20}\text{Na}_{2x}(\text{P}_2\text{O}_7)_{1-x}(\text{PO}_4)_{12+2x}$ and $\text{Ca}_{10-x}\text{Na}_x(\text{PO}_4)_{6-x}(\text{CO}_3)_{1+x}$ at calcination temperatures from 600 to 1000°C. The arrangements of phosphate in the structure give two different channels for calcium atoms under two different environments [26]. The phosphate or hydroxyl groups can be substituted with carbonate species [27]. When the d-HA powders are sintered above 800°C, on the other hand, a small amount of rhenanite (CaNaPO_4) phase is formed with the HA. The sintered HA must first be put through the immersion test to determine the biocompatibility of sintered calcium phosphate prepared in a ratio of $[\text{Ca}]/[\text{P}] = 1.50$.

In the present study, variations in the surfaces of sintered calcium phosphate pellets prepared in a ratio of $[\text{Ca}]/[\text{P}] = 1.50$ and immersed in a normal saline solution at 37°C were observed and the biocompatibility of calcium phosphate powders and the sintered pellets were investigated. The main purposes of this work were to: (i) understand the surface transition behavior of the sintered calcium phosphate pellet prepared in a ratio of $[\text{Ca}]/[\text{P}] = 1.50$ and immersed in a normal saline solution for various of time, (ii) study the mechanism of dissolution and changes in the properties of sintered the calcium phosphate pellet after it has been immersed in culture medium for various time, (iii) determine the biocompatibility of calcium phosphate powders prepared in a ratio of $[\text{Ca}]/[\text{P}] = 1.50$, and (iv) study the biocompatibility of the sintered calcium phosphate pellet prepared in the ratio of $[\text{Ca}]/[\text{P}] = 1.50$.

2. Experimental Procedure

2.1. Sample Preparation. In the present study, calcium hydrogen phosphate dihydrate ($\text{CaHPO}_4 \cdot 2\text{H}_2\text{O}$, DCPD, purity $\geq 98\%$, Riedel-de Haen, Germany) and calcium carbonate (CaCO_3 , purity $\geq 98.5\%$, Riedel-de Haen, Germany) were used as the starting materials. First, either 0.1 M DCPD was mixed with CaCO_3 in a ratio of $[\text{Ca}]/[\text{P}] = 1.50$ or pure DCPD was poured into a 500 mL NaOH solution (pH = 13, purity $\geq 99\%$, Showa Co., Japan). The mixtures were blended separately in a high-speed agitator at 75°C for 1 h. After hydrolysis, the reactions were stopped by cooling the reaction mixtures in ice water. The precipitate products were filtered and then rinsed in deionized water. The products were subsequently dried at 60°C and sieved with a 300 mesh until further use.

The synthesized powder prepared in a ratio of $[\text{Ca}]/[\text{P}] = 1.50$ was used as received without any binders added. Each sample consisted of 0.25 g of synthesized powder uniaxially cool-pressed at 23 MPa to form a 10 mm ϕ pellet. The pellets were then sintered by heating them from 25 to 800°C at a rate

of 2°C/min for 4 h in air. After all the samples were sintered, they were removed from the furnace and were cooled in air.

2.2. Sample Characterization. X-ray diffraction (XRD) analysis on the crystalline phase of the as-dried and sintered samples was performed before and after they were immersed in normal saline solution at 37°C for various amounts of time. The analysis was performed using an X-ray diffractometer (Rigaku D-Max/III, Tokyo, Japan) with monochromatic $\text{Cu-K}\alpha$ radiation ($\lambda = 1.5405 \text{ \AA}$) and a Ni filter. The operation voltage and current were 30 kV and 20 mA at a scanning rate (2θ) of 1°/min.

The surface morphology of the sintered pellets was observed using scanning electron microscopy (SEM, Model XL 40 FE-SEM, Philips, Eindhoven, Netherlands). After the sintered pellets had been immersed in the normal saline solution at 37°C for various times, they were freeze dried at -55°C in vacuum and were then coated with gold.

The Ca^{2+} concentration was detected using inductively coupled plasma-mass spectrometry (ICP-MS). An ELAN 6100 DRC II ICP-MS (Perkin-Elmer, Concord, ON, Canada) was used for these experiments. Samples were introduced using a pneumatic nebulizer with a Scott spray chamber. The operating conditions of ICP-MS were optimized by continuously introducing saline solution after the immersed calcium phosphate samples containing unknown Ca^{2+} concentrations). The unused saline was treated as the blank and was added to the standard solution used to produce a calibration curve. The solution flow rate was maintained at about 1.5 mL·min⁻¹.

2.3. Determination of Biocompatibility with 3T3 Cells. The calcium phosphate powder pellets prepared in a ratio of $[\text{Ca}]/[\text{P}] = 1.50$ were sterilized and immersed in a culture medium for 4, 7, 14, or 21 d at 37°C. The resulting media were then used to culture 3T3 fibroblasts. About 1×10^4 3T3 cells in 100 μL of immersion medium were seeded into each well of a 96-well culture plate and were cultured for 1, 2, 3, or 4 d. Cell viability was determined using MTT (3-(4,5-dimethylthiazol-2-yl)-2,5-diphenyltetrazolium bromide) assay. In addition, the sintered pellet of calcium phosphate prepared in the ratio of $[\text{Ca}]/[\text{P}] = 1.50$ was placed into an 80 mm dish and immersed in 75% alcohol for sterilization. After 24 h, the residual alcohol on the sintered pellet was removed by washing the pellet with the culture medium. The washed sintered pellet was then immersed in the culture medium. About 1×10^4 3T3 cells were seeded onto the sintered pellet and were incubated in a 5% CO_2 atmosphere for 4 d at 37°C so that the cells could adhere to the pellet. The morphology of the cells adhered to sintered pellet was observed with an optical microscope and scanning electron microscopy.

3. Results and Discussion

3.1. Transition on Surface of Sintered Calcium Phosphate Pellet Prepared in a Ratio of $[\text{Ca}]/[\text{P}] = 1.50$ and Immersed in Normal Saline Solution. Figure 1 shows the XRD patterns for

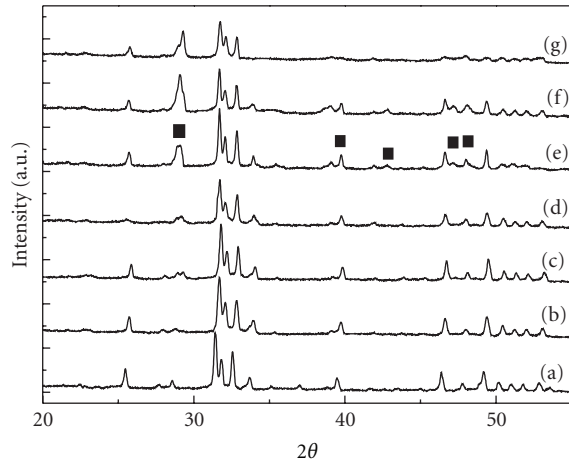


FIGURE 1: XRD patterns for sintered calcium phosphate pellets prepared in ratio of $[Ca]/[P] = 1.50$ and immersed in normal saline solution at $37^{\circ}C$ for various lengths of time (■: $Ca_2P_2O_7$). (a) 0 d, (b) 2 d, (c) 4 d, (d) 7 d, (e) 14 d, (f) 28 d, and (g) 42 d.

the synthesized calcium phosphate powder pellets prepared in a ratio of $[Ca]/[P] = 1.50$ after the pellets had been sintered at $800^{\circ}C$ for 4 h and immersed in a normal saline solution at $37^{\circ}C$ for various lengths of time. Figure 1(a) shows the XRD pattern for the as-sintered sample. The pattern indicates that the pellet was composed of HA and rhenanite ($NaCaPO_4$) as the major and minor phases, respectively, and that no other phase(s) were detected. $NaCaPO_4$ had formed because of Na^+ ions interstitial to the apatite structure. The XRD pattern for the sample that had been immersed for 2 d is shown in Figure 1(b). Bragg's angle of all reflection peaks for HA had obviously shifted to high-angle sites. Although the degree of splitting of the (112) and (200) reflections of HA decreased, their intensity of the reflections did not change and no other phases had formed. Figure 1(c) shows the XRD pattern for the sintered calcium phosphate pellet prepared in a ratio of $[Ca]/[P] = 1.50$ and immersed for 4 d. The pattern reveals a new weaker reflection peak at $2\theta \approx 29.3^{\circ}$. Nevertheless, all reflection peaks associated with HA have obviously shifted to higher angle sites, and the intensities of all the HA reflection peaks are slightly decreased. These phenomena occur because new substances form layers covering up previous ones on the surface of the pellet. The XRD pattern for the HA-sintered pellet immersed for 7 d is shown in Figure 1(d). Although the angles of the HA reflection peaks had returned to their original sites, the intensities of the HA reflection peaks were significantly decreased due to the intensity of the reflection peak associated with the new phase as well gradually obvious but the phase does not identify. Figure 1(e) shows the XRD pattern for the calcium phosphate pellet prepared in a ratio of $[Ca]/[P] = 1.50$ and immersed for 14 d. The pattern reveals that a new phase, calcium pyrophosphate ($Ca_2P_2O_7$; CPP, JCPDS card no. 73-0440), had formed on the surface of the pellet, and the intensities of the HA reflection peaks also returned to the same level as those of the as-sintered pellets because amorphous calcium phosphate (ACP) had

been used as the precursor substance for CPP, resulting in the intensities of the HA reflection peaks decreasing and angle of peak-site shifting. However, no new reflection peaks appeared. The CPP crystals formed on the surface of the sintered calcium phosphate pellet immersed for 14 d then the sites of the HA reflection peaks returned to their original sites as in the pattern for the as-sintered pellet. Figure 1(f) shows the XRD pattern for the sintered calcium phosphate pellet prepared in a ratio of $[Ca]/[P] = 1.50$ and immersed in a normal saline solution at $37^{\circ}C$ for 28 d. The intensities of CPP reflection peaks in this pattern were the highest because the increased thickness of the CPP crystallization layer led to further decrease in the intensity of the HA reflection peaks. The XRD patterns for the pellets immersed for 42 d are shown in Figure 1(g). Except for the successive decreases in the intensities of the HA reflection peaks, the intensities of CPP reflections also decrease.

3.2. Surface Morphologies of Immersed Sintered Calcium Phosphate Pellets Prepared in a Ratio of $[Ca]/[P] = 1.50$. The SEM images of the surface morphologies of the calcium phosphate powder synthesized in a ratio of $[Ca]/[P] = 1.50$, sintered at $800^{\circ}C$ for 4 h, and immersed in a normal saline solution at $37^{\circ}C$ for various lengths of time are shown in Figure 2. The surface morphology of the pellet immersed for 2 d is shown in Figure 2(a). A few of the HA grain boundaries appear blurred because the surface of the sintered sample is covered by an unknown substance. Figure 2(b) shows SEM image of the surface morphology of the sintered calcium phosphate sample immersed for 4 d. Amorphous substances were layered on the sample surface. The surface morphology of the sintered calcium phosphate sample immersed for 7 d is shown in Figure 2(c). A minute amount of irregular aggregated phase precipitate exists in addition to the amorphous substances on the surface. From the result shown in Figure 1(d), these amorphous substances and irregular aggregated phase precipitate correspond to the precursors of CPP and CPP crystallites, respectively. Figure 2(d) shows the SEM image of the surface morphology of the sintered calcium phosphate sample immersed in normal saline solution at $37^{\circ}C$ for 14 d. The CPP crystallites were clearly observed and made the amorphous substance to discriminate against become to the area of slice join together. This phenomenon also caused the intensity of the HA reflection peaks to increases. The surface morphology of the sintered calcium phosphate pellet immersed for 28 d is shown in Figure 2(e). Although amorphous substances are not observed on the surface, the whole HA surface is covered by CPP, leading to a decrease in the intensities of HA the reflection peaks. Figure 2(f) shows the surface morphology of the sintered calcium phosphate sample immersed in a normal saline solution at $37^{\circ}C$ for 42 d. The CPP has formed a linked flat-plane structure over the entire HA surface.

3.3. Variations in Postimmersion Concentration of Ca^{2+} Ions and Rate of Weight Loss of Sintered Calcium Phosphate Pellet Prepared in a Ratio of $[Ca]/[P] = 1.50$. In general, the Ca^{2+} ions in solution play the role of inducing phosphate

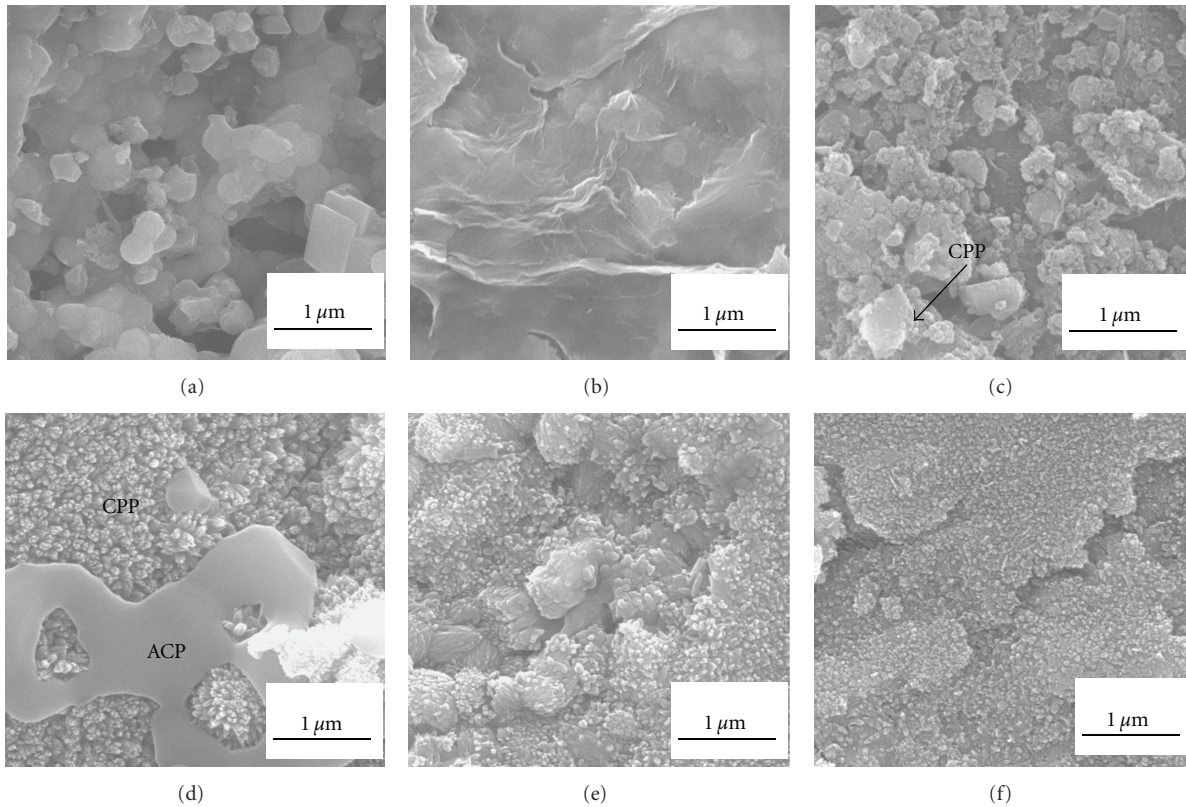


FIGURE 2: SEM images of microstructures on surface of sintered calcium phosphate pellets prepared in ratio of $[Ca]/[P] = 1.50$ and immersed in normal saline solution at $37^{\circ}C$ for various lengths of time: (a) 2 d, (b) 4 d, (c) 7 d, (d) 14 d, (e) 28 d, and (f) 42 d.

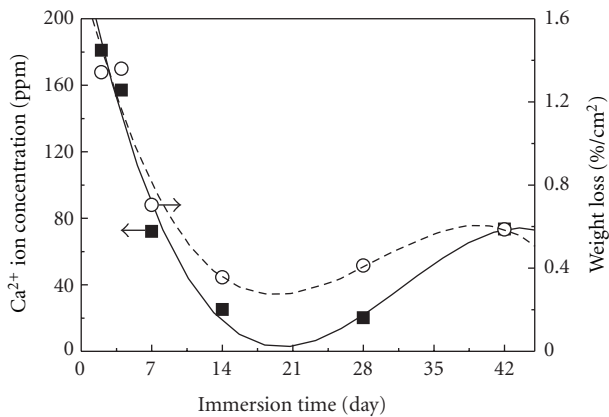


FIGURE 3: Concentration of Ca^{2+} ions and rate of weight loss of sintered calcium phosphate pellets immersed in normal saline solution at $37^{\circ}C$ for various lengths of time.

precipitation. However, because of the presence of phosphorous (P) in the solution, the pH can change, possibly forming various ions such as $H_2PO_4^-$, HPO_4^{2-} , and PO_4^{3-} . Therefore, during immersion, except test the self change of HA sintered sample, variation in the solution composition is a significant contributor to the transformation of the sintered calcium phosphate samples. From the change in the Ca^{2+} concentration in the immersion solution measured using

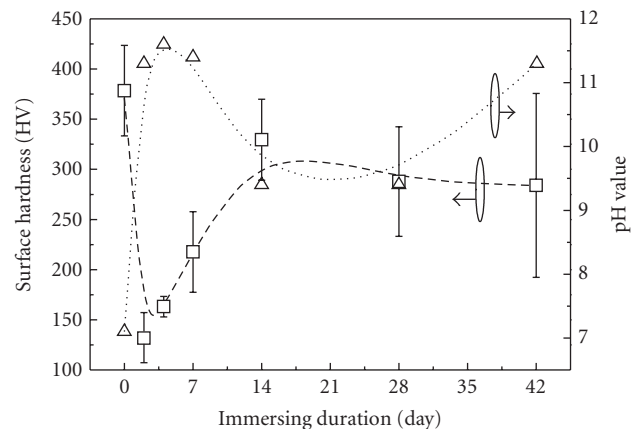


FIGURE 4: Surface hardness of sintered calcium phosphate pellets and pH of normal saline solutions in which pellets had been immersed at $37^{\circ}C$ for various lengths of time.

ICP-MS and the difference in the weight for sintered calcium phosphate sample measured before and after immersion, the variation in the sintered calcium phosphate samples during immersion can be investigated.

Figure 3 shows the variation in the concentration of Ca^{2+} ions and rate of weight loss per unit of surface area of sintered calcium phosphate samples prepared in the ratio of $[Ca]/[P]$

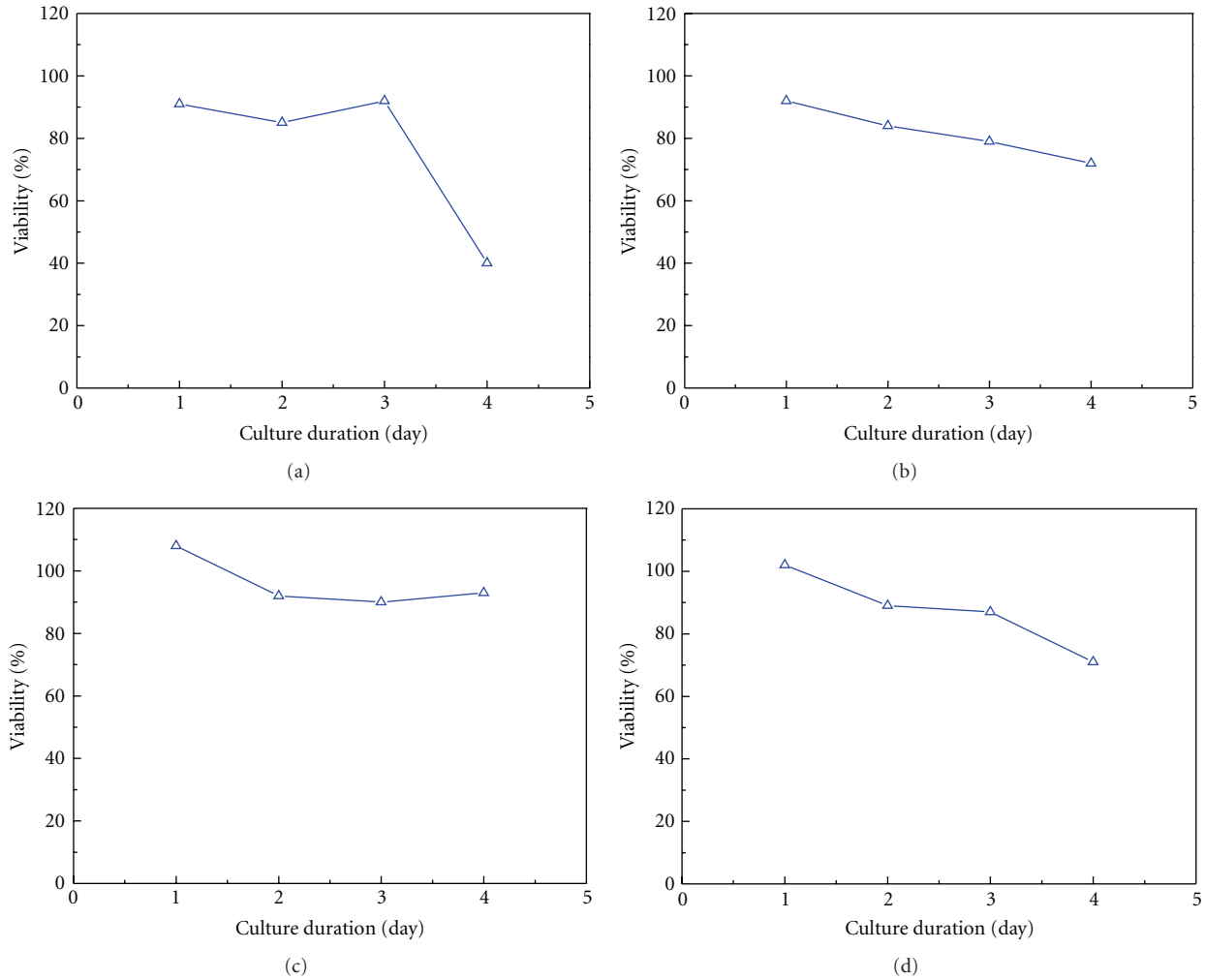


FIGURE 5: Viability of 3T3 cells cultured for various lengths of time in solutions of calcium phosphate powder extracted from pellets prepared in ratio of $[Ca]/[P] = 1.50$.

= 1.50 and immersed in a normal saline solution at 37°C for various lengths of time. The concentration of Ca^{2+} ions in the solution increased from 0 to 181 ppm, and the rate of weight loss per unit of surface area was $1.34\%/cm^2$ for the sample immersed for 2 d. This result indicates that the unstable calcium phosphate degraded and was released into the solution. When the immersion time increased to 14 d, the concentration of Ca^{2+} ions in the solution rapidly decreased and the rate of weight loss per unit of surface area decreased because the calcium phosphate product had reformed on the surface of the sintered calcium phosphate from the Ca^{2+} ions in the solution. This result is consistent with the XRD result and SEM observation for the amorphous substance precipitates. The concentration of Ca^{2+} ions in the solution gradually increased when the immersion time was longer than 14 d because the amorphous substance dissolved into the normal saline solution, and the CPP reformed. When the sintered calcium phosphate pellet was immersed for 42 d, the concentration of Ca^{2+} ions in the solution and the rate of weight loss of the sintered calcium phosphate pellet reached equilibrium. This result suggests that the equilibrium of

the precipitation-dissolution reactions for ACP and CPP had approached completion.

3.4. The Variation in Pre- and Postimmersion Surface Hardness and pH of Immersion Solution after Sintered Calcium Phosphate Pellets Had Been Immersed for Various Lengths of Time.

The variation in surface hardness and the pH of immersion solution for sintered calcium phosphate samples immersed for various amounts of time are shown in Figure 4. The minimum HV was 132.1 for the sample immersed for 2 d, suggesting that the ACP formed on the surface of the sintered calcium phosphate pellet prepared in a ratio of $[Ca]/[P] = 1.50$. The hardness values subsequently increased rapidly with increasing immersion time because of the CPP precipitate but could not reach the level of the pre-immersion sintered calcium phosphate sample. The surface hardness approached a stable value for the sample immersed for 14 d, and the sample surface exhibited a gradual tendency toward steady state.

Figure 4 also shows that the pH of the normal saline solution increases during the initial stage of immersion

because of the ACP precipitating and dissolving into the solution. The maximum pH of the normal saline solution reached 11.7 when the sintered calcium phosphate sample prepared in a ratio of $[Ca]/[P] = 1.50$ had been immersed for 4 d. Then the pH of the solution decreased for samples immersed longer than 4 days because CPP had formed, leading to a decrease in the concentrations of calcium and phosphor ions in the normal saline solution. For the sample immersed for 28 d, the pH of the solution increased, revealing that the calcium and phosphor ions were rereleased into the normal saline solution.

3.5. Biocompatibility of Calcium Phosphate Powder Pellets Prepared in the Ratio of $[Ca]/[P] = 1.50$ with regard to 3T3 Cells. The viability of 3T3 cells cultured for various lengths of time in solutions of calcium phosphate extracted from the pellets immersed for various lengths of time is shown in Figure 5. Figure 5(a) shows that the viability of the 3T3 cells cultured in the solution of calcium phosphate extracted from the pellet immersed for 4 d is greater than 90% when the cells were cultured for 1 d. The high 3T3 cell viability is attributed to the addition of $CaCO_3$ to increase $[Ca]/[P]$ ratio to one that was similar to that of stoichiometric HA [18]. This caused carbonate-substituted hydroxyapatite (CHA) to form, leading to increased biocompatibility. When the 3T3 cells were cultured for 4 d, their viability was still about 40%.

The viability of 3T3 cells cultured for various lengths of time in solutions of calcium phosphate extracted from the pellet immersed for 7 d are shown in Figure 5(b). It seems that the viability of 3T3 cells cultured in solutions prepared from calcium phosphate powders prepared in $[Ca]/[P]=1.50$ extracted from HA is greater than 70% for each culture time. Figure 5(c) shows the viability of 3T3 cells cultured in a solution prepared from HA powders prepared in $[Ca]/[P]=1.50$ extracted from the pellet immersed for 14 d. The viability remains above 90% for culture times from 1 to 4 d because the Ca^{2+} ions released from the test samples prevented the pH of the solution from decreasing, thereby increasing cell viability. When the HA powders prepared in $[Ca]/[P]=1.50$ after being immersed for 21 d, the cell viability of the extraction of HA powders for various culture times are shown in Figure 5(d). From Figure 5, the difference between the viability 3T3 cells cultured in solutions prepared from calcium phosphate extracted from HA powders with $[Ca]/[P] = 1.5$ and the viability of those cultured in solutions prepared from calcium phosphate extracted from HA powders with $[Ca]/[P] = 1.0$ decreases increasing immersion time of the pellets (data not shown). The results shown in Figure 5 also indicate that the HA powders with $[Ca]/[P] = 1.5$ exhibit higher biocompatibility because the $[Ca]/[P]$ ratio approaches that of stoichiometric HA. Figure 6 shows the XRD pattern generated after cell culture for the precipitate from the HA-sintered pellet synthesized from DCPD and $CaCO_3$ prepared in a ratio of $[Ca]/[P] = 1.50$. The reflection peaks in the XRD pattern correspond to the CPP phase.

The morphologies of the 3T3 cells cultured on HA-sintered pellets prepared from DCPD and added $CaCO_3$ in

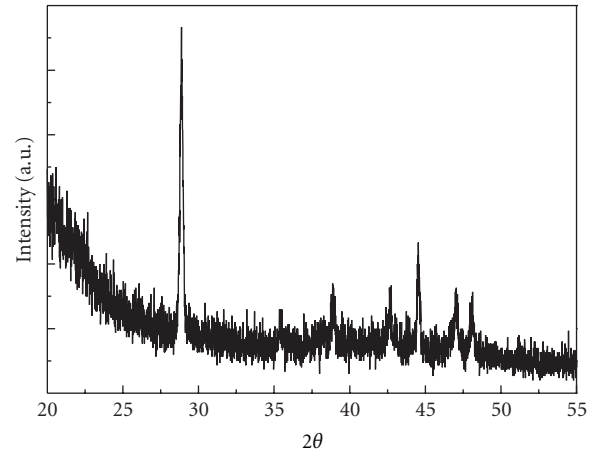


FIGURE 6: Post-cell-culture XRD pattern for precipitates of sintered calcium phosphate pellets prepared in ratio of $[Ca]/[P] = 1.50$.

the ratio of $[Ca]/[P] = 1.50$ are shown in Figure 7. Figure 7(a) shows optical microscopy (OM) image of the morphology of the cell adhesion on the bottom of the HA-sintered pellet after culturing for 4 d. Although the cells did not adhere to the bottom of the pellet, some precipitates had formed. The precipitates were identified as CPP, as shown in Figure 6. Figure 7(b) shows the enlarged view of Figure 7(a). The CPP precipitates consist of nonuniform polygons. The OM image of the morphology of the surrounding area on the sintered HA pellet is shown in Figure 7(c). The cell synapses were extended, and the cells exhibited interknit growth. This result may suggest that the release of ions during immersion of the sintered pellet had not affected the extended process of the normal mitosis of cells. Figure 7(d) shows the SEM image of the enlarged view of Figure 7(c). Some precipitates are surrounding the cells. From the preceding results and discussion, HA powders synthesized using DCPD and $CaCO_3$ as the starting materials in a ratio of $[Ca]/[P] = 1.50$ with hydrolysis can be good biomedical materials because they exhibit good biocompatibility.

4. Conclusions

The biocompatibility of HA-sintered pellets prepared in a ratio of $[Ca]/[P] = 1.5$ and powders prepared with various ratios of $[Ca]/[P]$ were investigated using XRD, OM, SEM, ICP-MS, a pH meter, an immersion test, and a cell culture. When the HA-sintered pellet was immersed in a normal saline solution at $37^\circ C$ for 4 d, XRD pattern exhibited a new weaker reflection peak at $2\theta \approx 29.3^\circ$, and all the reflection peaks associated with HA shifted to higher-angle sites; however, the intensities of all the HA reflection peaks slightly decreased. The CPP phase was formed on the surface of the pellets after the pellets had been immersed in the normal saline solution for 42 d. The SEM image of the surface morphology showed that amorphous precursors of CPP and irregular aggregated CPP crystallites had formed after the pellets had been immersed in the normal saline solution for 14 d. The CPP formed a linked flat-plane

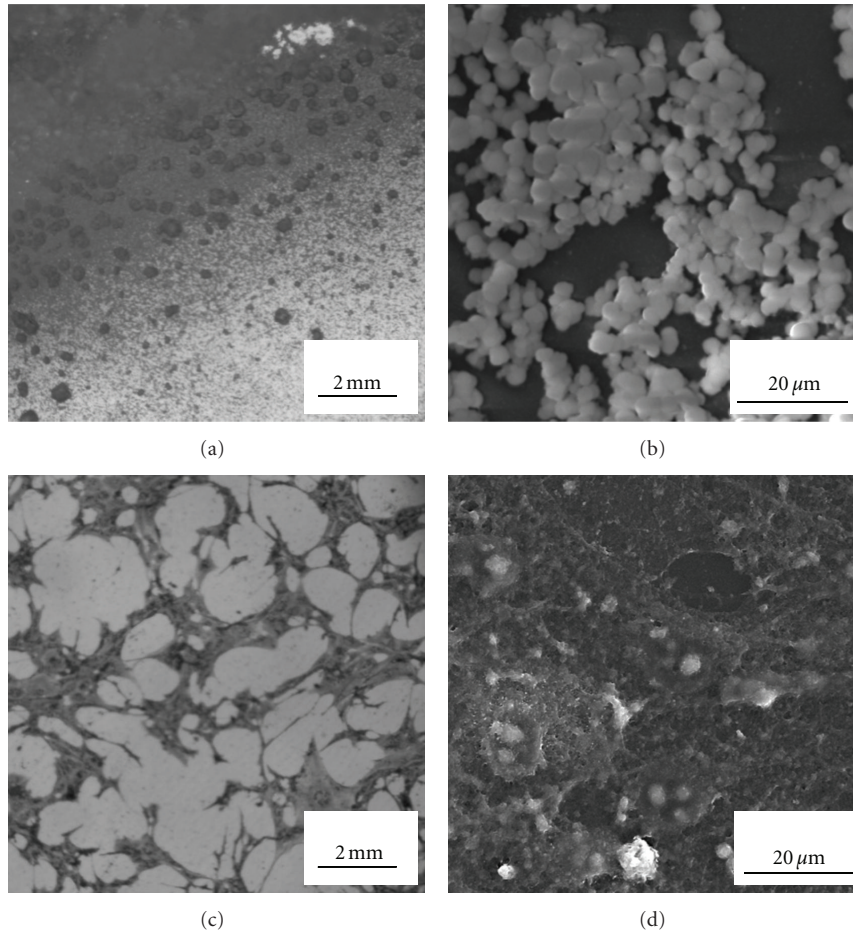


FIGURE 7: Morphologies of cells cultured on sintered calcium phosphate pellets prepared in ratio of $[Ca]/[P] = 1.50$: (a) OM image of precipitates, (b) SEM image of precipitates, (c) OM image of cell growth, and (d) SEM image of cell growth.

structure over the entire HA surface after the pellet had been immersed in a normal saline solution at 37°C for 42 d. In addition, when the pellet had been immersed in the normal saline solution for 42 d, the concentration of Ca^{2+} ions in the solution, and the rate of weight loss of the HA-sintered pellet reached an equilibrium because the precipitation-dissolution reactions for ACP and CPP had approached completion. The minimum surface hardness of HA was 132.1 because the ACP had formed on the HA-sintered sample immersed for only 2 d. The surface hardness then rapidly increased because of the CPP precipitate but could not reach to the level of hardness of sintered HA pellet before immersion. The maximum pH of the normal saline solution was 11.7 when the HA-sintered pellet had been immersed for 4 d. The viability of 3T3 cells remained above 90% for culture duration from 1 to 4 d with extracts of HA powders having $[Ca]/[P] = 1.50$ after the pellets had been immersed in a normal saline solution for 14 d. The HA-sintered pellet was prepared in a ratio of $[Ca]/[P] = 1.50$ after the cells had cultured for 4 d. Although the cells did not adhere on the bottom of the pellet, some CPP precipitate had formed. The morphology of the surrounding area on the HA-sintered pellet after the cells had cultured for 4 d shows that the cell

synapses were extended and that the cells exhibited interknit growth. Therefore, we suggest that HA powders synthesized using CPP and CaCO_3 in the ratio $[Ca]/[P] = 1.50$ with hydrolysis can be good biomedical materials because they exhibit good biocompatibility.

Acknowledgments

The authors gratefully acknowledge the financial support provided by the National Science Council of the Republic of China (Taiwan) under contract no. NSC 97-2221-E-037-001-MY3. The authors also gratefully acknowledge Mr. F. C. Wu and Mr. H. Y. Yao for their help with SEM and TEM imaging, respectively, when preparing the manuscript.

References

- [1] S. Kannan, A. F. Lemos, J. H. G. Rocha, and J. M. F. Ferreira, "Characterization and mechanical performance of the Mg-stabilized $\beta\text{-Ca}_3(\text{PO}_4)_2$ prepared from Mg-substituted Ca-deficient apatite," *Journal of the American Ceramic Society*, vol. 89, no. 9, pp. 2757–2761, 2006.

- [2] A. Bandyopadhyay, S. Bernard, W. Xue, and S. Böse, "Calcium phosphate-based resorbable ceramics: influence of MgO, ZnO, and SiO₂ dopants," *Journal of the American Ceramic Society*, vol. 89, no. 9, pp. 2675–2688, 2006.
- [3] S. S. Banerjee, S. Tarafder, N. M. Davies, A. Bandyopadhyay, and S. Bose, "Understanding the influence of MgO and SrO binary doping on the mechanical and biological properties of β -TCP ceramics," *Acta Biomaterialia*, vol. 6, no. 10, pp. 4167–4174, 2010.
- [4] L. L. Hench, "Bioceramics," *Journal of the American Ceramic Society*, vol. 81, no. 7, pp. 1705–1728, 1998.
- [5] J. M. Gomez-Vega, E. Saiz, A. P. Tomsia, G. W. Marshall, and S. J. Marshall, "Bioactive glass coatings with hydroxyapatite and Bioglass® particles on Ti-based implants. 1. Processing," *Biomaterials*, vol. 21, no. 2, pp. 105–111, 2000.
- [6] M. Swetha, K. Sahithi, A. Moorthi, N. Srinivasan, K. Ramasamy, and N. Selvamurugan, "Biocomposites containing natural polymers and hydroxyapatite for bone tissue engineering," *International Journal of Biological Macromolecules*, vol. 47, no. 1, pp. 1–4, 2010.
- [7] G. K. Lim, J. Wang, S. C. Ng, and L. M. Gan, "Processing of fine hydroxyapatite powders via an inverse microemulsion route," *Materials Letters*, vol. 28, no. 4–6, pp. 431–436, 1996.
- [8] W. Suchanek and M. Yoshimura, "Processing and properties of hydroxyapatite-based biomaterials for use as hard tissue replacement implants," *Journal of Materials Research*, vol. 13, no. 1, pp. 94–117, 1998.
- [9] M. Swetha, K. Sahithi, A. Moorthi et al., "Synthesis, characterization, and antimicrobial activity of nano-hydroxyapatite-zinc for bone tissue engineering applications," *Journal of Nanoscience and Nanotechnology*, vol. 12, pp. 167–172.
- [10] J. Chen, Q. Yu, G. Zhang, S. Yang, J. Wu, and Q. Zhang, "Preparation and biocompatibility of nanohybrid scaffolds by in situ homogeneous formation of nano hydroxyapatite from biopolymer polyelectrolyte complex for bone repair applications," *Colloids and Surfaces B*, vol. 93, pp. 100–107, 2012.
- [11] I. Brook, C. Freeman, S. Grubb et al., "Biological evaluation of nano-hydroxyapatite-zirconia (HA-ZrO₂) composites and strontium-hydroxyapatite (Sr-HA) for load-bearing applications," *Journal of Biomaterials Applications*, vol. 27, no. 3, pp. 291–298, 2012.
- [12] Y. Li, J. De Wijn, C. P. A. T. Klein, S. Van de Meer, and K. De Groot, "Preparation and characterization of nanograde osteoapatite-like rod crystals," *Journal of Materials Science*, vol. 5, no. 5, pp. 252–255, 1994.
- [13] G. Munir, G. Koller, L. Di Silvio, M. J. Edirisinghe, W. Bonfield, and J. Huang, "The pathway to intelligent implants: osteoblast response to nano silicon-doped hydroxyapatite patterning," *Journal of the Royal Society Interface*, vol. 8, no. 58, pp. 678–688, 2011.
- [14] D. B. Haddow, P. F. James, and R. Van Noort, "Characterization of sol-gel surfaces for biomedical applications," *Journal of Materials Science*, vol. 7, no. 5, pp. 255–260, 1996.
- [15] K. Hwang and Y. Lim, "Chemical and structural changes of hydroxyapatite films by using a sol-gel method," *Surface and Coatings Technology*, vol. 115, no. 2–3, pp. 172–175, 1999.
- [16] K. Ohta, M. Kikuchi, J. Tanaka, and H. Eda, "Synthesis of c axes oriented hydroxyapatite aggregate," *Chemistry Letters*, vol. 9, pp. 894–895, 2002.
- [17] W. J. Shih, Y. F. Chen, M. C. Wang, and M. H. Hon, "Crystal growth and morphology of the nano-sized hydroxyapatite powders synthesized from CaHPO₄·2H₂O and CaCO₃ by hydrolysis method," *Journal of Crystal Growth*, vol. 270, no. 1–2, pp. 211–218, 2004.
- [18] W. J. Shih, M. C. Wang, and M. H. Hon, "Morphology and crystallinity of the nanosized hydroxyapatite synthesized by hydrolysis using cetyltrimethylammonium bromide (CTAB) as a surfactant," *Journal of Crystal Growth*, vol. 275, no. 1–2, pp. e2339–e2344, 2005.
- [19] S. Ban and J. Hasegawa, "Morphological regulation and crystal growth of hydrothermal-electrochemically deposited apatite," *Biomaterials*, vol. 23, no. 14, pp. 2965–2972, 2002.
- [20] S. K. Yen and C. M. Lin, "Cathodic reactions of electrolytic hydroxyapatite coating on pure titanium," *Materials Chemistry and Physics*, vol. 77, no. 1, pp. 70–76, 2003.
- [21] W. J. Shih, Y. H. Chen, S. H. Wang, W. L. Li, M. H. Hon, and M. C. Wang, "Effect of NaOH_(aq) treatment on the phase transformation and morphology of calcium phosphate deposited by an electrolytic method," *Journal of Crystal Growth*, vol. 285, no. 4, pp. 633–641, 2005.
- [22] M. C. Wang, W. J. Shih, K. M. Chang, S. H. Wang, W. L. Li, and H. H. Huang, "Effect of process parameters on the crystallization and morphology of calcium phosphate at a constant pressure of 80 Torr," *Journal of Non-Crystalline Solids*, vol. 356, no. 31–32, pp. 1546–1553, 2010.
- [23] W. J. Shih, M. C. Wang, K. M. Chang et al., "Phase transformation of calcium phosphates by electrodeposition and heat treatment," *Metallurgical and Materials Transactions A*, vol. 41, pp. 3509–3516, 2010.
- [24] W. Pon-On, S. Meejoo, and I. M. Tang, "Formation of hydroxyapatite crystallites using organic template of polyvinyl alcohol (PVA) and sodium dodecyl sulfate (SDS)," *Materials Chemistry and Physics*, vol. 112, no. 2, pp. 453–460, 2008.
- [25] T. Ma, Z. Xia, and L. Liao, "Effect of reaction systems and surfactant additives on the morphology evolution of hydroxyapatite nanorods obtained via a hydrothermal route," *Applied Surface Science*, vol. 257, no. 9, pp. 4384–4388, 2011.
- [26] H. El Feki, J. M. Savariault, and A. B. Salah, "Structure refinements by the Rietveld method of partially substituted hydroxyapatite: Ca₉Na_{0.5}(PO₄)_{4.5}(CO₃)_{1.5}(OH)₂," *Journal of Alloys and Compounds*, vol. 287, no. 1–2, pp. 114–120, 1999.
- [27] E. A. P. De Maeyer, R. M. H. Verbeeck, and D. E. Naessens, "Stoichiometry of Na⁺- and CO₃²⁻-containing apatites obtained by hydrolysis of monetite," *Inorganic Chemistry*, vol. 32, no. 25, pp. 5709–5714, 1993.

Research Article

Property Evaluation of *Bletilla striata*/Polyvinyl Alcohol Nano Fibers and Composite Dressings

Jia-Horng Lin,^{1,2} Chao-Tsang Lu,³ Jin-Jia Hu,⁴
Yueh-Sheng Chen,⁵ Chen-Hung Huang,⁶ and Ching-Wen Lou⁷

¹Laboratory of Fiber Application and Manufacturing, Department of Fiber and Composite Materials, Feng Chia University, Taichung 40724, Taiwan

²School of Chinese Medicine, China Medical University, Taichung 40402, Taiwan

³Graduate Institute of Biotechnology, Central Taiwan University of Science and Technology, Taichung 40601, Taiwan

⁴Department of Biomedical Engineering, National Cheng Kung University, Tainan 70101, Taiwan

⁵Department of Biomedical Imaging and Radiological Science, China Medical University, Taichung 40402, Taiwan

⁶Department of Aerospace and Systems Engineering, Feng Chia University, Taichung 40724, Taiwan

⁷Institute of Biomedical Engineering and Material Science, Central Taiwan University of Science and Technology, Taichung 40601, Taiwan

Correspondence should be addressed to Ching-Wen Lou, cwlou@ctust.edu.tw

Received 19 June 2012; Accepted 25 September 2012

Academic Editor: Xiao-Miao Feng

Copyright © 2012 Jia-Horng Lin et al. This is an open access article distributed under the Creative Commons Attribution License, which permits unrestricted use, distribution, and reproduction in any medium, provided the original work is properly cited.

This study used nonwoven manufacture and electrospinning to create wound dressings with solid mechanical properties and hemostasis function. 10% Polyvinyl alcohol (PVA) and 5% *Bletilla striata* (BS) were blended into the PVA/BS solution, which can be made into nanomaterial with high specific surface area by electrospinning. The PVA/BS solution was electrospun onto the dressing matrix made of polyester (PET) and absorbent cotton (AC), forming the PVA/BS composite dressings. According to the experiment results, when the volume ratio of PVA to BS was 9 : 1, the resulting dressings had optimal fiber formation, the finest average diameter, and the lowest toxicity.

1. Introduction

Wound dressings are divided into gauze dressing, synthetic dressing, and biological dressing. Gauze dressings are composed of cellulose fibers or fur, such as gauze, cotton pad, or wool. This type of dressings is used to cover the wounds for a temporal protection and needs to be changed periodically. As various polymer materials have been developed as a result of chemical industry advances, there are many products for wounds; however, they are only good for skin-layer wounds, not for deep and large wounds [1–3].

In addition, sponge-form and spray-form synthetic dressings are available in the market; the design of synthetic dressings is further improved to be double-layer and multilayer, the former of which is composed of durable outer layer and adhesive and resilient inner layer. As all the aforementioned dressings do not significantly help large

and deep burns, biological dressings with better quality and functionality are thus developed. An ideal dressing has to be able to keep wounds moist, to prevent the wounds from the second injury, to absorb the oozed blood and tissue fluid, to accelerate wound healing, as well as to have good resilience, tear strength, abrasion, and biocompatibility [4–8].

Electrospinning was first developed in 1900, when people placed melted sealing wax in an electric field, and solid fibers were jetted from the high-voltage end and accumulated on collector, forming membranes. Zeleny [9] explored the behavior of fluid droplets from a metal capillary under static electricity, and Formals (1934) published a complete electrospinning manufacturing that can successfully produce polymer filaments and that obtained the patent of electrospinning in US [10–12]. Fibers made by electrospinning are much finer than those by conventional spinning, yielding a diameter varying from tens to thousands of nanometers.

The most desired functionality of electrospinning is to have nano fibers with considerable specific surface area, which could be largely applied in biomedicine, such as wound dressing, and tissue engineering scaffolding, tissue engineering vascular graft [13–16].

Polyvinyl alcohol (PVA), made from the hydrolyzed polyvinyl acetate, is primarily composed of hydrophobic acetyl group ($-\text{CH}_3\text{COO}$) and hydrophilic hydroxyl group ($-\text{OH}$). The side chain of molecular chain of PVA has a great amount of hydroxyl groups, imparting PVA great hydrophile. In addition, PVA also has good biocompatibility, nontoxicity, formability, and chemical and heat stability [17, 18]. *Bletilla striata* (BS), a traditional Chinese medicine, is good for wound healing, hemostasis, detumescence, and granulation. It also helps to recover cuts, abrasion, toxin of wound tumescence, pulmonary hemorrhage, and gastric ulcer. Current studies have found that BS has glysan, volatile oil, and starch, which activate platelets, shorten time for thrombin generation, and suppress activity protease. Therefore, it shortens thrombin time, restricts fibrinolysis, and forms artificial thrombus so as to yield hemostasia [19–22].

Wounds, burns, surgical wounds, or acute wounds that have excessive bleeding demand an efficient wound dressings. In this study, PVA and BS solutions were first mixed with various volume ratios and then electrospun onto a PET/AC matrix, forming a hemostatic composite dressing. As PVA is able to complement BS for fiber formation, electrospinning is able to make polymer solution into micrometer fibers, and even nanometer fibers. The PVA/BS nano fibers differ from the previous PVA nano fibers in having the addition of *Bletilla striata*, which has functions of hemostasis and detumescence. When electrospun into nano fibers, *Bletilla striata* has a high specific surface area; this increases the contact area between it and wounds, leading to an efficient treatment. The PVA/BS composite dressings thus had good mechanical properties, hemostasia, and biocompatibility. In addition, high specific surface area of the constituent PVA/BS nano fibers largely increased the contact area between BS and the wound, facilitating the hemostasia and healing. The PVA/BS nano fibers could be used as carrier for drug delivery, tissue engineering, tissue repair substitutes and wound dressing material.

2. Experiment

2.1. Material. PVA was purchased from Nihon Shiyaku Industries, Japan. BS was purchased from Fu Tan Pharmaceutical Co., Ltd., Taiwan. Deionized water was offered by Feng Chia University, Taiwan. L929 fibroblasts were supplied by Institute of Life Sciences, Taiwan.

2.2. Electrospinning. In the first stage, PVA powder and BS powder were respectively, dissolved with deionized water, formulating 10 wt% PVA solution and 5 wt% BS solution. Two solutions were then mixed with volume ratios of 10:0, 9:1, 8:2, 7:3, 6:4, 5:5, or 0:10 and then measured for viscosity. Afterward, these solutions were made into films and membrane by heating and electrospinning, respectively.

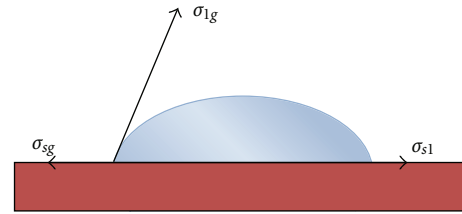


FIGURE 1: Illustration of contact angle.

The electrospinning machine was offered by the Laboratory of Fiber Application and Manufacturing, Feng Chia University, Taiwan. The settings of electrospinning were as follows: the voltage was 12 kV, the distance between the collector and needle was 12 cm, the syringe flow was 0.75 mL/h. The films were evaluated in terms of contact angle while the membranes were observed by a scanning electron microscopy (SEM), according to which the optimal volume ratio of PVA to BS was thus determined.

In the second stage, the optimal volume ratio of PVA to BS was obtained from the first stage, the voltage of electrospinning was constant (12 kV), the distance between collector and needle varied from 8, 10, 12, 15 to 20 cm, and the syringe flow varied from 0.50, 0.75, to 1.00 mL/h. The resulting PVA/BS membranes were then observed by an SEM to determine the electrospinning parameters.

2.3. Preparation of Composite Dressings. The optimum parameters of fiber formation were used to in electrospinning process: PVA/BS mixture solution was electrospun on the optimal dressing matrix from the preliminary study [23], forming the PVA/BS composite wound dressings. The resulting samples were then evaluated in terms of tear strength, tensile strength, flexibility, and air permeability to determine the dressings' mechanical properties and comfort on users' skin.

2.4. Tests

2.4.1. Contact Angle Evaluation. Contact angle was based on Young's formula [24] proposed in 1805 as below:

$$\sigma_{lg} \cos \theta = \sigma_{sg} - \sigma_{sl}, \quad (1)$$

where σ_{lg} was the interfacial tension between liquid and gas, σ_{sg} was the interfacial tension between solid and gas, σ_{sl} was the interfacial tension between solid and liquid, and θ was the contact angle, all of which were exemplified in Figure 1. PVA/BS solutions with various volume ratios were made into films and then evaluated by a contact angle meter (Kyowa Interface Science Co., Ltd., Japan). The number of test samples was six.

2.4.2. Observation of Scanning Electron Microscopy. PVA/BS solutions with various volume ratios were, respectively, electrospun into membranes, gilt, and then observed by a scanning electron microscopy (SEM, S3000N, Hitachi Ltd., Japan).

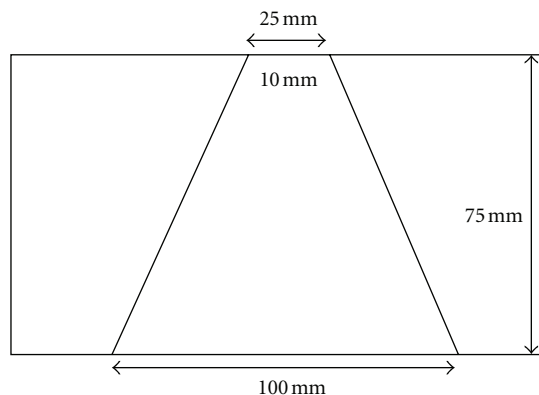


FIGURE 2: Sample of tear strength test.

2.4.3. Cell Biocompatibility Test. In *in vitro* test, PVA/BS membranes were tested for cell biocompatibility, as specified in ASTM F813-83. The membranes of 1 cm × 1 cm were placed in a dish, where the L929 fibroblasts and medium were both infused. After cell culture, samples were observed for the cell growth.

2.4.4. Tensile Strength Test. This test was conducted according to CNS 12915, using a universal strength tester (HT-9101, Hung Ta Instrument Co., Ltd., Taiwan). Ten composite dressings of 150 mm × 25.4 mm were each taken along machine direction (MD) or cross machine direction (CD). The yields of values were averaged for definitive mean and standard deviation.

2.4.5. Tear Strength Test. A universal strength tester (HT-9101, Hung Ta Instrument Co., Ltd., Taiwan, ROC) evaluated the tear strength of the composite dressings, as specified in CNS 12915. Figure 2 illustrates the sample size. Ten samples, each taken along the CD or MD, were evaluated for the definitive mean and standard deviation.

2.4.6. Air Permeability Test. This test was performed as specified in ASTM D737, using an air permeability tester (FX 3300, Textest AG, Switzerland). The composite dressings were tested thirty times at different locations, and the values were then averaged for definitive mean.

2.4.7. Flexibility Test. A flexometer (Hung Ta Instrument Co., Ltd., ROC) was used to test the composite dressings, according to CNS 12915. Six samples of 150 mm × 25.4 mm, each taken along the MD and CD, were tested for definitive mean and standard deviation.

3. Results and Discussion

3.1. Contact Angle of Films Made by PVA/BS Solutions with Various Volume Ratios by Heating. Figure 3 shows the contact angles of PVA/BS films made with various volume ratios. With an increase in BS content, the contact angle of

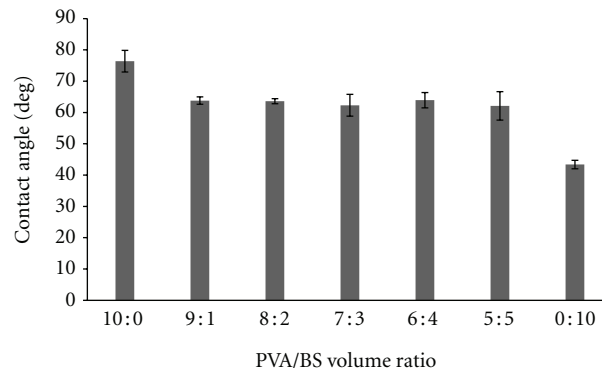


FIGURE 3: Contact angles as related to various PVA/BS volume ratios of the resulting films.

TABLE 1: Mean of fiber diameter and viscosity of the PVA/BS solution as related to various BS contents.

BS content (%)	Mean of fiber diameter (Nm)	Viscosity of PVA/BS solution (cp)
0	181 ± 41	450.0
10	179 ± 28	378.0
20	177 ± 35	321.4
30	164 ± 41	230.7
40	212 ± 34	155.2
50	256 ± 38	69.1
100	N/A	41.7

PVA/BS films decreased. This decrease was due to the fact that the molecular chains of PVA had a greater amount of chemicals found in the hydrophilic group (–OH) and some found in the hydrophobic group (–COOCH₃); the major component of BS was carbohydrate, which was composed of carbon molecules and a great amount of certain hydrophilic chemicals (–OH and –H). Therefore, an increase in BS content raised the amounts of hydrophilic groups in PVA/BS films, resulting in a greater hydrophile. This study shows that PVA/BS films were hydrophilic as the size of contact angle between the material and water was small.

3.2. SEM of Nanomembranes Made of PVA/BS Solutions with Various Volume Ratios by Electrospinning. Figure 4 shows the nano fibers made of PVA/BS solutions with volume ratios of 10:1 (pure PVA), 9:1, 8:2, 7:3, 6:4, and 5:5, by electrospinning. It was observed that when the BS content was increased, the electrospun fibers of PVA/BS solution exhibited distinct beads.

Table 1 reports the influence of various BS contents on the mean of fiber diameter and the viscosity of the PVA/BS solution. The mean of fiber diameter first decreased with an increase in the BS content, starting from 0, up to 10, 20, and 30%; when BS content exceeded 30%, the mean of fiber diameter then increased and was greater than that with 0% of BS content. An increase in BS

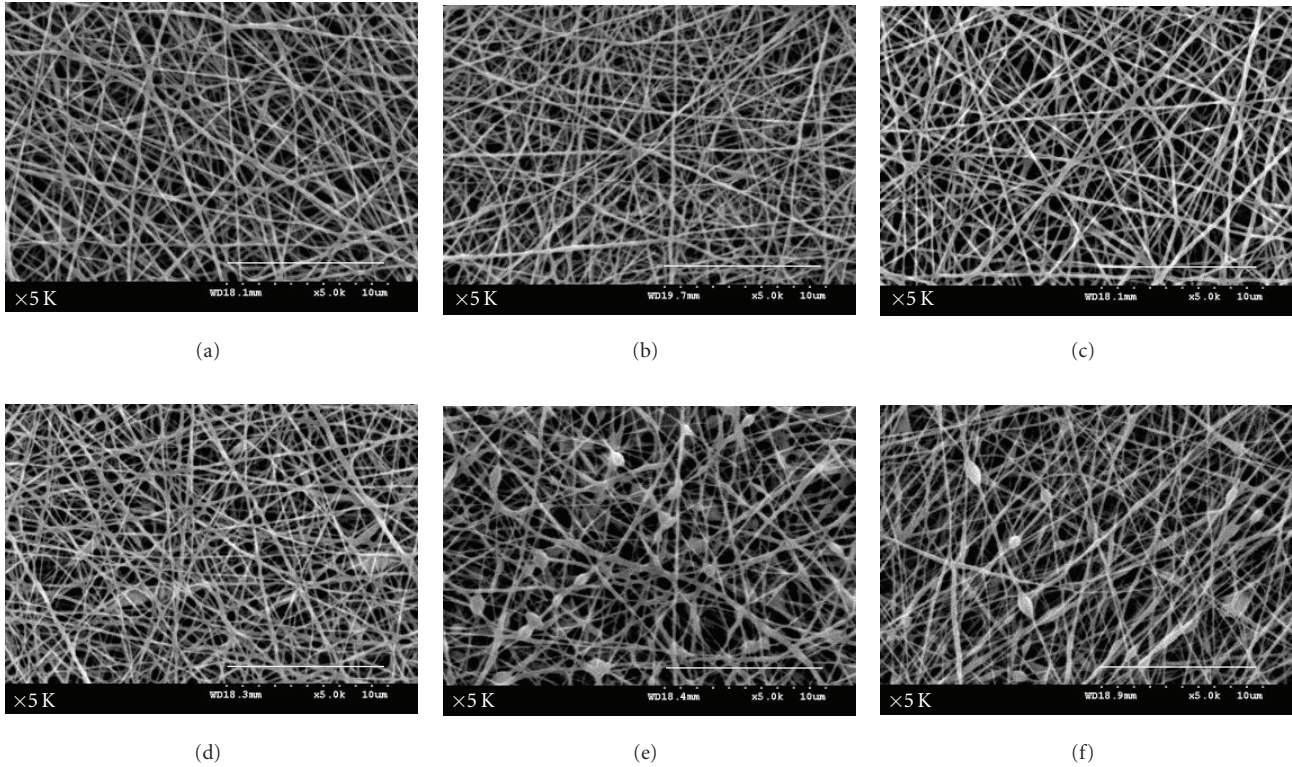


FIGURE 4: SEM images ($\times 5000$) of nano fibers made of PVA/BS solution with volume ratios of (a) pure PVA, (b) 9 : 1, (c) 8 : 2, (d) 7 : 3, (e) 6 : 4, and (f) 5 : 5, by electrospinning. Scale bar: 10 μm .

content also decreased the viscosity of PVA/BS solution. Pure BS solution possessed a low viscosity, the greater the amount of BS content, the lower the viscosity of PVA/BS solution. The viscosity of PVA/BS solution was proportional to the mean of fiber diameter, namely, the mean of fiber diameter decreased with a decrease in the viscosity of PVA/BS solution.

According to Figure 4, beads started to occur when BS content was 20%, indicating that the viscosity of PVA/BS solution was lower than the critical value of polymer viscosity required by electrospinning. In this study, the critical value of desired viscosity fell within 378.2~321.4 cp. The optimal volume ratio of PVA/BS solution was 9 : 1, with which the resulting fibers exhibited no beads, resulting in the optimal fiber formation.

3.3. SEM of the PVA/BS Nano Fibers Made by Various Electric Fields and Syringe Flows. Table 2 reports the effect of various electric fields and syringe flows on the mean of fiber diameter of the electrospun fibers made of PVA/BS solution of 9 : 1, which was obtained from Section 3.2. The electric field varied from 0.6, 0.8, 1.0, 1.2 to 1.4 kV/cm while the syringe flow varied from 0.50, 0.75 to 1.00 mL/h. According to Table 2, five combinations of electric fields and syringe flows, which created a smaller mean of fiber diameter, were selected. Figure 5 shows the SEM images of the resulting PVA/BS fibers with the chosen five combinations

TABLE 2: Mean of fiber diameter as related to various electric fields and syringe flows.

Electric field (kV/cm)	Syringe flow (mL/h)	Mean of fiber diameter (Nm)
0.6	0.50	206 \pm 46
0.8	0.50	170 \pm 29
1.0	0.50	222 \pm 34
1.2	0.50	247 \pm 39
1.4	0.50	186 \pm 35
0.6	0.75	195 \pm 30
0.8	0.75	249 \pm 43
1.0	0.75	179 \pm 28
1.2	0.75	239 \pm 40
1.4	0.75	220 \pm 36
0.6	1.00	193 \pm 37
0.8	1.00	192 \pm 41
1.0	1.00	227 \pm 38
1.2	1.00	243 \pm 36
1.4	1.00	199 \pm 45

of 0.6 kV/cm-1.0 mL/h, 0.8 kV/cm-0.5 mL/h, 0.8 kV/cm-1.00 mL/h, 1 kV/cm-0.75 mL/h, and 1.4 kV/cm-0.5 mL/h. There was variation in the mean of fiber diameter because

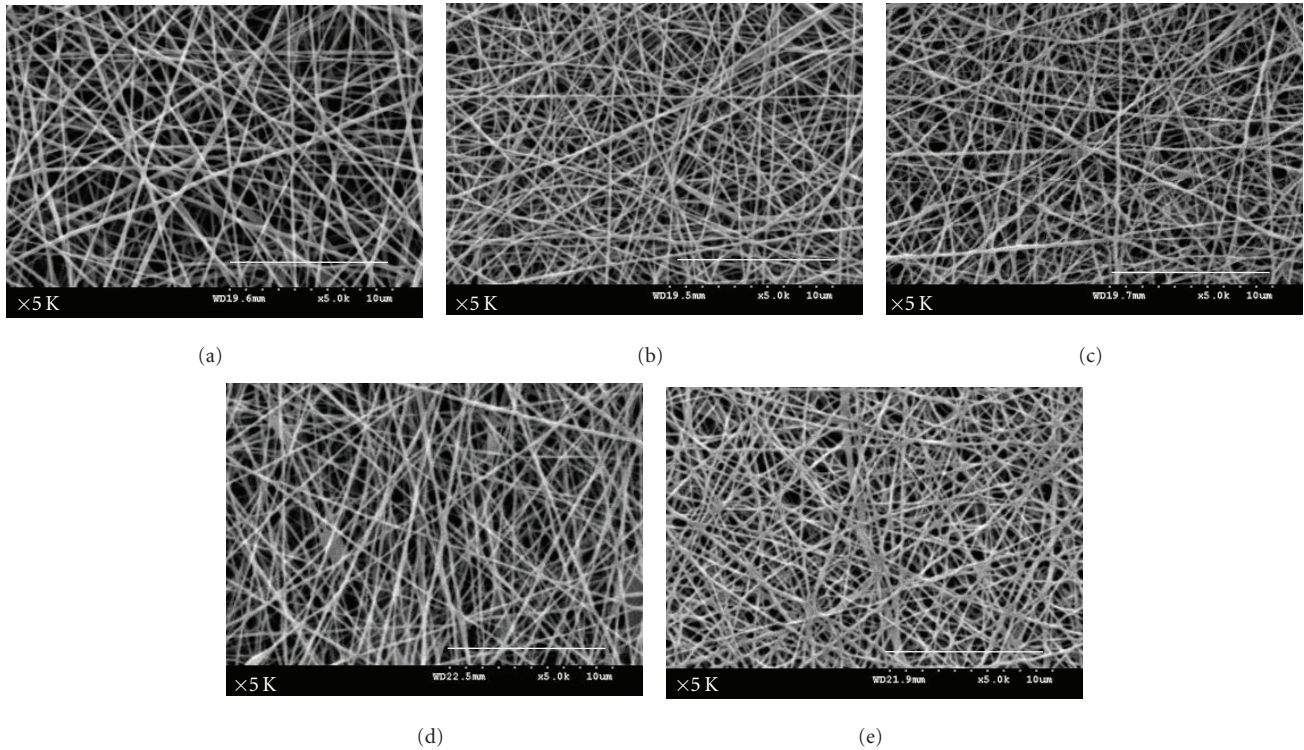


FIGURE 5: SEM images ($\times 5000$) of electrospun fibers made of PVA/BS solution (9:1) with various combinations of electric field and syringe flow of (a) 0.6 kV/cm-1.0 mL/h, (b) 0.8 kV/cm-0.5 mL/h, (c) 0.8 kV/cm-1.00 mL/h, (d) 1 kV/cm-0.75 mL/h, and (e) 1.4 kV/cm-0.5 mL/h. Scale bar: 10 μm .

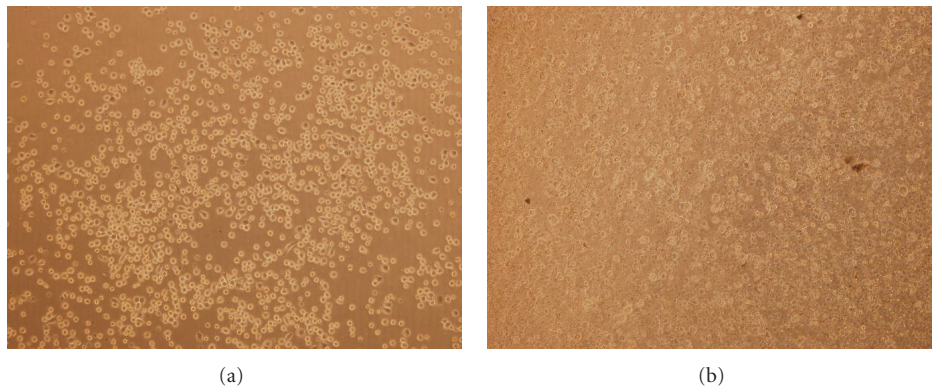


FIGURE 6: Optical microscope images of cell growth of (a) control group (pure L929 fibroblasts cultured in medium), and (b) L929 fibroblasts cultured with a PVA/BS nanomembrane in medium.

when the charge was varied, the polymer solution was turned into different shapes, called Taylor cones, on the tip of the syringe as a result of an imbalance of surface tension of polymer solution (repulsion force) and electric field force (pulling force). This influenced the generated drops, fiber diameter, fiber morphology, and the strength of currents.

With the five given combinations of electric fields and syringe flows, the resulting Taylor cones did not create beads, showing that these Taylor cones, formed during electrospinning, were all suitable for fiber formation. In addition, variation in electric fields generated currents with various strengths during currents' transmission in polymer

solution, forming PVA/BS nano fibers with various diameters. The optimal combination was thus determined to be an electric field of 0.8 kV/cm and a syringe flow of 0.5 mL/h, which produced the smallest mean of fiber diameter (170 ± 29 nm); the amount of fibers was also greater than the other groups.

3.4. Cell Biocompatibility Test. Figure 6 shows the images of cell growth magnified 40 times: (a) is the control group (pure L929 fibroblasts cultured in medium), and (b) is L929 fibroblasts cultured with a PVA/BS nanomembrane in medium. Comparing Figures 6(a) and 6(b), the cell amount did not

TABLE 3: Comparison of mechanical properties of PVA/BS composite dressings and PET/AC matrices.

	PVA/BS composite dressings		PET/AC matrices	
	CD	MD	CD	MD
Maximum tear strength (N)	106.7	79.8	103.6	76
Standard deviation	5.32	2.88	4.4	1.62
Maximum tensile strength (N)	130.7	38.1	123.9	36.8
Standard deviation	6.71	0.49	4.71	2.44
Flexibility (cm)	12.2	10.9	8.5	7.1
Standard deviation	0.65	0.45	0.16	0.33

TABLE 4: Comparison of air permeability of PVA/BS composite dressings and PET/AC matrices.

	PVA/BS composite dressings	PET/AC matrices
Air permeability (cm ³ /s/cm ²)	57.4	106.05
Standard deviation	9.39	4.55

decrease largely when cells were cultured with a PVA/BS nanomembrane, indicating the resulting nanomembrane did not negatively interfere with cell growth. In other words, PVA/BS nanomembranes had a minor toxicity, resulting in only a minor cell loss after implantation of the nanomembranes.

3.5. Mechanical Properties of PVA/BS Composite Dressings and PET/AC Matrices. Tables 3 and 4 compare the tear strength, tensile strength, flexibility, and air permeability of PVA/BS composite dressings and PET/AC matrices. According to Table 3, after PVA/BS solution was electrospun to PET/AC matrices, the resulting composite dressings displayed greater mechanical properties. This was because electrospinning transformed the solution into a nanofibrous net, the nano fibers of which had a smaller diameter than that of PET/AC fibers. The nano fibers fell in and then filled the voids of PET/AC matrices. In addition, nano fibers also had a larger specific surface area, enlarging the contact area between the PVA/BS nano fibers and PET/AC fibers and, thus, raising the friction between fibers. An increase in friction contributed to a greater resistance for fibers to move. Therefore, to electrospin PVA/BS solution onto the PET/AC matrices indirectly imparted greater mechanical properties to the resulting PVA/BS composite dressings.

In contrast, the air permeability of the resulting PVA/BS composite dressings was lower than that of PET/AC matrices. Due to the aforementioned explanation about the distribution of nano fibers during electrospinning, the voids in PET/AC matrices were clogged by nano fibers, decreasing the air volume that passed through the voids per unit time, and the air permeability. However, the air permeability of PVA/BS composite dressings was still satisfactory.

4. Conclusion

This study proposed a PVA/BS composite dressing, which was made by electrospinning the PVA/BS solution onto the PET/AC matrices. The fiber formation and physical properties of the resulting materials as related to various parameters were explored. When PVA/BS solution had a volume ratio of 9 : 1, the critical value of the solution viscosity fell between 378.2~321.4 cp, creating no beads between the resulting PVA/BS nano fibers and thus providing the optimal fiber formation. With a constant volume ratio of 9 : 1, PVA/BS solution could be electrospun into nano fibers with the smallest mean of fiber diameter (170 ± 29 nm) when the electric field was 0.8 kV/cm and the syringe flow was 0.5 mL/h. In the cell biocompatibility test, PVA/BS nanomembranes had minor toxicity, which caused only insignificant cell loss. In comparison with PET/AC matrices, PVA/BS composite dressings were composed of nano fibers, which had a much smaller diameter and high specific surface area, and thus exhibited greater tensile and tear strength, flexibility, and a lower air permeability.

Acknowledgment

The authors are thankful to the National Science Council, Taiwan, ROC, for providing financial assistance to carry out this research work under NSC-97-2622-E-166-003-CC3.

References

- [1] N. S. Levine, R. A. Lindberg, R. E. Salisbury, A. D. Mason Jr., and B. A. Pruitt Jr., "Comparison of coarse mesh gauze with biologic dressings on granulating wounds," *American Journal of Surgery*, vol. 131, no. 6, pp. 727–729, 1976.
- [2] G. Linda and M. Phillips, "Wound healing," in *Sabiston Textbook of Surgery*, 16th edition.
- [3] M. Malmjö, R. Ingemansson, R. Martin, and E. Huddleston, "Negative-pressure wound therapy using gauze or open-cell polyurethane foam: similar early effects on pressure transduction and tissue contraction in an experimental porcine wound model," *Wound Repair and Regeneration*, vol. 17, no. 2, pp. 200–205, 2009.
- [4] M. McGuckin, R. Goldman, L. Bolton, and R. Salcido, "The clinical relevance of microbiology in acute and chronic wounds," *Advances in Skin & Wound Care*, vol. 16, no. 1, pp. 12–23, 2003.
- [5] M. J. Morykwas, L. C. Argenta, E. I. Shelton-Brown, and W. McGuirt, "Vacuum-assisted closure: a new method for wound control and treatment: animal studies and basic foundation," *Annals of Plastic Surgery*, vol. 38, no. 6, pp. 553–562, 1997.
- [6] M. J. Morykwas, L. C. Argenta, E. I. Shelton-Brown, and W. McGuirt, "Vacuum-assisted closure: a new method for wound control and treatment: animal studies and basic foundation," *Annals of Plastic Surgery*, vol. 38, no. 6, pp. 563–577, 1997.
- [7] M. J. Morykwas and L. C. Argenta, "Nonsurgical modalities to enhance healing and care of soft tissue wounds," *Journal of the Southern Orthopaedic Association*, vol. 6, no. 4, pp. 279–288, 1997.
- [8] T. A. Mustoe, "Evolution of silicone therapy and mechanism of action in scar management," *Aesthetic Plastic Surgery*, vol. 32, no. 1, pp. 82–92, 2008.

- [9] J. Zeleny, "The electrical discharge from liquid points and a hydrostatic method of measuring the electric intensity at their surface," *Physical Review*, vol. 3, no. 2, pp. 69–91, 1914.
- [10] A. Formhals, "Process and Apparatus for Preparing Artificial Threads," US Patent, 1, 975, 504, 1934.
- [11] A. Formhals, "Method and Apparatus for Spinning," US Patent, 2, 160, 962, 1939.
- [12] A. Formhals, "Artificial Thread and Method of Producing Same," US Patent, 2, 187, 306, 1940.
- [13] S. Y. Gu, J. Ren, and G. J. Vancso, "Process optimization and empirical modeling for electrospun polyacrylonitrile (PAN) nanofiber precursor of carbon nanofibers," *European Polymer Journal*, vol. 41, no. 11, pp. 2559–2568, 2005.
- [14] K. T. Shalumon, N. S. Binulal, N. Selvamurugan et al., "Electrospinning of carboxymethyl chitin/poly(vinyl alcohol) nanofibrous scaffolds for tissue engineering applications," *Carbohydrate Polymers*, vol. 77, no. 4, pp. 863–869, 2009.
- [15] Y. T. Jia, J. Gong, X. H. Gu, H. Y. Kim, J. Dong, and X. Y. Shen, "Fabrication and characterization of poly (vinyl alcohol)/chitosan blend nanofibers produced by electrospinning method," *Carbohydrate Polymers*, vol. 67, no. 3, pp. 403–409, 2007.
- [16] N. Charernsriwilaiwat, P. Opanasopit, T. Rojanarata, T. Ngawhirunpat, and P. Supaphol, "Preparation and characterization of chitosan-hydroxybenzotriazole/polyvinyl alcohol blend nanofibers by the electrospinning technique," *Carbohydrate Polymers*, vol. 81, no. 3, pp. 675–680, 2010.
- [17] S. E. Shih, *Textile Physics*, Taiwan Textile Research Institute, Taipei, Taiwan, 2000.
- [18] C. A. Lin, "Fiber Chemistry," Taiwan Silk & Filament Weaving Industrial Information Web, 2006.
- [19] H. Diao, X. Li, J. Chen et al., "Bletilla striata polysaccharide stimulates inducible nitric oxide synthase and proinflammatory cytokine expression in macrophages," *Journal of Bioscience and Bioengineering*, vol. 105, no. 2, pp. 85–89, 2008.
- [20] X. Miao, *Shenmong Ben Cao Jing Su*, China Press of Traditional Chinese Medicine, Beijing, China, 1997.
- [21] Shi-zhen Li, *Pen Ts'ao Kang Mu*, China Press of Traditional Chinese Medicine, Beijing, China, 1998.
- [22] A. Wang, *Pen Ts'ao Pei Yao*, China Press of Traditional Chinese Medicine, Beijing, China, 1998.
- [23] C. W. Lou, J. J. Hu, C. C. Huang, C. T. Lu, C. T. Hsieh, and J. H. Lin, "Preparation and characterization of polyester fibers/absorbent cotton composite dressing matrix fabrics," *Advanced Materials Research*, vol. 287–290, pp. 2721–2724, 2011.
- [24] N. K. Adam, "Use of the term "Young's Equation" for contact angles," *Nature*, vol. 180, no. 4590, pp. 809–810, 1957.

Research Article

Sonochemical Synthesis of Er³⁺-Doped ZnO Nanospheres with Enhanced Upconversion Photoluminescence

Jun Geng,^{1,2} Guang-Hui Song,¹ and Jun-Jie Zhu¹

¹ State Key Laboratory of Analytical Chemistry for Life Science, School of Chemistry and Chemical Engineering, Nanjing University, Nanjing 210093, China

² Department of Chemistry, Jiangsu Institute of Education, Nanjing 210013, China

Correspondence should be addressed to Jun-Jie Zhu, jjzhu@nju.edu.cn

Received 24 September 2012; Accepted 8 October 2012

Academic Editor: Xiao-Miao Feng

Copyright © 2012 Jun Geng et al. This is an open access article distributed under the Creative Commons Attribution License, which permits unrestricted use, distribution, and reproduction in any medium, provided the original work is properly cited.

Er³⁺-doped ZnO nanospheres have been synthesized via a sonochemical conversion process. The formation mechanism of these nanocrystals is connected with the sonochemical effect of ultrasound irradiation. The as-prepared Er³⁺ doped ZnO nanospheres show enhanced photoluminescence and upconversion photoluminescence properties compared with pure ZnO.

1. Introduction

ZnO semiconductors, with a direct wide bandgap of 3.37 eV and aesthetic nanoscale morphologies, have been intensively studied due to their multifunctional characteristics for a diverse range of applications in optical, electronic, optoelectronic, piezoelectric, photocatalytic, and power devices [1]. In the past decade, ZnO has been explored for new device applications when extra functionalities are intentionally introduced through proper doping or alloying with impurity ions despite the considerable challenges. It is worth noting that much effort has also been made through doping rare earth (RE) ions (e.g., Er³⁺ and Eu³⁺) into the ZnO host, which undergoes upconversion (UC) luminescence and/or energy transfer, in realizing new optoelectronic and photonic device applications such as solid-state full-colour displays, infrared detectors, solar cells, biological fluorescent labels, and all-solid compact lasers [2]. The Er³⁺-doped semiconductors are the potential optoelectronic materials [3] due to the Er intra-4f shell transition with a photoemission at a wavelength of 1.54 μm , which lies in the minimum loss region of silica-based optical fibers [4].

Up to now, physical doping methods such as ion implantation [5], laser ablation [6], magnetron sputtering [7], and high temperature calcinations [8] have mainly been used to introduce Er into ZnO substrate, while most

researches focused on the formation of films. Some chemical doping methods, such as sol-gel [9], colloidal [10], and hydrothermal processes [11], have also been reported to prepare Er³⁺-doped ZnO nanocrystals. However, most products were nanoparticles. Only a few groups reported the morphology-controlled synthesis, such as Er³⁺-doped ZnO nanowires fabricated using Er-ion implantation [5], flower-like structures prepared by a wet chemical reaction [12], and prickly sphere-like, column-like, prism-like, and grain-like structures prepared via hydrothermal process [13]. Therefore, it is still a challenge to prepare Er³⁺-doped nanocrystals with special morphology through a fast and convenient method.

Here, a facile sonochemical route has been used to prepare Er³⁺-doped ZnO nanospheres. Under the irradiation of ultrasound, it only took 30 min of reaction time to effectively dope Er³⁺ into ZnO host. The photoluminescence and upconversion photoluminescence properties of the as-prepared Er³⁺-doped ZnO nanospheres were investigated, and the results showed enhanced emission due to effective doping.

2. Experimental

2.1. Materials. All the reagents used were of analytical purity and were used without further purification.

$\text{Zn}(\text{NO}_3)_2 \cdot 6\text{H}_2\text{O}$, $\text{Er}(\text{NO}_3)_3 \cdot 5\text{H}_2\text{O}$, PEG-20000, and triethanolamine (TEA) were purchased from Beijing Chemical Reagents Ltd. Co. of China.

2.2. Synthesis. Typically, $\text{Zn}(\text{NO}_3)_2 \cdot 6\text{H}_2\text{O}$ (0.005 mol) was dissolved in H_2O (100 mL), and then specific amount of $\text{Er}(\text{NO}_3)_3 \cdot 5\text{H}_2\text{O}$ (2, 5, 10% doping, resp.), PEG-20000 (1 g) and TEA (2 mL) were introduced sequentially with stirring to form a clear solution. The transparent mixture solution was exposed to high-intensity ultrasound irradiation under ambient air for 30 min. Ultrasound irradiation was generated with a high-intensity ultrasonic probe (Xinzhi Co., China, JY92-2D, 0.6 cm diameter; Ti-horn, 20 kHz, 60 W cm^{-2}) immersed directly in the reaction solution. A white precipitate was centrifuged, washed with distilled water and absolute ethanol in sequence, and finally dried in air. The final products were collected for characterizations and further preparations.

2.3. Characterization. The X-ray powder diffraction (XRD) analysis was performed on a Philips X²-pert X-ray diffractometer at a scanning rate of 4° min^{-1} in the 2θ range from 10° to 80° , with graphite-monochromatized $\text{Cu-K}\alpha$ radiation ($\lambda = 0.15418 \text{ nm}$). The scanning electron micrographs (SEM) were taken on a LEO-1530VP field-emission scanning electron microscope. Transmission electron microscopy (TEM) was carried out on a JEOLJEM 200CX transmission electron microscope, using an accelerating voltage of 200 kV. High-resolution transmission electron micrographs (HRTEM) were obtained by employing a JEOL-2010 high-resolution transmission electron microscope with an accelerating voltage of 200 kV. Photoluminescence spectra (PL) were measured on a Shimadzu RF-5301PC fluorescence spectrometer under the excitation of 325 nm at room temperature. The upconversion (UC) photoluminescence spectra were recorded on a spectrometer (Zolix, China) equipped with a 980 nm laser diode as the excitation source.

3. Results and Discussion

3.1. Characterization of the Final Products. Figure 1 shows the XRD pattern of the as-prepared products. Evidently, all of the diffraction peaks in the XRD pattern are well assigned to hexagonal wurtzite ZnO as reported in JCPDS card no. 36-1451, and no impurity phase related to Er^{3+} could be found. The diffraction peaks shift to lower angle slightly with the Er-doping concentration increasing from 2–10%, indicating that the lattice parameter gets larger when Er^{3+} are incorporated into ZnO lattice, which is consistent with the fact that the radii of Er^{3+} ($R = 0.89 \text{ \AA}$) are bigger than that of Zn^{2+} ($R = 0.74 \text{ \AA}$).

The as-prepared Er^{3+} -doped ZnO samples appeared as uniform solid nanospheres with diameter of ca. 400 nm, as shown in Figures 2(a) and 2(b). The HRTEM image recorded on the surface of ZnO:Er nanospheres (Figure 2(c)) shows lattice fringes with interplanar spacing of 0.25 nm for the (101) faces of hexagonal ZnO.

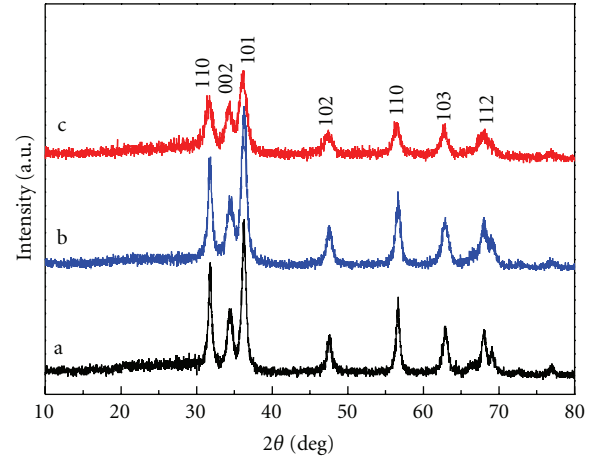


FIGURE 1: XRD patterns of Er^{3+} -doped ZnO nanocrystals with Er doping concentrations of (a) 2%, (b) 5%, and (c) 10%.

3.2. Possible Sonochemical Formation Mechanism. In recent years, ultrasonic irradiation has been extensively used in the synthesis of nanomaterials. The effects of high-intensity ultrasound result primarily from acoustic cavitation are [14]: the formation, growth, and implosive collapse of bubbles in liquids. During the acoustic cavitation process, very high temperatures ($>5000 \text{ K}$), pressures ($>20 \text{ MPa}$), and cooling rates ($>10^{10} \text{ K s}^{-1}$) can be achieved upon the collapse of the bubble, which provides a unique platform for the growth of nanostructures including 0D nanoparticles [15], 1D nanorods [16], to 2D nanoplates [17], and even mesoporous [18] or hollow structures [19]. Nanocomposites [20] and doped nanomaterials [21] have also been prepared through sonochemical methods.

In the present case, $\text{Zn}(\text{NO}_3)_2 \cdot 6\text{H}_2\text{O}$ was used as precursor, TEA as complexing and precipitating agent and PEG as capping agent. TEA has the chemical formula $\text{N}(\text{CH}_2\text{CH}_2\text{OH})_3$, which acts generally as a weak base due to the single lone pair of electrons on nitrogen atom and accordingly could coordinate to zinc ions forming $[\text{Zn}(\text{TEA})_4]^{2+}$ complex [22]. Under ultrasonic irradiation, the complex would dissociate and a part of TEA molecules would hydrolyze to build up an alkaline environment, which leads to the controlled release of free zinc ions and hydroxide ions ((1) and (2)). The released Zn^{2+} ion and OH^- ion would combine and transform to ZnO under sonochemical conditions ((3) and (4)). As a popular shape modifier, PEG was used here to control the morphology of formed ZnO nanoparticles and also showed effective role to make uniform ZnO nanospheres. Therefore, the mechanism of the formation of ZnO nanospheres is probably related to the coordination of Zn^{2+} and TEA to form Zn-TEA complex, the dissociation of the complex under sonication and PEG-modified formation of ZnO nanospheres. The probable reaction process in aqueous solution can be summarized as follows:



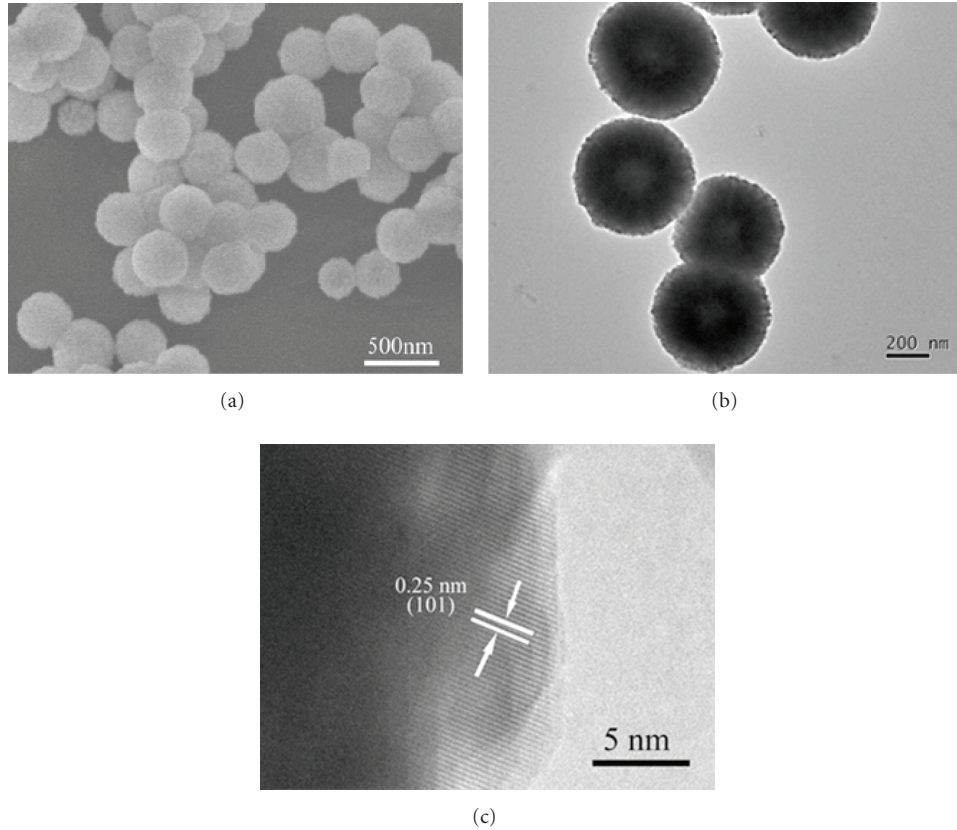
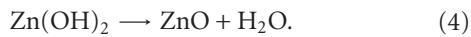


FIGURE 2: (a) SEM, (b) TEM, and (c) HRTEM images of the as-prepared Er^{3+} -doped ZnO nanospheres with Er doping concentration of 2%.



High-intensity ultrasonic irradiation also played an important role. The transient high temperature and high pressure field produced during ultrasonic irradiation provides a favorable environment for the growth of nanocrystals. Cavitations and shock waves created by ultrasound can accelerate solid particles to high velocities leading to inter-particle collisions and inducing effective fusion at the point of collision [23]. We consider that the high temperature, high pressure, and shock waves caused by ultrasound induced the effective doping of Er^{3+} into ZnO host. The energy generated during collision can induce the crystallization of the amorphous particles, responsible for the further crystallization process. It only took 30 min of reaction time to conduct effective doping under ultrasonic irradiation, while rather long reaction time (e.g., 8–12 hours) is needed in hydrothermal and other synthetic routes.

3.3. Photoluminescence Properties. Figure 3 shows the room-temperature photoluminescence spectra of pure and Er^{3+} -doped ZnO with different Er^{3+} doping concentrations using the same excitation line at 325 nm. All samples show a strong and broad green emission around 540 nm which can be

attributed to deep-level emission (DLE) caused by defects and impurities [24]. The emission intensity of ZnO:Er is increased enormously as compared with that of undoped ZnO. The integral emission intensity of ZnO:Er with 10% Er^{3+} doping concentration is 3 times higher than that of the undoped ZnO, which indicates an unusual improvement on the light yield by Er doping.

The PL spectra of the ZnO:Er crystal with Er^{3+} doping concentration varying from 2% to 10% (Figures 3(b)–3(d)) show that the emission intensity enhanced with the increasing doping concentration. The heavily doped product appeared to have an extremely high PL intensity in the present case, which might be related to the interaction between ZnO and Er. Previous studies reported that the intentionally doped impurities could provide a significant contribution to DLE, for example, by providing donor-acceptor pairs in ZnO [24]. The majority of Er in ZnO is likely to be associated with rare earths occupying substitutional Zn sites [25], and the local lattice is modified because of the different oxidation states and ionic sizes of Er and Zn ions [26]. The incorporation of Er ions in the ZnO lattice is therefore expected to increase the deep-level states and resulted in an increase in DLE. Energy transfer might also occur between excitons and Er^{3+} ions [27]; however, we did not observe Er^{3+} emission peaks in the visible region. It might be possible that the weak emission peaks of Er^{3+} ions were embedded in the trace of a strong DLE.

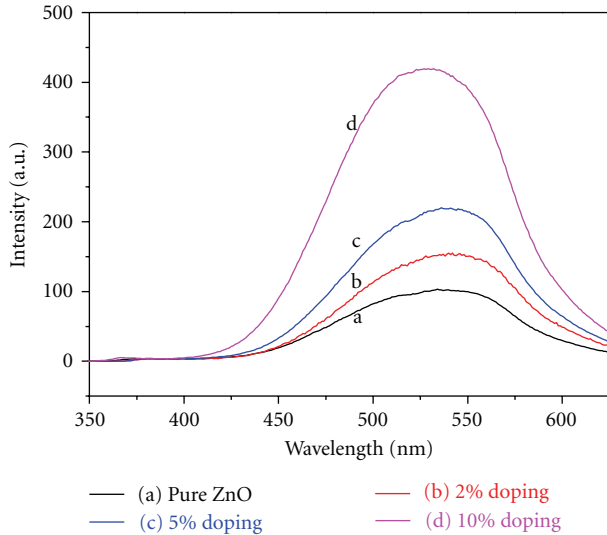


FIGURE 3: The PL spectra of (a) the pure ZnO and Er^{3+} -doped ZnO nanospheres with different Er doping concentrations of (b) 2%, (c) 5%, and (d) 10%.

3.4. Upconversion Luminescence Properties. Upon excitation with a 980 nm semiconductor laser diodes (SLD) at room temperature, the blue, green, and red upconversion emissions of Er^{3+} ions in the ZnO nanocrystals were observed, which suggests that the Er^{3+} ions have been incorporated inside the crystalline ZnO grains. The upconversion luminescence spectra for the pure ZnO and Er^{3+} -doped ZnO nanospheres with different Er doping concentrations are shown in Figure 4, where four emission bands at approximately 409 nm, 525, 545, and 659 nm are assigned to $2\text{H}_{9/2}$ to $4\text{I}_{15/2}$, $2\text{H}_{11/2}$ to $4\text{I}_{15/2}$, $4\text{S}_{3/2}$ to $4\text{I}_{15/2}$, and $4\text{F}_{9/2}$ to $4\text{I}_{15/2}$ transitions, respectively [2].

Obviously, the upconversion luminescence intensity of Er^{3+} -doped ZnO is much higher than that of pure ZnO, which indicate the effective doping could enhance the upconversion emission. It is found that with the Er doping concentration increasing from 2% to 5%, the integral upconversion luminescence intensity enhanced. However, with the Er-doping concentration varying from 5% to 10%, the green emission decreased slightly while the red emission enhanced, which is similar with the literature [28]. Therefore, the upconversion light output could be tuned by adjusting the dopant concentration. Further detailed investigation is still going on.

4. Conclusion

Er^{3+} -doped ZnO nanospheres have been synthesized via a facile sonochemical route. Ultrasonic irradiation played an important role in the formation of ZnO nanospheres and resulted in the effective doping. The photoluminescence intensity of Er^{3+} -doped nanocrystals enhanced with the increasing Er doping concentrations. Higher upconversion photoluminescence emissions of the Er^{3+} -doped ZnO

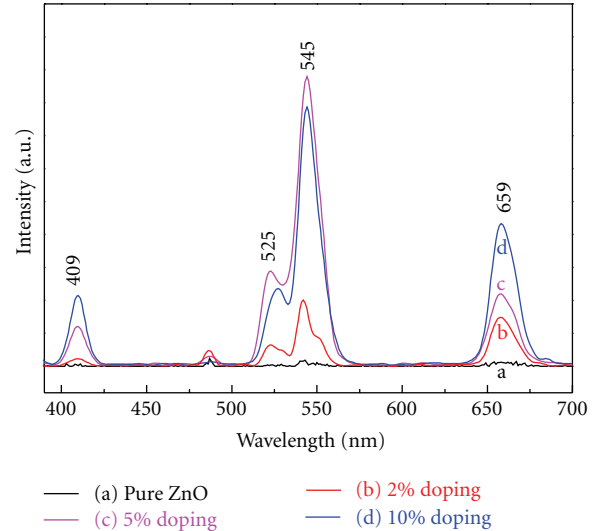


FIGURE 4: Upconversion spectra of (a) the pure ZnO and Er^{3+} -doped ZnO nanospheres with different doping concentrations of (b) 2%, (c) 5%, and (d) 10% excited by 980 nm laser at room temperature.

nanocrystals were observed, which suggests that the Er^{3+} ions have been incorporated inside the crystalline ZnO grains.

Acknowledgments

This work is supported by the Young Scientists Fund of the National Natural Science Foundation of China (Grant no. 20805022), National Natural Science Foundation of China (Grant no. 50972058), and China Postdoctoral Science Foundation (Grant no. 20100471294).

References

- [1] Z. L. Wang and J. Song, "Piezoelectric nanogenerators based on zinc oxide nanowire arrays," *Science*, vol. 312, no. 5771, pp. 243–246, 2006.
- [2] X. Wang, X. Kong, G. Shan et al., "Luminescence spectroscopy and visible upconversion properties of Er^{3+} in ZnO nanocrystals," *Journal of Physical Chemistry B*, vol. 108, no. 48, pp. 18408–18413, 2004.
- [3] Y. Bai, Y. Wang, K. Yang et al., "The effect of Li on the spectrum of Er^{3+} in Li- and Er-codoped ZnO nanocrystals," *Journal of Physical Chemistry C*, vol. 112, no. 32, pp. 12259–12263, 2008.
- [4] X. Zhao, S. Komuro, H. Isshiki, Y. Aoyagi, and T. Sugano, "Fabrication and stimulated emission of Er-doped nanocrystalline Si waveguides formed on Si substrates by laser ablation," *Applied Physics Letters*, vol. 74, no. 1, pp. 120–122, 1999.
- [5] K. Zhong, J. Xu, J. Su, and Y. L. Chen, "Upconversion luminescence from Er-N codoped of ZnO nanowires prepared by ion implantation method," *Applied Surface Science*, vol. 257, no. 8, pp. 3495–3498, 2011.
- [6] S. Harako, S. Yokoyama, K. Ide, X. Zhao, and S. Komoro, "Visible and infrared electroluminescence from an Er-doped n-ZnO/p-Si light emitting diode," *Physica Status Solidi A*, vol. 205, no. 1, pp. 19–22, 2008.

- [7] Y. Chen, X. L. Xu, G. H. Zhang, H. Xue, and S. Y. Ma, "Blue shift of optical band gap in Er-doped ZnO thin films deposited by direct current reactive magnetron sputtering technique," *Physica E*, vol. 42, no. 5, pp. 1713–1716, 2010.
- [8] Z. Zhou, T. Komori, T. Ayukawa et al., "Li- and Er-codoped ZnO with enhanced 1.54 μm photoemission," *Applied Physics Letters*, vol. 87, no. 9, Article ID 091109, 3 pages, 2005.
- [9] X. Meng, C. Liu, F. Wu, and J. Li, "Strong up-conversion emissions in ZnO:Er³⁺, ZnO:Er³⁺-Yb³⁺ nanoparticles and their surface modified counterparts," *Journal of Colloid and Interface Science*, vol. 358, no. 2, pp. 334–337, 2011.
- [10] M. Kohls, T. Schmidt, H. Katschorek et al., "Simple colloidal route to planar micropatterned ErZnO amplifiers," *Advanced Materials*, vol. 11, no. 4, pp. 288–292, 1999.
- [11] C.-Y. Chen, K.-Y. Lai, J.-W. Lo et al., "Electronic structures of well-aligned Er-doped ZnO nanorod arrays," *Journal of Nanoscience and Nanotechnology*, vol. 11, no. 12, pp. 10615–10619, 2011.
- [12] W. C. Yang, C. W. Wang, J. H. He et al., "Facile synthesis of large scale Er-doped ZnO flower-like structures with enhanced 1.54 μm infrared emission," *Physica Status Solidi A*, vol. 205, no. 5, pp. 1190–1195, 2008.
- [13] Y. Sun, Y. Chen, L. Tian et al., "Morphology-dependent upconversion luminescence of ZnO:Er³⁺ nanocrystals," *Journal of Luminescence*, vol. 128, no. 1, pp. 15–21, 2008.
- [14] K. S. Suslick, S. B. Choe, A. A. Cichowlas, and M. W. Grinstaff, "Sonochemical synthesis of amorphous iron," *Nature*, vol. 353, no. 6343, pp. 414–416, 1991.
- [15] A. Nemancha, J. L. Rehspringer, and D. Khatmi, "Synthesis of palladium nanoparticles by sonochemical reduction of palladium(II) nitrate in aqueous solution," *Journal of Physical Chemistry B*, vol. 110, no. 1, pp. 383–387, 2006.
- [16] J. Geng, W. H. Hou, Y. N. Lv, J. J. Zhu, and H. Y. Chen, "One-dimensional BiPO₄ nanorods and two-dimensional BiOCl lamellae: fast low-temperature sonochemical synthesis, characterization, and growth mechanism," *Inorganic Chemistry*, vol. 44, no. 23, pp. 8503–8509, 2005.
- [17] L. P. Jiang, S. Xu, J. M. Zhu, J. R. Zhang, J. J. Zhu, and H. Y. Chen, "Ultrasonic-assisted synthesis of monodisperse single-crystalline silver nanoplates and gold nanorings," *Inorganic Chemistry*, vol. 43, no. 19, pp. 5877–5883, 2004.
- [18] R. K. Rana, Y. Mastai, and A. Gedanken, "Acoustic cavitation leading to the morphosynthesis of mesoporous silica vesicles," *Advanced Materials*, vol. 14, no. 19, pp. 1414–1418, 2002.
- [19] J. Geng, J. J. Zhu, D. J. Lu, and H. Y. Chen, "Hollow PbWO₄ nanospindles via a facile sonochemical route," *Inorganic Chemistry*, vol. 45, no. 20, pp. 8403–8407, 2006.
- [20] J. Geng, X. D. Jia, and J. J. Zhu, "Sonochemical selective synthesis of ZnO/CdS core/shell nanostructures and their optical properties," *CrystEngComm*, vol. 13, no. 1, pp. 193–198, 2011.
- [21] J. Geng, D. Lu, J. J. Zhu, and H. Y. Chen, "Antimony(III)-doped PbWO₄ crystals with enhanced photoluminescence via a shape-controlled sonochemical route," *Journal of Physical Chemistry B*, vol. 110, no. 28, pp. 13777–13785, 2006.
- [22] Y. S. Fu, X. W. Du, J. Sun, Y. F. Song, and J. Liu, "Kinetics controlled growth of quasi-spherical ZnO single crystal in homogeneous solutions," *Journal of Alloys and Compounds*, vol. 461, no. 1-2, pp. 527–531, 2008.
- [23] S. J. Doktycz and K. S. Suslick, "Interparticle collisions driven by ultrasound," *Science*, vol. 247, no. 4946, pp. 1067–1069, 1990.
- [24] N. Y. Garces, L. Wang, L. Bai, N. C. Giles, L. E. Halliburton, and G. Cantwell, "Role of copper in the green luminescence from ZnO crystals," *Applied Physics Letters*, vol. 81, no. 4, pp. 622–624, 2002.
- [25] U. Wahl, E. Rita, J. G. Correia, E. Alves, and J. P. Araújo, "Implantation site of rare earths in single-crystalline ZnO," *Applied Physics Letters*, vol. 82, no. 8, pp. 1173–1175, 2003.
- [26] Z. Zhou, T. Komori, M. Yoshino et al., "Enhanced 1.54 μm photoluminescence from Er-containing ZnO through nitrogen doping," *Applied Physics Letters*, vol. 86, no. 4, Article ID 041107, 3 pages, 2005.
- [27] S. Komuro, T. Katsumata, T. Morikawa, X. Zhao, H. Isshiki, and Y. Aoyagi, "Highly erbium-doped zinc-oxide thin film prepared by laser ablation and its 1.54 μm emission dynamics," *Journal of Applied Physics*, vol. 88, no. 12, pp. 7129–7136, 2000.
- [28] Y. Liu, C. Xu, and Q. Yang, "White upconversion of rare-earth doped ZnO nanocrystals and its dependence on size of crystal particles and content of Yb³⁺ and Tm³⁺," *Journal of Applied Physics*, vol. 105, no. 8, Article ID 084701, 6 pages, 2009.

Research Article

Facile Synthesis of Calcium Carbonate Nanoparticles from Cockle Shells

Kh. Nurul Islam,¹ A. B. Z. Zuki,^{1,2} M. E. Ali,³ Mohd Zobir Bin Hussein,⁴ M. M. Noordin,⁵ M. Y. Loqman,⁶ H. Wahid,⁴ M. A. Hakim,⁷ and Sharifa Bee Abd Hamid³

¹Laboratory of Histology, Department of Preclinical Sciences, Faculty of Veterinary Medicine, Universiti Putra Malaysia, Selangor, 43400 Serdang, Malaysia

²Institute of Bioscience, University Putra Malaysia, Selangor, 43400 Serdang, Malaysia

³Nanotechnology and Catalysis Research Center, University of Malaya, 50603 Kuala Lumpur, Malaysia

⁴Laboratory of Nanomaterials, Department of Chemistry, Faculty of Science, Universiti Putra Malaysia, Selangor, 43400 Serdang, Malaysia

⁵Laboratory of Pathology, Department of Veterinary Pathology and Microbiology, Faculty of Veterinary Medicine, Universiti Putra Malaysia, Selangor, 43400 Serdang, Malaysia

⁶Department of Clinical Veterinary Studies, Faculty of Veterinary Medicine, Universiti Putra Malaysia, Selangor, 43400 Serdang, Malaysia

⁷Institute of Tropical Agriculture, Universiti Putra Malaysia, Selangor, 43400 Serdang, Malaysia

Correspondence should be addressed to A. B. Z. Zuki, zuki@vet.upm.edu.my

Received 14 May 2012; Revised 13 July 2012; Accepted 5 August 2012

Academic Editor: Jiu-Ju Feng

Copyright © 2012 Kh. Nurul Islam et al. This is an open access article distributed under the Creative Commons Attribution License, which permits unrestricted use, distribution, and reproduction in any medium, provided the original work is properly cited.

A simple and low-cost method for the synthesis of calcium carbonate nanoparticles from cockle shells was described. Polymorphically, the synthesized nanoparticles were aragonites which are biocompatible and thus frequently used in the repair of fractured bone and development of advanced drug delivery systems, tissue scaffolds and anticarcinogenic drugs. The rod-shaped and pure aragonite particles of 30 ± 5 nm in diameter were reproducibly synthesized when micron-sized cockle shells powders were mechanically stirred for 90 min at room temperature in presence of a nontoxic and nonhazardous biomineralization catalyst, dodecyl dimethyl betaine (BS-12). The findings were verified using a combination of analytical techniques such as variable pressure scanning electron microscopy (VPSEM), transmission electron microscopy (TEM), Fourier transmission infrared spectroscopy (FT-IR), X-ray diffraction spectroscopy (XRD), and energy dispersive X-ray analyser (EDX). The reproducibility and low cost of the method suggested that it could be used in industry for the large scale synthesis of aragonite nanoparticles from cockle shells, a low cost and easily available natural resource.

1. Introduction

Calcium carbonate (CaCO_3), which is one of the most abundant minerals in nature, exists in three polymorphs: calcite, aragonite, and vaterite [1]. Among these three polymorphs, aragonite has got enormous research attention because of its biocompatible properties [2–5]. It is denser than calcite and can be integrated, resolved, and replaced by bone [4, 6]. Aragonite is also a potential biomaterial for the development

of anticancer drugs, advanced drug delivery systems [7], and scaffolds for bone repair and tissue engineering [4]. Because of the presence of many attractive and useful properties in aragonite polymorphs, enormous research attention has been paid in the development of methodology for the controlled and facile synthesis of aragonite nanoparticles (ANPs) with convenient sizes and shapes [2, 3, 5]. Two fundamental routes for the bottom up synthesise of ANPs are documented: (1) the solution route in which aqueous CaCl_2 and

$(\text{NH}_4)_2\text{CO}_3$ or CaCl_2 and Na_2CO_3 or $\text{Ca}(\text{NO}_3)_2$ and Na_2CO_3 [2, 3, 8–12] are combined in equimolar ratios through a double decomposition reaction and (2) the carbonation route in which CO_2 gas is bubbled through an aqueous slurry of $\text{Ca}(\text{OH})_2$ at a specified temperature in presence of organic substrates such as polyacrylamide [5]. However, none of these routes can produce pure aragonite nanoparticles of suitable sizes and shapes. They are often mixed with calcite [3] or calcite and vaterite [2] and thus may not be suitable for a specialized biomedical application. Although carbonation methods are viewed to be eco-environmentally friendly, they need stringent temperature control, purified raw materials, and laborious gas (CO_2 or mixture of CO_2 and N_2) bubbling steps which incur additional cost, time, and skills [5, 13]. These methods also add organic impurities to the final products [13].

The synthesis of ANPs from its natural reservoirs such as cockle shells or sea shells using a top-down approach is greatly promising. In our last report [4], we have shown that cockle shells and its powders are rich and naturally purified source of aragonite polymorphs of calcium carbonate. In this paper, we developed an easy-to-perform, environmentally friendly, and low-cost method that involved a simple mechanical stirring of cockle shell powder in presence of BS-12 as a biomineralization catalyst. The method synthesized the smallest size ANPs so far reported in literatures [2–5]. The beauty of the method was that it did not add any impurities to the final products but produced very small-sized rod-shaped ANPs in a reproducible fashion, a criteria which is strongly desired in industrial synthesis.

2. Experimental

Approximately 250 gm of cockle shells (*Anadara granosa*) were washed and scrubbed to remove dirt, boiled for 10 minutes and then cooled at room temperature. The shells were then washed thoroughly with distilled water and dried in an oven (Mettler UM500, Germany) for seven days at 50°C . The cockle shells were finely grounded using a blender (Blendor, HCB 550, USA). The powders were sieved using a stainless laboratory test sieve with an aperture size of $90\ \mu\text{m}$ (Endecott Ltd., London, England) to obtain micron-sized ($10\text{--}90\ \mu\text{m}$ in diameter) powders [4]. Dodecyl dimethyl betaine ($\text{RN}+(\text{CH}_3)_2\text{CH}_2\text{COO}-$)(BS-12) was obtained from Sigma-Aldrich (Steinheim, Germany). The water used was HPLC-grade of resistance $>18\ \text{M}\Omega$ obtained from a Milli-RO6 plus Milli-Q-Water System (Organex).

For the synthesis of calcium carbonate nanoparticles, 5 grams of micron-sized cockle shells powders were taken into two separate 250-mL conical flasks. To each of the conical flasks, 50 mL distilled water was added to form a slurry. Two millilitres of BS-12 (as obtained from Sigma-Aldrich) was added into the second flask. The sample of the first conical flask was used as a control. After the addition of BS-12, the mixtures were vigorously stirred for 90 min at room temperature using a mechanical hot plate stirrer at the rate of 1000 rpm. The obtained samples were separated from the mother liquid using a double ring filter paper of size 18.0 cm (Filtres Fioroni, China). The final products were dried for 1

day in an oven (Mettler UM500) at 100°C and packed in a polyethylene plastic bag (JP Packaging) for further use.

The surface morphologies of the produced nanoparticles were studied using a variable pressure scanning electron microscope (VPSEM, LEO 1455, Germany) after coating the powder with gold. The elemental analyses were performed using an energy dispersive X-ray analyser (EDX, model 7353, England), directly connected to the VPSEM. The crystal shapes and sizes were determined using a TEM (Hitachi H-7100, Japan). For TEM study, the produced nanoparticles powder of cockle shells were mixed with absolute alcohol under sonication for 30 min, and the colloidal solution was dropped on to a carbon-covered copper grid, placed on a filter paper, and dried at room temperature for 1 h. The purity and crystalline properties of the powders were investigated by an X-ray powder diffractometer (Shimadzu XRD-6000, Japan) operated at $\text{CuK}\alpha$ ($\lambda = 1.540562\ \text{\AA}$). The chemical analyses were done using a Fourier transform infrared (FT-IR) spectrophotometer (Model 100, Perkin Elmer, 710 Bridgeport Avenue, Shelton, CT USA) over a range of 280 to $4000\ \text{cm}^{-1}$ at a resolution of $2\ \text{cm}^{-1}$ and at scan speed of $64/\text{s}$.

3. Results and Discussion

The surface morphologies as obtained from VPSEM cockle shells powder before (Figure 1(a)) and after adding BS-12 (Figure 1(b)) are shown in Figure 1. While the rod-shaped aragonite crystals clearly appeared in the cockle shells powder before adding BS-12 (Figure 1(a)), the larger clumps of smaller and agglomerated calcium carbonate crystals were observed after treatment with BS-12 (Figure 1(b)). The SEM studies thus suggested that BS-12 probably catalyzed the breakdown of larger particles into the smaller ones through the enhancement of inter particle adhesiveness.

To visualize the calcium carbonate particles more clearly, transmission electron micrographs were studied. The TEM images of cockle shells powder before (Figure 2(a)) and after adding 2 mL of BS-12 (Figure 2(b)) are shown in Figure 2. While the micron-sized rod-like aragonite crystals of diameter $10\text{--}90\ \mu\text{m}$ were observed in the cockle shells powders without addition of any organic surfactant or catalyst (Figure 2(a)), the rod-shaped aragonite crystals of diameter $30 \pm 5\ \text{nm}$ clearly appeared in the presence of 2 mL of BS-12 (Figure 2(b)). A number of previous studies indicated the formation of rod-like aragonite crystals in presence of polyacrylamide [5] or in absence of any organic substrates such as polyacrylamide or BS-12 [3]. However, none of these studies obtained pure aragonite crystals of homogeneous sizes and shapes. In most of the cases, the aragonite crystals were obtained as a mixture of calcite and aragonite [3, 5] or calcite, vaterite, and aragonite [2]. For the first time, we prepared rod-shaped aragonite crystals of the smallest and homogeneous sizes and shapes from a low cost and available natural resource such as cockle shell, using a top-down approach in the presence of BS-12. BS-12 is extensively reported in the bottom-up approach [13] where it acts as a surfactant to control the nucleation and growth pattern of the calcite particles. However, the method

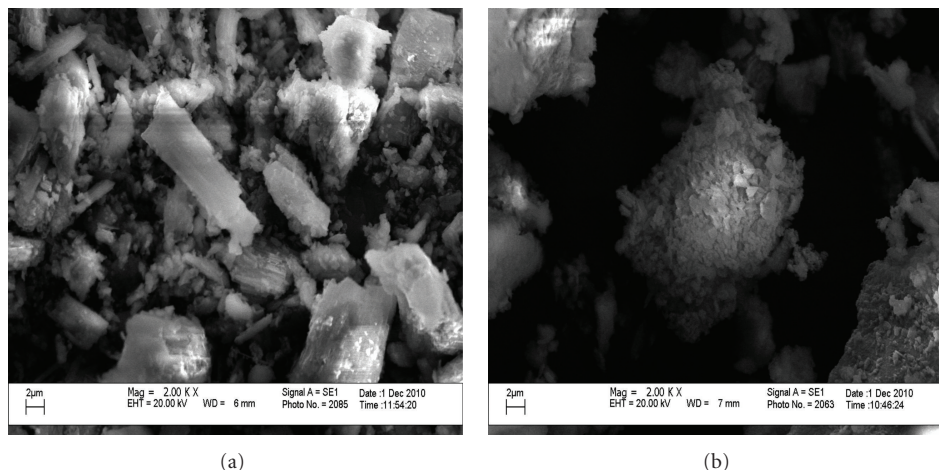


FIGURE 1: SEM micrograph of cockle shells powders before (a) and after (b) the addition of BS-12. The crystals of cockle shells powders were white, larger, rod-shaped, and separated in the absence of BS-12, whereas the crystals were smaller sized, agglomerated, and clumped together in the presence of BS-12.

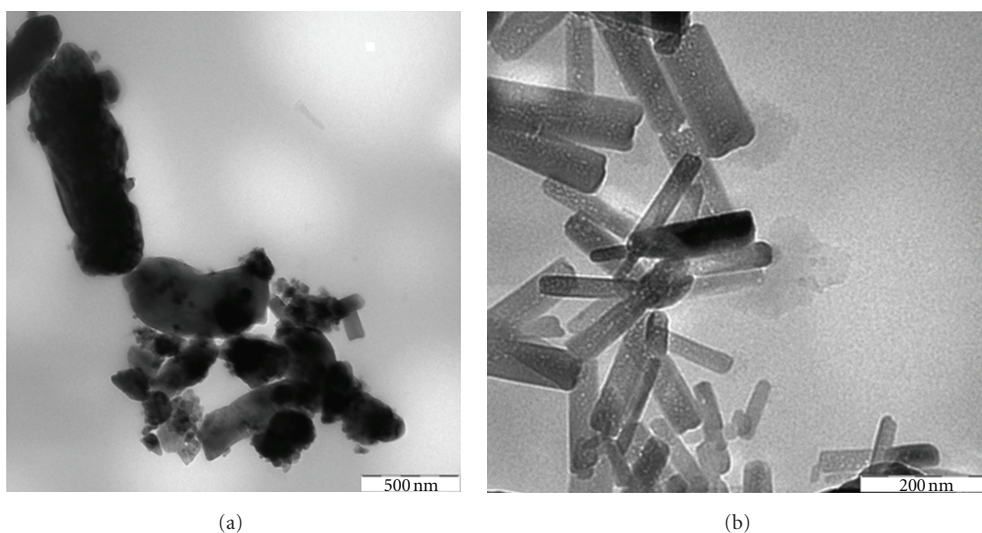


FIGURE 2: TEM image of cockle shells powders before (a) and after (b) the addition of BS-12. While the micron-sized rough rod-like crystals were observed before adding any catalyst (a), the clear nanosized rod-like crystals were synthesized after adding BS-12 as a catalyst (b).

adds some BS-12 impurities in the final products which may not be suitable for biological applications [13]. However, in this study, we have not observed any BS-12 as impurities in the final aragonite particles. Here, BS-12 probably acted as a catalyst to loosen the bundles of rod-shaped aragonite crystals that are present as a large bundles in the original cockle shells as well as in its powder form.

The FT-IR spectra of cockle shells powders before (Figure 3(a)) and after the addition of 2 mL of BS-12 (Figure 3(b)) are demonstrated in Figure 3. Prominent absorption peaks of carbonate appeared at 1455 cm^{-1} in the cockle shells powders in all conditions ((Figure 3(a)) and (Figure 3(b))). No positional shift of this peak was observed before (Figure 3(a)) and after adding BS-12 (Figure 3(b)).

This peak was attributed to the alkyl group which is present in the aragonite polymorphs [4]. Two other peaks appeared at 1794 cm^{-1} and 2520 cm^{-1} were referred to the amide and carboxylic stretching vibration [4]. The characteristic peaks, which represent CO_3^{2-} of aragonite, were observed at 1082 cm^{-1} and 857 cm^{-1} . No positional shift of these peaks was seen before and after addition of BS-12. The peaks defining the CO_3^{2-} of aragonite appeared at 1082 and 857 cm^{-1} [4, 11]. Wang et al. [13] obtained two peaks at 2875 and 2993 cm^{-1} in calcite nanoparticles synthesised via carbonation method in the presence of BS-12 as an organic surfactant. These peaks were assigned to the residual BS-12, embedded on the particle surfaces. However, such a peak that can demonstrate the presence or contamination

TABLE 1: EDX profiles of cockle shells powders before (a) and after (b) the addition of 2 mL BS-12. No significant change in the presence of BS-12.

Spectrum	C	O	Al	Ca	Cu	Te	Total
Without BS-12 (a)							
Spectrum 1	16.39	30.15	0.61	50.12	1.4	1.33	100
Spectrum 2	15.66	28.8	0.47	52.38	2.3	0.39	100
Spectrum 3	30.93	27.71	1.69	32.76	4.96	1.95	100
Mean	20.99	28.88	0.92	45.08	2.88	1.22	100
Std. deviation	8.61	1.22	0.66	10.73	1.85	0.78	
Max	30.93	30.15	1.69	52.38	4.96	1.95	
Min	15.66	27.71	0.47	32.76	1.4	0.39	
With BS-12 (b)							
Spectrum 1	16.10	30.26	0.67	50.27	1.35	1.35	100
Spectrum 2	15.65	28.79	0.47	52.46	2.29	0.34	100
Spectrum 3	30.93	27.71	1.69	32.76	4.91	2.00	100
Mean	20.89	28.92	0.94	45.16	2.85	1.23	100
Std. deviation	8.70	1.27	0.64	10.78	1.85	0.81	
Max	30.93	30.26	1.69	52.46	4.91	2.00	
Min	15.65	27.71	0.47	32.76	1.35	0.34	

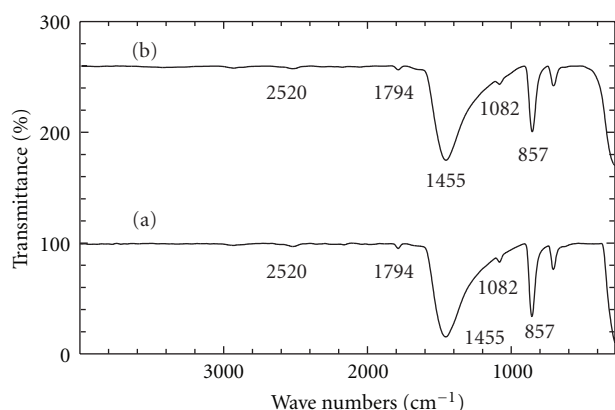


FIGURE 3: FT-IR spectra of cockle shells powders before (a) and after (b) the addition of BS-12. The characteristics absorption peaks of aragonite polymorph were observed both in the absence and presence of BS-12 ((a) and (b)).

of BS-12 was totally absent in the FT-IR spectra of the synthesised aragonite nanoparticles, suggesting that ANPs were synthesised without any additional impurities.

The XRD patterns of cockle shells powders before (Figure 4(a)) and after adding 2 mL of BS-12 (Figure 4(b)) are demonstrated in Figure 4. The XRD patterns of cockle shells powders (Figure 4(a)) completely matched with the aragonite phase (JCPDS file no. 00-003-0425). The reflection patterns of cockle shells powders (Figure 4(b)) were characteristic of calcium carbonate in the aragonite phase (JCPDS no. 00-001-0628). No additional influence of BS-12 was found in any of these XRD profiles. The XRD patterns of cockle shells powders did not show any peaks of mixed polymorphs such as calcite and aragonite [3, 5] or calcite, aragonite, and vaterite [2], demonstrating that pure crystalline aragonite nanoparticles were synthesised in the presence of BS-12 which most likely acted as a biomineralization catalyst.

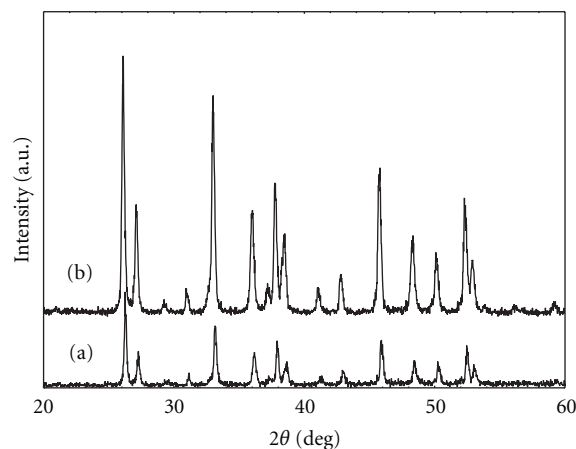


FIGURE 4: XRD patterns of cockle shells powders before (a) and after (b) the addition of BS-12. The aragonite phase appeared in both XRD patterns.

The elemental compositions of the cockle shells powders before and after adding 2 mL of BS-12 are shown in Table 1. While the cockle shells powders in the absence of BS-12 contained 20.99% carbon, 28.88% oxygen, 0.92% aluminium, 45.08% calcium, 2.88% copper, and 1.22% tellurium [4], the cockle shells powders in presence of 2 mL of BS-12 contains 20.89% carbon, 28.92% oxygen, 0.94% aluminium, 45.16% calcium, 2.85% copper, and 1.23% tellurium. No significant change in the elemental compositions of the obtained cockle shells nanoparticles were found after the addition of BS-12, reflecting the catalytic role of BS-12 in the breakdown of larger bundles of aragonite rods into the smaller or singular ones.

4. Conclusion

A simple, low-cost, and environmentally friendly method for the synthesis of calcium carbonate nanoparticles (aragonite)

from a low-cost and abundant natural resource, cockle shell, was developed. The method was a top-down approach which involved minimum procedural steps and did not need any stringent temperature management, expensive and hazardous chemicals or any carbonation step of expensive and time consuming gas bubbling. It was simply a mechanical grinding process using very simple, easily available, and low-cost instrument in the presence of a biomineralization catalyst, dodecyl dimethyl betaine. The method produces very small-sized excellent rod-shaped and pure aragonite nanoparticles with an average diameter of 30 ± 5 nm in a reproducible manner without any additional impurities. The method has a great potential to be used in industry for large-scale synthesis of aragonite nanoparticles for biomedical applications.

Acknowledgment

The authors gratefully acknowledge the financial support from the Fundamental Research Grand Scheme of Malaysia (FRGS).

References

- [1] H. Bala, W. Fu, J. Zhao et al., "Preparation of BaSO₄ nanoparticles with self-dispersing properties," *Colloids and Surfaces A*, vol. 252, no. 2-3, pp. 129–134, 2005.
- [2] J. Chen and L. Xiang, "Controllable synthesis of calcium carbonate polymorphs at different temperatures," *Powder Technology*, vol. 189, pp. 64–69, 2009.
- [3] F. Guo, Y. Li, H. Xu, G. Zhao, and X. He, "Size-controllable synthesis of calcium carbonate nanoparticles using aqueous foam films as templates," *Materials Letters*, vol. 61, no. 27, pp. 4937–4939, 2007.
- [4] K. N. Islam, A. B. Z. Zuki, M. M. Noordin, M. Z. B. Hussein, N. S. S. B. A. Rahman, and M. E. Ali, "Characterisation of calcium carbonate and its polymorphs from cockle shells (*Anadara granosa*)," *Power Technology*, vol. 213, no. 1–3, pp. 188–191, 2011.
- [5] C. Wang, J. Zhao, X. Zhao, H. Bala, and Z. Wang, "Synthesis of nanosized calcium carbonate (aragonite) via a polyacrylamide inducing process," *Powder Technology*, vol. 163, no. 3, pp. 134–138, 2006.
- [6] S. I. Stupp and P. V. Braun, "Molecular manipulation of microstructures: biomaterials, ceramics, and semiconductors," *Science*, vol. 277, no. 5330, pp. 1242–1248, 1997.
- [7] Z. P. Xu, Q. H. Zeng, G. Q. Lu, and A. B. Yu, "Inorganic nanoparticles as carriers for efficient cellular delivery," *Chemical Engineering Science*, vol. 61, no. 3, pp. 1027–1040, 2006.
- [8] H. Kawaguchi, H. Hirai, K. Sakai et al., "Crystallization of inorganic compounds in polymer solutions. Part I: control of shape and form of calcium carbonate," *Colloid & Polymer Science*, vol. 270, no. 12, pp. 1176–1181, 1992.
- [9] N. Wada, S. Suda, K. Kanamura, and T. Umegaki, "Formation of thin calcium carbonate films with aragonite and vaterite forms coexisting with polyacrylic acids and chitosan membranes," *Journal of Colloid and Interface Science*, vol. 279, no. 1, pp. 167–174, 2004.
- [10] A. M. Belcher, X. H. Wu, R. J. Christensen, P. K. Hansma, G. D. Stucky, and D. E. Morse, "Control of crystal phase switching and orientation by soluble mollusc-shell proteins," *Nature*, vol. 381, no. 6577, pp. 56–58, 1996.
- [11] C. S. Choi and Y. W. Kim, "A study of the correlation between organic matrices and nanocomposite materials in oyster shell formation," *Biomaterials*, vol. 21, no. 3, pp. 213–222, 2000.
- [12] R. Lakshminarayanan, S. Valiyaveetil, and G. L. Loy, "Selective nucleation of calcium carbonate polymorphs: role of surface functionalization and poly(vinyl alcohol) additive," *Crystal Growth and Design*, vol. 3, no. 6, pp. 953–958, 2003.
- [13] C. Wang, Y. Liu, H. Bala et al., "Facile preparation of CaCO₃ nanoparticles with self-dispersing properties in the presence of dodecyl dimethyl betaine," *Colloids and Surfaces A*, vol. 297, no. 1–3, pp. 179–182, 2007.

Research Article

High-Sensitive Sensor of Dopamine Based on Photoluminescence Quenching of Hierarchical CdS Spherical Aggregates

Binjie Sun¹ and Changzheng Wang²

¹College of Chemistry, Beijing Normal University, Beijing 100875, China

²Key Laboratory of Urban Stormwater System and Water Environment, Beijing University of Civil Engineering and Architecture, Beijing 100044, China

Correspondence should be addressed to Binjie Sun, sunbinjie@mail.bnu.edu.cn

Received 21 May 2012; Accepted 24 May 2012

Academic Editor: Xiao-Miao Feng

Copyright © 2012 B. Sun and C. Wang. This is an open access article distributed under the Creative Commons Attribution License, which permits unrestricted use, distribution, and reproduction in any medium, provided the original work is properly cited.

Hierarchical CdS spherical aggregates have been fabricated by an assembling strategy starting from nanoparticles, which opens a general way to obtain hierarchical spherical aggregates of different types of materials. The hierarchical CdS spherical aggregates are of high porosity and high surface area, which give rise to unique photoluminescence properties. The desirable properties we report here will spur further developments of novel dopamine photoluminescence sensors based on the high surface area hierarchical CdS spherical aggregates fabricated with our unique assembling strategy. The novel dopamine photoluminescence sensor has a low detection limit of 1.0×10^{-8} M, which is much lower than those reported previously.

1. Introduction

Dopamine (DA), as one of the most important neurotransmitters, was discovered in the 1950s, which has ever since captured the interest of neuroscientists and chemists. High DA levels are known to be cardiotoxic, leading to rapid heart rate, high blood pressure, and possible death of the heart muscles. On the contrary, a loss of DA-containing neurons may result in some serious diseases such as Parkinson's disease and schizophrenia [1–7]. Hence, determining the concentration of this neurochemical is of biomedical significance.

The detection of DA is most often accomplished by the measurement of redox potential or intrinsic fluorescence. Fluorescence quenching refers to any process which decreases the fluorescence intensity of a sample, which has been widely studied both as a fundamental phenomenon and as a source of information about biochemical systems [8–10]. With the development of nanotechnology, many methods have been developed to detect DA by using nanomaterials such as carbon nanotubes and gold nanoparticles (NPs) [11–15]. Semiconductor nanoparticles have attracted much attentions since they have unique optical and several other properties

such as size-dependent, tunable adsorption and emission properties [16]. Fluorescence detection methods have led to major improvement in bioanalytical applications because of their extraordinary sensitivity and selectivity. The traditional fluorescence probes are organic dyes, and semiconductor nanocrystals with unique structure could probably be used to substitute the organic dyes based on their unique optical properties.

As a unique structure, hierarchical assembly of nanoscale building blocks is a crucial step toward realization of functional nanosystems and represents a significant challenge in the field of nanoscience [17]. The past few years have witnessed increasing attention focused on such novel structures, because of their unique optical, electrical, and surface properties that underlie their potential applications in photoelectric devices, drug delivery, sensors, filters, coatings, and chemical catalysis. Methods that support hierarchical assembly over multiple length scales are particularly promising for designing functional nanostructures and assembling nanodevices. Many efforts have been developed to shape nanoscale materials to hierarchical nanoarchitectures, such as hierarchically ordered oxides (silica, niobia, and titania), zinc oxide hierarchically ordered nanowire arrays,

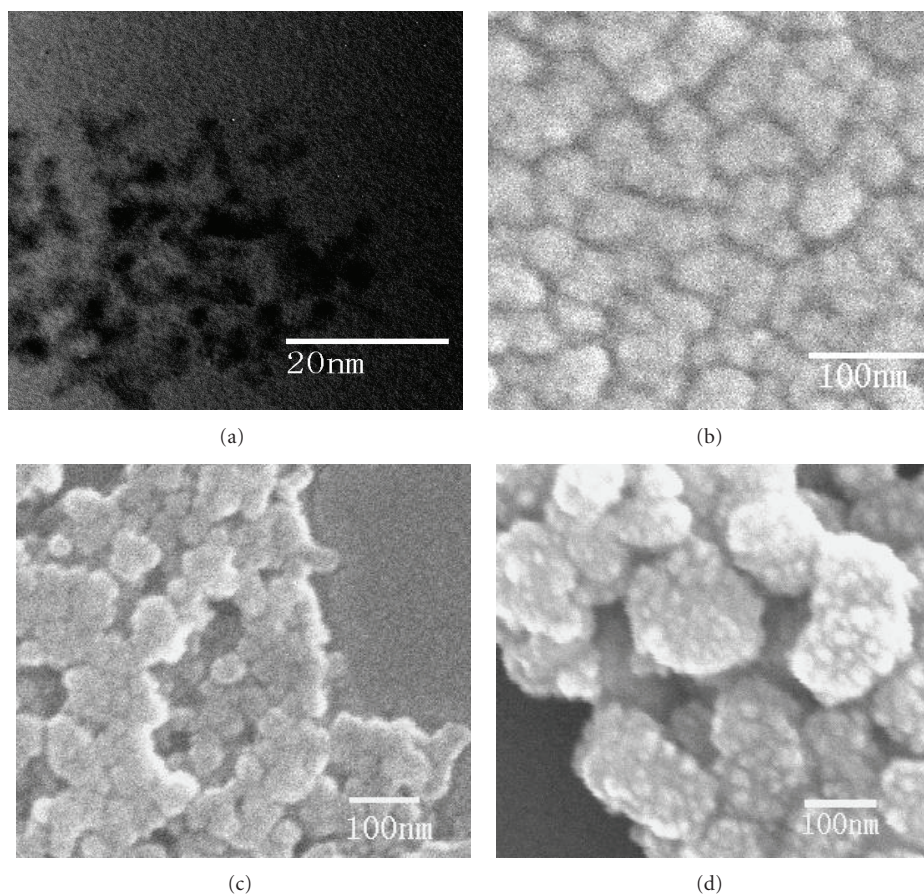


FIGURE 1: TEM image (a) of CdS colloids prepared in tetrachlorethylene and octylamine mixed solution and SEM images (b, c, d) of the hierarchical CdS spherical aggregates.

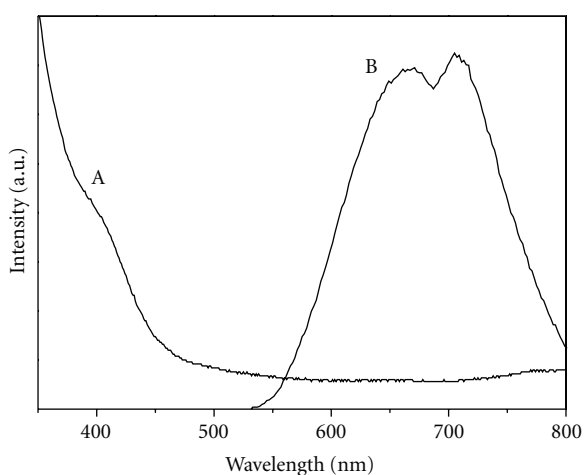


FIGURE 2: UV-vis absorption and photoluminescence spectra of hierarchical CdS spherical aggregates.

hierarchical zinc sulfide nanostructures, gold nanoparticle, nanotubes, and rhodium spherical aggregates [18–21].

Hierarchical spherical aggregates, who are composed of NPs in a multi-length-scale assembly, possess high surface

area and therefore are particularly important in catalysis, sensors, and nanodevices. It is well known that CdS is an outstanding photoelectric semiconductor material [22, 23]. It is envisaged that NP-assembled hierarchical CdS spherical aggregates, with intimate inter-NP contacts and a direct connection to the electrode and large exposed surface areas, should provide an ideal nanoarchitecture for efficient generation of photoluminescence (PL). Although numerous shapes of CdS nanocrystals have been prepared, to our knowledge, there has been few reports on such hierarchical spherical aggregates from CdS NPs to be used as a sensor for DA. Herein, we report a simple approach for the detection of DA by high surface area hierarchical CdS spherical aggregates.

2. Material and Methods

All chemicals were of analytical grade and were used without further purification.

2.1. Preparation of Hierarchical CdS Spherical Aggregates. CdS NPs and their spherical aggregates were prepared in organic solvents, and the procedure is described here. CdS quantum dots were synthesized according to the literature

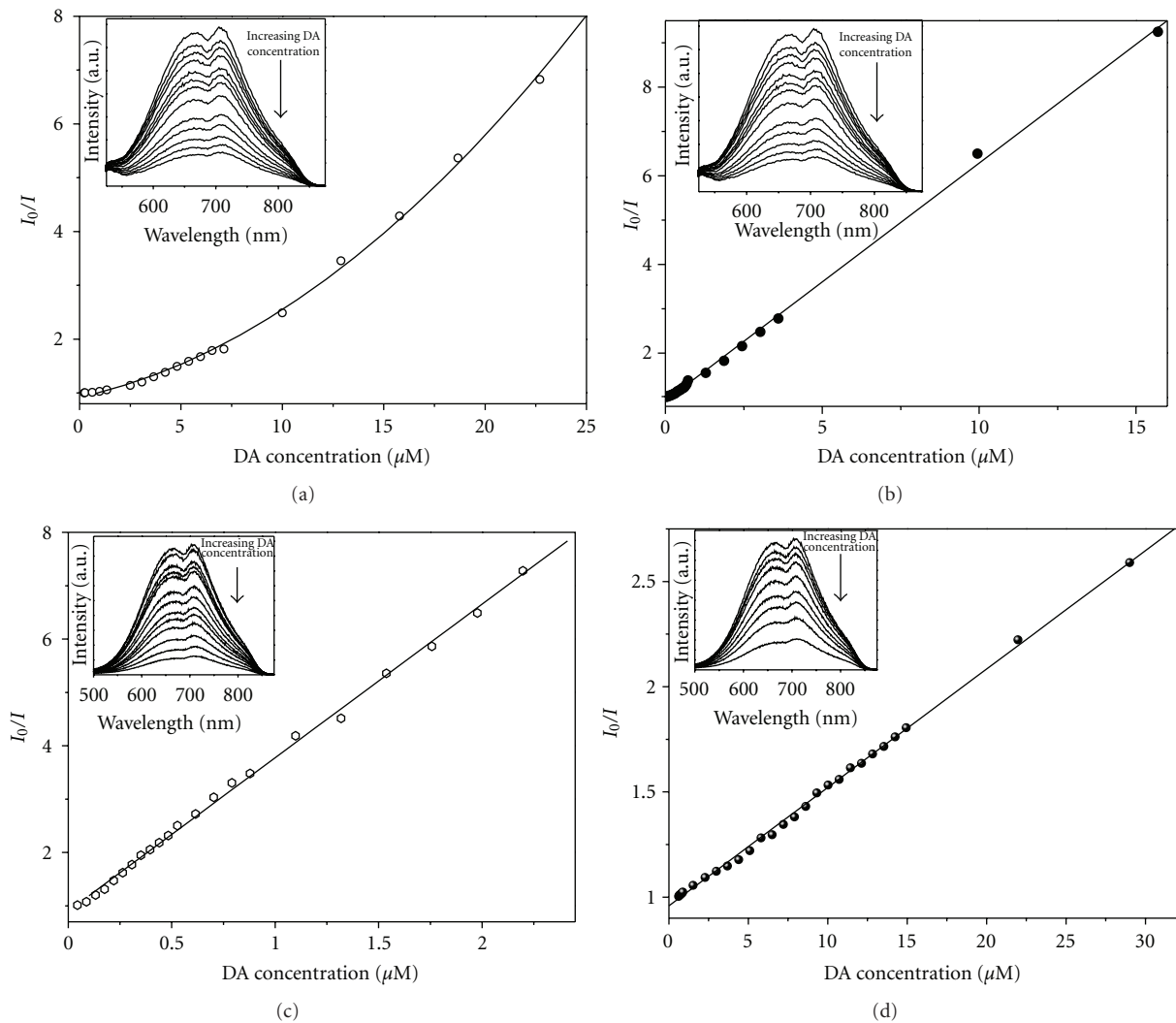


FIGURE 3: Dependence of the PL intensity of hierarchical CdS spherical aggregates on the concentration of DA, with different volume ratio of tetrachlorethylene to ethanol: (a) 4 : 1, (b) 1 : 4, (c) 1 : 50, and (d) CdS colloidal solution without ethanol.

but with improvement [24]. In a typical procedure, 0.25 g sublimed sulfur was dissolved in 200 mL dimethyl sulphoxide (DMSO) at 100°C for about 1 hour and then increased to 150°C . At this temperature, a preheated solution of 2.5 g cadmium acetate in 200 mL DMSO was added. The solution became lemon yellow after several minutes. The reaction solution was kept in 150°C for about one hour and then cooled to ambient temperature. Adding 100 mL acetone to the solution, the precipitant was collected by centrifuging and then washed with acetone for two times. After dried under vacuum at room temperature, the CdS quantum dots were obtained. Analytical grade octylamine, which was used to increase the solubility of the CdS quantum dots, was dissolved in tetrachlorethylene (the volume ratio of octylamine to tetrachlorethylene was 0.1%). CdS colloid in tetrachlorethylene was obtained through 0.1 mg CdS quantum dots adding 99.9 mL tetrachlorethylene and 0.1 mL octylamine. The CdS colloid was stable for more than 6 months at ambient temperature. Hierarchical CdS spherical

aggregates were assembled by adding ethanol in the CdS colloid. The size distributions of these spherical aggregates vary with the volume ratio of tetrachlorethylene and ethanol.

2.2. The Photoluminescence Quenching of Hierarchical CdS Spherical Aggregates by Dopamine. DA was dissolved in ethanol. Hierarchical CdS spherical aggregates were dispersed in ethanol (3 mL), and the photoluminescence of CdS was recorded before DA was added. Then DA solution was dropped into CdS by injector, and after solution was mixed round adequately, the photoluminescence intensity was recorded step by step.

2.3. Characterization. The morphology and size of the hierarchical CdS spherical aggregates were analyzed with a Hitachi S4800 scanning electron microscope (SEM) and a Philips CM20 transmission electronic microscope (TEM). The UV-vis spectra were measured at room temperature with

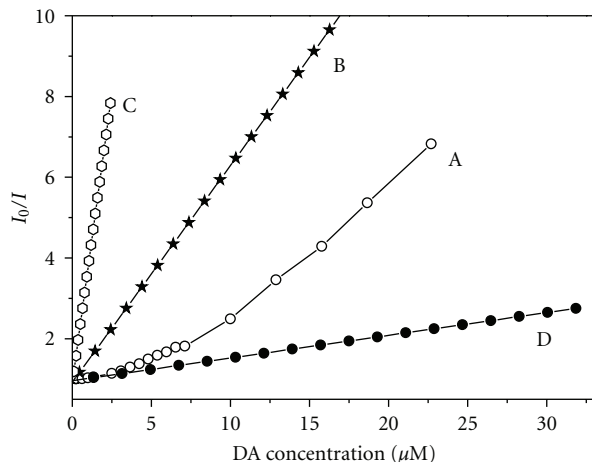


FIGURE 4: A linear relation between the PL intensity and DA concentration, with different volume ratio of tetrachlorethylene to ethanol: (a) 4 : 1, (b) 1 : 4, (c) 1 : 50, and (d) CdS colloidal solution without ethanol.

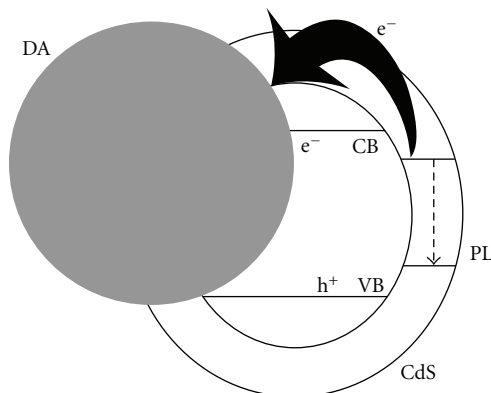


FIGURE 5: Schematic illustration for the fluorescence quenching principle of CdS in the presence of DA.

a lambda 900 UV-vis spectrophotometer (GBC, Cintra10). Photoluminescence spectra were measured at room temperature with an LS50 steady-state fluorescence spectrometer (Shimadzu, RF-5301PC).

3. Results and Discussions

TEM image (Figure 1(a)) shows that the diameter of the as-prepared CdS quantum dots is about 2–5 nm, which dissolves neither in tetrachlorethylene nor in ethanol. When ethanol was added into the CdS colloid, the hierarchical CdS spherical aggregates could be obtained. SEM images testify the formation of hierarchical CdS spherical aggregates. Figures 1(b) to 1(d) show that as-prepared hierarchical CdS spherical aggregates are composed of small CdS NPs. The uniform spherical aggregates with diameter about 100 nm were built from CdS nanoparticles with the size of smaller than 5 nm. The diameter of the spherical aggregates was controlled by the volume ratio of ethanol to tetrachlorethylene. With the increase of the volume ratio of ethanol to

tetrachlorethylene, the diameter of the spherical aggregates increases.

From Figures 1(b) to 1(d) depicted the SEM images of hierarchical CdS spherical aggregates growing at different volume ratios of tetrachlorethylene to ethanol. Figure 1(b) showed the morphology of the sample, which is obtained when the ratio of tetrachlorethylene to ethanol is 4 : 1 (V/V). Its diameter ranges from 20 to 50 nm. When this ratio was changed to be 1 : 4 (V/V), the diameter of spherical aggregates was larger as shown in Figure 1(c). As shown in Figure 1(d), when the ratio of tetrachlorethylene to ethanol was increased to 1 : 50 (V/V), the diameter of spherical aggregates ranges from 80 to 100 nm, which were clearly comprised of bright spots of individual CdS quantum dots with the diameter of 20–30 nm. But continuing to increase the volume ratio of tetrachlorethylene to ethanol, the CdS nanoparticles will be deposited. It distinctly indicated that the hierarchical CdS spherical aggregates were able to be produced by the self-assembly of CdS quantum dots, and the size of the self-assembled CdS spherical aggregates can be controlled by the volume ratio of tetrachlorethylene to ethanol.

Optical properties of the hierarchical CdS spherical aggregates have been studied by UV-vis absorption and photoluminescence (Figure 2). The UV-vis absorption spectra substantiate the formation of hierarchical CdS spherical aggregates (Figure 2(a)), which is consistent with the UV-vis spectra of CdS nanoparticles, with the absorption peak 420 nm. For hierarchical CdS spherical aggregates, the PL emissions are at around 700 nm, which is attributed to the trapped emission (Figure 2(b)).

The effect of DA concentration on the PL emissions intensity of hierarchical CdS spherical aggregates is shown in Figure 3. The linear relation between the PL intensity and DA concentration can be obtained, respectively, when the ratio of tetrachlorethylene to ethanol is 4 : 1, 1 : 4, and 1 : 50.

As proved previously, addition of DA to the aqueous solution of CdS led to a significant quenching of the PL emission of CdS. Moreover, DA gave a steady and maximal quenching effect on the fluorescence of CdS. PL emission is much sensitive to their surface structures and is dependent on the surface properties and the presence of surface states. And, with much more ethanol concentration, the surface of hierarchical CdS spherical aggregates will be higher, and the quenching effect will become more prominent (Figure 4). When the ratio of tetrachlorethylene to ethanol is 1 : 50, the linear relation between the PL intensity and DA concentration was obtained. The detection limit of DA was detected to be 1.0×10^{-8} M, lower than those of biosensors reported [1, 2], which demonstrate that hierarchical CdS spherical aggregates can be developed to be used as DA sensor.

The fluorescence quenching principle of CdS in the presence of DA is illustrated in Figure 5. The fact that DA substantially quenched the fluorescence of CdS indicates a strong interaction between the excited-state CdS and the attached DA molecules. A plausible explanation for the PL peak quenchments presented here is the unique surface electronic structure of the hierarchical CdS spherical aggregates.

When the active sites of hierarchical CdS spherical aggregates increased, a junction is built up, and DA can act as an electron acceptor. Quenching of the PL emissions of CdS by DA is expected via the new nonradiative pathways created by the proximity of DA, possibly resulting from electron transfer from CdS to DA [25].

4. Conclusions

In summary, high surface area hierarchical CdS spherical aggregates have been fabricated by an assembling strategy starting from nanoparticles, which opens a general way to obtain hierarchical spherical aggregates of different types of materials. The hierarchical CdS spherical aggregates are of high porosity, high surface area, and high order, which give rise to unique PL properties. All of the desirable properties we report here will spur further developments of novel DA sensors based on the hierarchical CdS spherical aggregates fabricated with our simple assembling strategy.

Acknowledgments

The authors gratefully acknowledge the support from the National Nature Science Foundation of China (20975016, 21175014, 91027034, and 21103008), National Grant of Basic Research Program of China (no. 2011CB915504), the Fundamental Research Funds for the Central Universities (2009SC-1), and Open Research Fund Program of Key Laboratory of Urban Stormwater System and Water Environment (Beijing University of Civil Engineering and Architecture), Ministry of Education.

References

- [1] J. L. Chen, X. P. Yan, K. Meng, and S. F. Wang, "Graphene oxide based photoinduced charge transfer label-free near-infrared fluorescent biosensor for dopamine," *Analytical Chemistry*, vol. 83, no. 22, pp. 8787–8793, 2011.
- [2] P. C. Pandey, D. S. Chauhan, and V. Singh, "Effect of processable polyindole and nanostructured domain on the selective sensing of dopamine," *Materials Science and Engineering C*, vol. 32, no. 1, pp. 1–11, 2012.
- [3] C. Yu, J. Yan, and Y. Tu, "Electrochemiluminescent sensing of dopamine using CdTe quantum dots capped with thioglycolic acid and supported with carbon nanotubes," *Microchimica Acta*, vol. 175, no. 3–4, pp. 347–354, 2011.
- [4] D. R. Shankaran, K. Limura, and T. Kato, "Simultaneous determination of ascorbic acid and dopamine at a sol-gel composite electrode," *Sensors and Actuators B*, vol. 94, no. 1, pp. 73–80, 2003.
- [5] K. Kurzatowska, E. Dolusic, W. Dehaen, K. Sieroń-Stołyń, A. Sieroń, and H. Radecka, "Gold electrode incorporating corrole as an ion-channel mimetic sensor for determination of dopamine," *Analytical Chemistry*, vol. 81, no. 17, pp. 7397–7405, 2009.
- [6] L. Lin, P. Qiu, L. Yang, X. Cao, and L. Jin, "Determination of dopamine in rat striatum by microdialysis and high-performance liquid chromatography with electrochemical detection on a functionalized multi-wall carbon nanotube electrode," *Analytical and Bioanalytical Chemistry*, vol. 384, no. 6, pp. 1308–1313, 2006.
- [7] L. Zhang and X. Lin, "Electrochemical behavior of a covalently modified glassy carbon electrode with aspartic acid and its use for voltammetric differentiation of dopamine and ascorbic acid," *Analytical and Bioanalytical Chemistry*, vol. 382, no. 7, pp. 1669–1677, 2005.
- [8] P. Bolel and M. Halder, "Fluorescence quenching of carmoisine by viologens in neat methanol: observation of inversion in quenching," *Chemical Physics Letters*, vol. 507, no. 4–6, pp. 234–239, 2011.
- [9] B. Sui, L. Shen, and W. Jin, "Ultrasensitive determination of 1,4-dihydroxybenzene based on fluorescence resonance energy quenching of luminescent quantum dots modified on surface of silica nanoparticles," *Talanta*, vol. 85, no. 3, pp. 1609–1613, 2011.
- [10] X. G. Gu, G. X. Zhang, and D. Q. Zhang, "A new ratiometric fluorescence detection of heparin based on the combination of the aggregation-induced fluorescence quenching and enhancement phenomena," *Analyst*, vol. 137, no. 2, pp. 365–369, 2012.
- [11] H. Jeong and S. Jeon, "Determination of dopamine in the presence of ascorbic acid by nafion and single-walled carbon nanotube film modified on carbon fiber microelectrode," *Sensors*, vol. 8, no. 11, pp. 6924–6935, 2008.
- [12] K. Wu, J. Fei, and S. Hu, "Simultaneous determination of dopamine and serotonin on a glassy carbon electrode coated with a film of carbon nanotubes," *Analytical Biochemistry*, vol. 318, no. 1, pp. 100–106, 2003.
- [13] Z. H. Wang, Q. L. Liang, Y. M. Wang, and G. A. Luo, "Carbon nanotube-intercalated graphite electrodes for simultaneous determination of dopamine and serotonin in the presence of ascorbic acid," *Journal of Electroanalytical Chemistry*, vol. 540, pp. 129–134, 2003.
- [14] C. R. Raj, T. Okajima, and T. Ohsaka, "Gold nanoparticle arrays for the voltammetric sensing of dopamine," *Journal of Electroanalytical Chemistry*, vol. 543, no. 2, pp. 127–133, 2003.
- [15] H. P. Wu, T. L. Cheng, and W. L. Tseng, "Phosphate-modified TiO₂ nanoparticles for selective detection of dopamine, levodopa, adrenaline, and catechol based on fluorescence quenching," *Langmuir*, vol. 23, no. 14, pp. 7880–7885, 2007.
- [16] D. M. Willard, L. L. Carillo, J. Jung, and A. Van Orden, "CdSe-ZnS quantum dots as resonance energy transfer donors in a model protein-protein binding assay," *Nano Letters*, vol. 1, no. 9, pp. 469–474, 2001.
- [17] Y. Cheng, Y. Wang, C. Jia, and F. Bao, "MnS hierarchical hollow spheres with novel shell structure," *Journal of Physical Chemistry B*, vol. 110, no. 48, pp. 24399–24402, 2006.
- [18] P. Yang, T. Deng, D. Zhao et al., "Hierarchically ordered oxides," *Science*, vol. 282, no. 5397, pp. 2244–2246, 1998.
- [19] M. Lahav, T. Sehayek, A. Vaskevich, and I. Rubinstein, "Nanoparticle nanotubes," *Angewandte Chemie*, vol. 42, no. 45, pp. 5576–5579, 2003.
- [20] T. D. Ewers, A. K. Sra, B. C. Norris et al., "Spontaneous hierarchical assembly of rhodium nanoparticles into spherical aggregates and superlattices," *Chemistry of Materials*, vol. 17, no. 3, pp. 514–520, 2005.
- [21] A. D. Dinsmore, M. F. Hsu, M. G. Nikolaidis, M. Marquez, A. R. Bausch, and D. A. Weitz, "Colloidosomes: selectively permeable capsules composed of colloidal particles," *Science*, vol. 298, no. 5595, pp. 1006–1009, 2002.
- [22] D. Routkevitch, T. Bigioni, M. Moskovits, and J. M. Xu, "Electrochemical fabrication of CdS nanowire arrays in porous anodic aluminum oxide templates," *Journal of Physical Chemistry*, vol. 100, no. 33, pp. 14037–14047, 1996.

- [23] Y. Liang, C. Zhen, D. Zou, and D. Xu, "Preparation of free-standing nanowire arrays on conductive substrates," *Journal of the American Chemical Society*, vol. 126, no. 50, pp. 16338–16339, 2004.
- [24] R. Elbaum, S. Vega, and G. Hodes, "Preparation and surface structure of nanocrystalline cadmium sulfide (Sulfoselenide) precipitated from dimethyl sulfoxide solutions," *Chemistry of Materials*, vol. 13, no. 7, pp. 2272–2280, 2001.
- [25] T. Mokari, E. Rothenberg, I. Popov, R. Costi, and U. Banin, "Selective growth of metal tips onto semiconductor quantum rods and tetrapods," *Science*, vol. 304, no. 5678, pp. 1787–1790, 2004.